Design, Analysis and Testing of a Self-reactive Wave Energy Point Absorber with Mechanical Power Take-off

Xiaofan Li

Dissertation submitted to the faculty of the Virginia Polytechnic Institute and State University in partial fulfillment of the requirements for the degree of

Doctor of Philosophy
In
Mechanical Engineering

Lei Zuo
Robert G Parker
Danesh Tafti
Khai Ngo
Yi-Hsiang Yu

September 18th, 2020
Blacksburg, VA

Keywords: Ocean wave energy harvesting; Point absorber; Bench test; Wave tank test; Power optimization

Design, Analysis and Testing of a Self-reactive Wave Energy Point Absorber with Mechanical Power Take-off

Xiaofan Li

ABSTRACT

Ocean wave as a renewable energy source possesses great potential for solving the world energy crisis and benefit human beings. The total theoretical potential wave power on the ocean-facing coastlines of the world is around 30,000 TWh, although cannot all be adopted for generating electricity, the amount of the power can be absorbed still can occupy a large portion of the world's total energy consumption. However, multiple reasons have stopped the ocean wave energy from being widely adopted, and among those reasons, the most important one is the immature of the Power Take-off (PTO) technology.

In this dissertation, a self-reactive two body wave energy point absorber that is embedded with a novel PTO using the unique mechanism of Mechanical Motion Rectifier (MMR) is investigated through design, analysis and testing to improve the energy harvesting efficiency and the reliability of the PTO. The MMR mechanism can transfer the reciprocated bi-directional movement of the ocean wave into unidirectional rotation of the generator. As a result, this mechanism brings in two advantages towards the PTO. The first advantage it possess is that the alternating stress of the PTO is changed into normal stress, hence the reliability of the components are expected to be improved significantly. The other advantage it brings in is a unique phenomenon of engagement and disengagement during the operation, which lead to a piecewise nonlinear dynamic property of the PTO. This nonlinearity of the PTO can contribute to an expanded frequency domain bandwidth and better efficiency, which are verified through both numerical simulation and in-lab experiment. During the in-lab test, the prototyped PTO achieved energy transfer efficiency as high as 81.2%, and over 40% of efficiency improvement compared with the traditional non-MMR PTO under low-speed condition, proving the previously proposed advantage.

Through a more comprehensive study, the MMR PTO is further characterized and a refined dynamic model. The refined model can accurately predict the dynamic response of the

PTO. The major factors that can influence the performance of the MMR PTO, which are the inertia of the PTO, the damping coefficient, and the excitation frequency, are explored through analysis and experiment comprehensively. The results show that the increase on the inertia of the PTO and excitation frequency, and decrease on the damping coefficient can lead to a longer disengagement of the PTO and can be expressed analytically.

Besides the research on the PTO, the body structure of the point absorber is analyzed. Due to the low-frequency of the ocean wave excitation, usually a very large body dimension for the floating buoy of the point absorber is desired to match with that frequency. To solve this issue, a self-reactive two body structure is designed where an additional frequency between the two interactive bodies are added to match the ocean wave frequency by adopting an additional reactive submerged body. The self-reactive two body structure is tested in a wave to compare with the single body design. The results show that the two body structure can successfully achieve the frequency matching function, and it can improve more than 50% of total power absorption compared with the single body design.

Design, Analysis and Testing of a Self-reactive Wave Energy Point Absorber with Mechanical Power Take-off

Xiaofan Li

GENERAL AUDIENCE ABSTRACT

Ocean wave as a renewable energy source possesses great potential for solving the world energy crisis and benefit human beings. The total theoretical potential wave power on the ocean-facing coastlines of the world is around 30,000 TWh, although impossible to be all transferred into electricity, the amount of the power can be absorbed still can cover a large portion of the world's total energy consumption. However, multiple reasons have stopped the ocean wave energy from being widely adopted, and among those reasons, the most important one is immature of the Power Take-off (PTO) technology. In this dissertation, a novel two body wave energy converter with a PTO using the unique mechanism of Mechanical Motion Rectifier (MMR) is investigated through design, analysis, and testing. To improve the energy harvesting efficiency and the reliability of the PTO, the dissertation induced a mechanical PTO that uses MMR mechanism which can transfer the reciprocated bi-directional movement of the ocean wave into unidirectional rotation of the generator. This mechanism brings in a unique phenomenon of engagement and disengagement and a piecewise nonlinear dynamic property into the PTO. Through a comprehensive study, the MMR PTO is further characterized and a refined dynamic model that can accurately predict the dynamic response of the PTO is established. The major factors that can influence the performance of the MMR PTO are explored and discussed both analytically and experimentally.

Moreover, as it has been theoretically hypothesis that using a two body structure for designing the point absorbers can help it to achieve a frequency tuning effect for it to better match with the excitation frequency of the ocean wave, it lacks experimental verification. In this dissertation, a scaled two body point absorber prototype is developed and put into a wave tank to compare with the single body structure. The test results show that through the use of two body structure and by designing the mass ratio between the two bodies properly,

the point absorber can successfully match the excitation frequency of the wave. The highest power capture width ratio (CWR) achieved during the test is 58.7%, which exceeds the results of similar prototypes, proving the advantage of the proposed design.

Acknowledgement

At the beginning of this dissertation, I would like to give sincere thanks to my advisor, Dr. Lei Zuo for the support, guidance, and encouragement he provided during my entire Ph.D. study. From him, I received valuable knowledge beyond the notebook on how to observe the engineering problems with scientific insight and conduct meaningful research. His brilliant mind and endless enthusiasm towards research mark him as a perfect role model for me and will always inspire me.

My grateful thank goes to Dr. Robert G. Parker and Dr. Khai Ngo for all the time and effort they spend on me during the past five years. It is my pleasure to work under your guidance on different projects.

I would like to express my gratitude to Dr. Danesh Tafti and Dr. Yi-Hsiang Yu for serving in my thesis committee, your time on reviewing my research, and the advice your give is much appreciated.

I would like to thank the financial support provided by the following funding agencies and projects, including the "Marine Energy Competition" project funded by National Renewable Energy Laboratory (NREL) under the grant NREL #SUB-2020-10058, the "Floating Oscillating Surge Wave Energy Converter using Controllable Efficient Power Takeoff System" funded by the United States Department of Energy (DOE) under the grant DE-EE0008953, the "Efficient and Reliable Power Takeoff for Ocean Wave Energy Harvesting" project funded by the United States Department of Energy (DOE) under the grant DE-EE0007174, the "GOALI: Energy Efficient and Reliable Motion Mechanism for Ocean Wave Energy Harvesting" project funded by the United States National Science Foundation (NSF) under the grant No. 1530122, the "Nets: Small: Ocean Mesh Networks Powered By Energy Harvesting" project funded by the United States National Science Foundation (NSF) under the grant No. 1527239, the "Ocean Wave Energy Harvester with a Novel Takeoff Mechanism" project funded by the United States Environmental Protection Agency (EPA) under the grant No. 83991001, and other funding sources including the Center of Innovative Technology's Commonwealth Research Commercialization Fund (CRCF), European Union's Marinet2, and Mechanical Engineering Department of Virginia Tech.

I would like to acknowledge all my lab mates at the Center for Energy Harvesting Materials and Systems (CEHMS), including the ones who worked in the same project with me once, which are Chien-An Chen, Dillon Martin, Lin Xu, Qiaofeng Li, Jia Mi, Boxi Jiang, Qiuchi Xiong, Shuo Chen, Jianuo Huang, Lisheng Yang, Weihan Lin, Peter Racioppo, Vicky Boontanom, Eric Dupuis, Adam Wise, Li Tan, and the ones who helped me whenever I need, which are Yilun Liu, Yalu Pei, Yu Pan, Sijing Guo, Yongjia Wu, Jie Chen, Shifeng Yu, Jackson Klein, Feng Qian, Mingyi Liu, Hongjip Kim, Kan Sun, Shengxi Zhou, Wei-Che Tai, HyunJun Jung, Isil Anakok, Yue Yuan, Rui Lin, Yuzhe Chen, Bonan Qin and Yifan Luo.

I would like to give credit to the undergraduate students who worked with me either on their senior design project or summer research and all finished their work excellently, including Elias Bearinger, Samuel Marthinuss, Kavi Muraleetharan, Wendy Sparrer, Rachael Chase, Rachael Duke, David Kennedy, Carl Capindo, Coby Mizrahi, Rosaline Lee, Luis Fernandez, Gabriel Palencia and Evan House.

I sincerely thank my friends who offered me endless comfort and support in their own ways during my Ph.D. study, including Changwei Liang, Yuhan Zhang, and Shaoxu Xing.

Finally, I would like to dedicate this dissertation to my beloved ones, especially my parents, Hongwei Li and Pufang Liu, and my wife Jingxuan Liu, for your love and support has been the biggest comfort of mine.

Contents

List of Figures

List of Tables

List of Publications

Journal Articles:

1. **Xiaofan Li,** Dillon Martin, Changwei Liang, Chien-An Chen, Khai Ngo, Robert G. Parker, Lei Zuo, "Characterization and Verification of a Two-body Wave Energy Converter with a Novel Power Take-off", *Renewable Energy*, 2020.

2. **Xiaofan Li,** Chien-An Chen, Changwei Liang, Qiaofeng Li, Lin Xu, Khai Ngo, Robert G. Parker, Lei Zuo, A Compact Mechanical Power Take-off for Wave Energy Converters: Design, Analysis, and Test Verification, *Applied Energy*, 2020.

3. **Xiaofan Li,** Changwei Liang, Chien-An Chen, Qiuchi Xiong, Robert G. Parker, Lei Zuo "Optimum Power Analysis of a Self-Reactive Wave Energy Point Absorber with Mechanically-driven Power Takeoffs", *Energy*, 2020.

4. Boxi Jiang, **Xiaofan Li,** Shuo Chen, Qiuchi Xiong, Bang-fuh Chen, Robert G Parker, Lei Zuo, "Performance Analysis and Tank Test Validation of a Hybrid Ocean Wave-Current Energy Converter with a Single Power Takeoff", *Energy Conversion and Management*, 2020.

5. Chien-An Chen, **Xiaofan Li,** Lei Zuo, Khai Ngo, "Circuit Modelling of the Mechanical-Motion-Rectifier for Electrical Simulation of Ocean Wave Power Take-off", *IEEE Trans. Industrial Electronics*, 2020.

6. Dillon Martin, **Xiaofan Li,** Chien-An Chen, Krish Thiagarajan, Khai Ngo, Robert Parker, Lei Zuo, "Numerical Analysis and Wave Tank Testing on the Optimal Design of a Two-Body Wave Energy Converter", *Renewable Energy*, 2020.

7. Xiuxing Yin, **Xiaofan Li,** and Lei Zuo, "Dynamic Characteristics and Test Results of a Wave Power Take-off System with Mechanical Motion Rectification and Transmission", *IEEE Trans. on Industrial Electronics*, 2019.

8. Jia Mi, Qiaofeng Li, Mingyi Liu, **Xiaofan Li,** Lei Zuo, "Design, Modelling, and Treadmill Tests of a Novel Suspended Energy-harvesting Backpack using Half-wave Mechanical Rectification", *Applied Energy*, accepted.

Selected peer-reviewed Conference Proceedings:

1. Chien-An Chen, **Xiaofan Li,** Khai Ngo, Lei Zuo, "A non-ideal Wave-to-Wire Model and Wave Tank Test Validation", the 13th European Wave and Tidal Energy Conference (EWTEC), Napoli, Italy, Sept 1-6, 2019.

2. **Xiaofan Li,** Chien-An Chen, Robert Parker, Khai Ngo, Lei Zuo, "Comparative study and test on a two body wave energy point absorber under various constraints", the 13th European Wave and Tidal Energy Conference (EWTEC), Napoli, Italy, Sept 1-6, 2019.

3. Shuo Chen, Boxi Jiang, **Xiaofan Li,** Qiuchi Xiong, Jianuo Huang, Robert Parker, Lei Zuo, Lei Zuo, Design and Dynamics of a Hybrid Ocean Wave and Current Energy Converter, ASME International Design Engineering Technical Conferences & Computers and Information in Engineering Conference (IDETC/CIE 2019), Anaheim, CA, 2019.

4. **Xiaofan Li** and Lei Zuo, On Designing and Simulation of a Novel Mechanical Power Take-off on a Two Body Wave Energy Point Absorber, ASME International Design Engineering Technical Conferences (IDETC), Quebec, Aug 2018.

5. Qiuchi Xiong, **Xiaofan Li** and Lei Zuo, Semi-active Control for Two-body Ocean Wave Energy Converter by Using Hybrid Model Predictive Control, 2018 ASME Dynamic Systems and Control Conference (DSCC), Oct 2018.

6. Xiuxing Yin, **Xiaofan Li,** Vicky Boontanom, Lei Zuo, "Dynamic characteristics and control strategy of a wave energy converter system based on dual ball screws and mechanical motion rectifier", 2017 ASME Dynamic Systems and Control Conference (DSCC), Oct 2017.

7. **Xiaofan Li,** Changwei Liang, Jedhathai Boontanom, Lei Zuo, "Design, fabrication and testing of wave energy converters(WECs) using different power take-off with mechanical motion rectifier", European Wave and Tidal Energy Conference, Ireland, Oct 2017.

8. **Xiaofan Li,** Changwei Liang and Lei Zuo, "Design and Analysis Of a Two-Body Wave Energy Converter With Mechanical Motion Rectifier", 2016 ASME Design Engineering Technical Conference (IDETC), Charlotte, NC, USA, Aug 2016.

Patent:

1. Lei Zuo, Robert G. Parker and **Xiaofan Li,** "Simultaneous Ocean Wave and Current Energy Harvesting using a Single Power Takeoff." U.S. Patent No.62/960,416.

1. Introduction

1.1 Background

1.1.1 Ocean wave energy source

The world has an increasing demand for renewable energy with the growing concerns for the climate change [1]. In the year of 2019, the total renewable energy capacity around the world is 2.536 TW, which increased more than 49% compared with the 1.692 TW capacity 5 years ago in 2014, indicating the importance of the renewable energy [2]. Ocean wave energy stands out among various renewable energies for its advantages of high power density [3]. The total global wave power resource is characterized to be around 2.11TW, 4.6% of which can be extracted by the Wave Energy Converters (WECs) [4]. Figure 1-1 shows a scheme on the gross wave energy potential for different ocean location points around the world [5], where different levels of wave power density is painted in different colors. If narrow down to the United States, the available wave energy resource along the United States coastline is 2,640 TWh/year, which can occupy nearly two-thirds of the 4,000 TWh of electricity used in the United States each year (2011) [6].

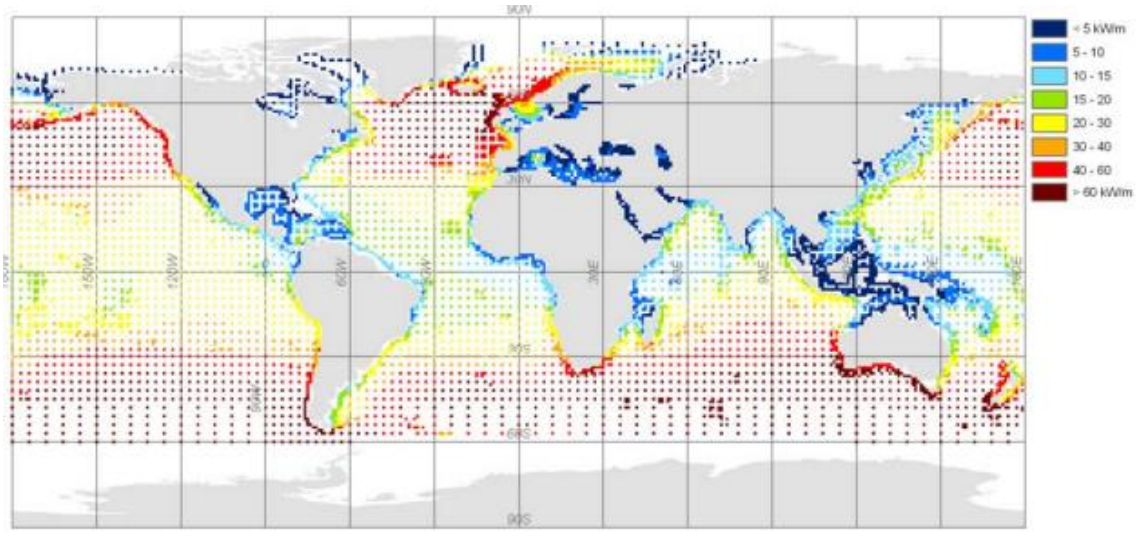

Figure 1-1 Annual global gross theoretical wave power for all grid points worldwide [5]

Unlike tidal energy that is mainly sourced from the gravitational attraction exerted from the celestial bodies, or the ocean current energy that may generated by multiple sources

including the Coriolis effect and differences in temperature and salinity, the wave energy mainly comes from the wind induced surface waves of the ocean. However, due to multiple reasons including the irregularity of the wave forces and the harsh ocean environment, the technology of ocean wave energy harvesting is still not mature enough to reach to an acceptable Levelized Cost of Energy (LCOE) to be commercially deployed and adopted widely.

1.1.2 Classification of wave energy converter (WEC)

The history for adopting ocean wave energy can be traced back to the year of 1799, where a father and his son patented their design for harvesting energy from ocean waves [7]. Yet after that, the research on extracting energy from ocean wave did not brought much attention until the 1970s when the world oil crisis happened and people started to look for other resources of energy to replace the oil [8]. The European countries are the most active ones, the earliest countries that foster the advancement of this technology through government funding with plan include Norwegian, Portugal and the United Kingdom. As a result, a lot of concepts with different ideas for harvesting wave energy have been developed and many prototypes are developed and tested since then. Since these concepts adopted different designs and principles, they are further classified into sub-categories.

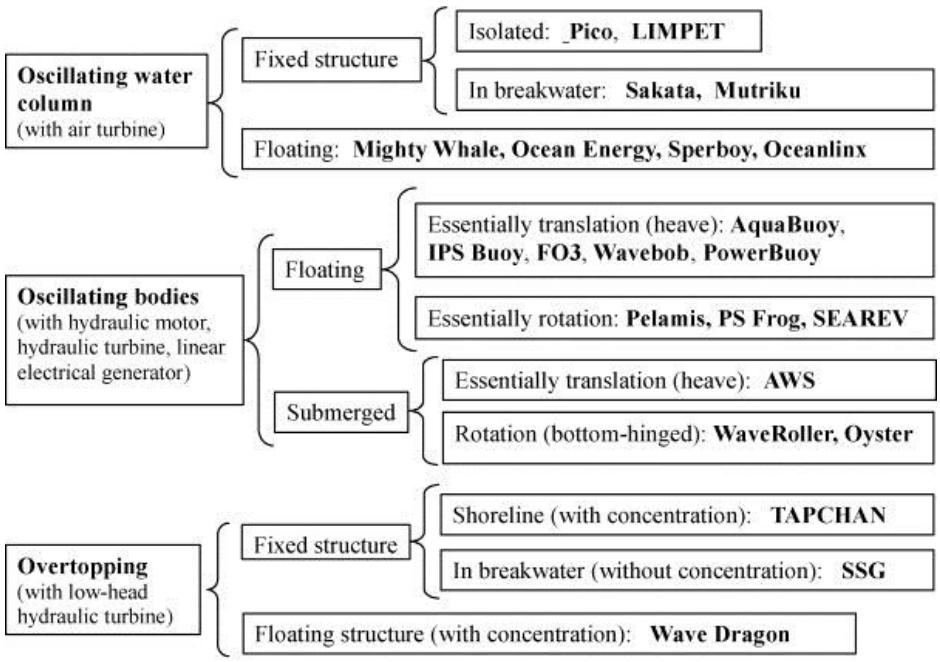

Figure 1-2 Classification of wave energy converters based on Falcao [9]

According to Falcao, who is one of the most well-known pioneers in the field of wave energy conversion, most types of wave energy converter can be classified into three categories, the oscillating water column, the oscillating body device and the overtopping device, which can be found in Figure 1-2.

The oscillating water column (OWC) is the earliest concept for wave energy conversion [10]. The OWC uses a chamber that is half submerged in the ocean, when the ocean wave raises and falls, the inner air pressure of the chamber changes with the water level, and the pressure change can be used to power an air turbine and drive the generator to generate electricity [11]. The OWC can either be a floating type or a fixed type based on the supporting structure it possess. The top of Figure 1-3 shows a fixed type of OWC where a structure is fixed to the seabed for mounting the device, whereas in the bottom of Figure 1-3, the device is floating on the surface of the ocean with an floater to provide extra buoyance force.

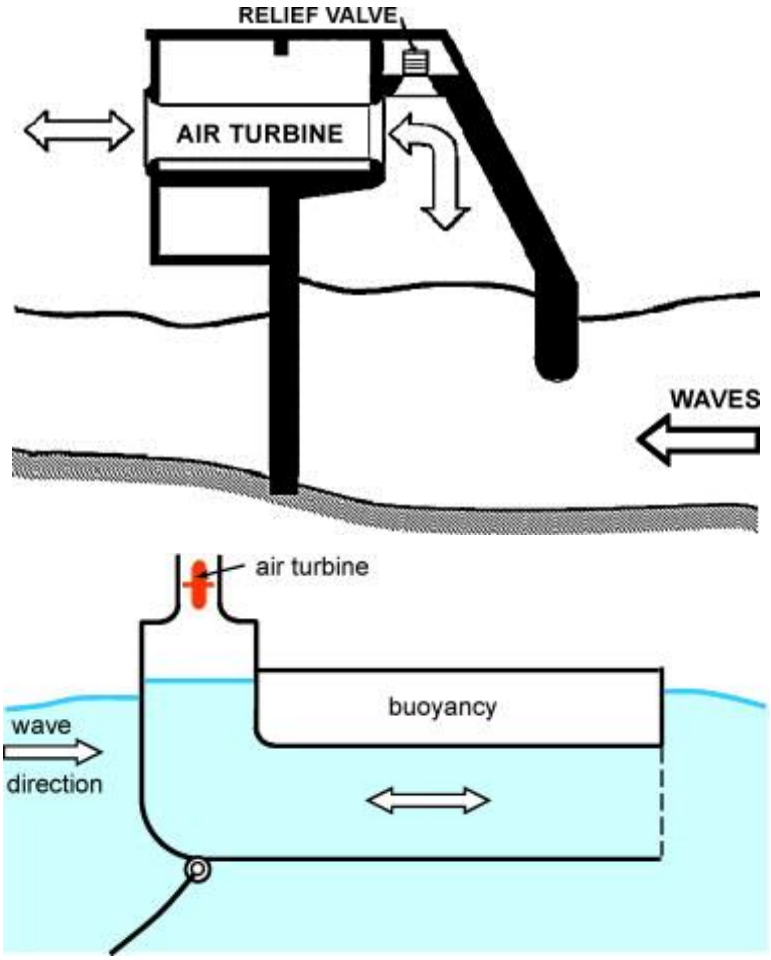

Figure 1-3 Top: Fixed type of OWC; Bot: Floating type of OWC

The oscillating body device is another widely used concept where the body (either floating or submerged) is driven by the natural oscillatory movement of the ocean wave, the kinematic energy stored in the body during that motion is then transferred into electricity using other approaches, which may be hydraulic motor, linear generator or hydraulic turbines. The oscillating body device can also be further categorized, either based on whether it is floating of the surface, or based on which wave motion it majorly adopts to harvest energy. For example, a typical point absorber illustrated in Figure 1-4 on the left is the one that float on the surface of the ocean and harvest the wave energy in heave motion, a surge device as illustrated in Figure 4 on the right is the one with a flap that adopts the surge motion of the wave to generate electricity [12] [13].

Figure 1-4 Left: Wavebob, a typical point absorber; Right: Oyster, a wave surge device designed for shallow water use

A overtopping device is the one which usually with long arms to concentrate the wave so that the concentrated part of water can have higher crest, the crest is then stored to the device and the potential energy stored in the high water level is then used to generate electricity. A highly representative one is the Wave Dragon that was deployed in Denmark for several year, which is illustrated in Figure 1-5 [14].

Figure 1-5 Overtopping device Wave Dragon prototype deployed in Denmark as proof of concept

1.1.3 Detailed introduction to point absorbers

Among all the different concepts, the author specifically focused on one type of WEC, which is the point absorber. The point absorber, which takes advantage of the oscillatory

up-and-down heave movement of the ocean waves, is one of the most prominent and widely adopted WECs for ocean power extraction. In 1975, Budal and Falnes raised the concept of extracting energy from ocean waves using a point absorber [15]. Later optimal conditions for point absorber power absorption were presented by Evans [16] and Mei [17], concluding that the maximum is achieved when the natural frequency of the floating buoy matches the excitation frequency of the incident waves. In real applications, however, the frequency of the incident wave can be as low as 0.1Hz, so the floating buoy demands a large body structure to match with that frequency, which is difficult, expensive, and even unrealistic [9]. To overcome this difficulty and try to match the natural frequency of the point absorber with the excitation frequency of the ocean wave, many ideas were explored. In 1982, Budal et al [18] proposed the design of a point absorber with optimum phase control using latching strategy. The power take-off (PTO) in their design is an air turbine. French and Bracewell [19] designed an internal mass to move against the heaving point absorber, and introduced springs with different stiffness to achieve phase control and to increase the total energy extraction. Later, various latching and declutching methods were proposed to reinforce the device to move in coherence with the wave and fulfill the frequency matching [20][21][22][23]. In addition to the theoretical studies, prototypes have been deployed and tested, these pioneering prototypes includes the one buoy with hemispheric bottom built by Falcao with hydraulic cylinders for energy conversion [24], the IPS buoy tested at Sweden in 1981 [25], and the AWS prototype which uses a linear direct-drive generator that later deployed in 2004 after two unsuccessful trials [26]. Figure 1-6 illustrates the concept where multiple of AWS buoy together build a wave farm [27].

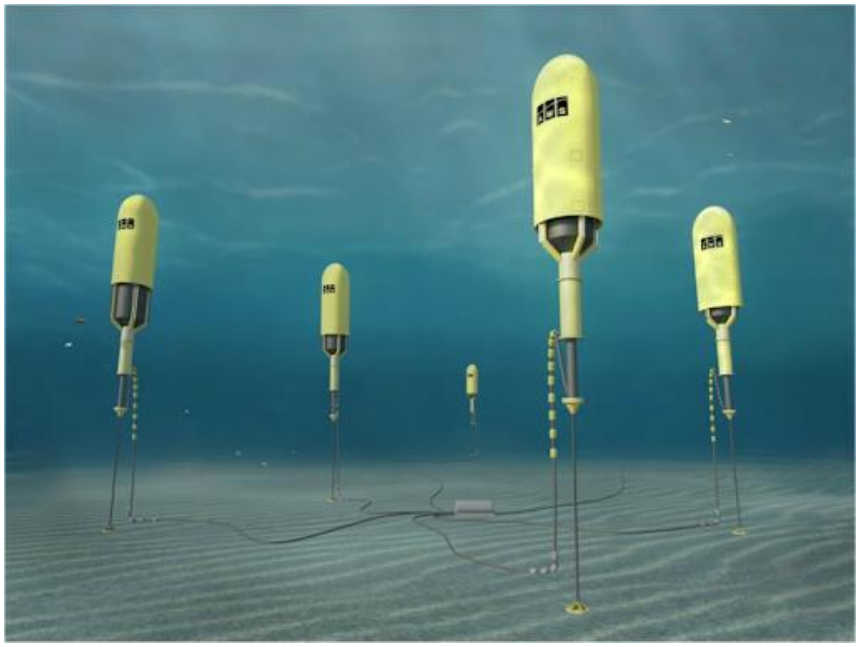

Figure 1-6 A wave farm consist of multiple AWS buoy

Besides the single-body designs with control that attempt to achieve frequency matching, another point absorber concept is to connect the floating buoy with a submerged body to form a two-body WEC. The two-body point absorber generates power from the self-reactive relative motion between the floating buoy and the submerged body without the requirement for an additional supporting frame. The natural frequency of the energy harvesting motion can be tuned through multiple approaches including changing the mass ratio between the two bodies and tuning the PTO damping coefficient. These advantages give the self-reactive two-body point absorber certain flexibility and simplicity during the design and deployment. Researchers have analyzed the two-body self-reactive point absorbers. As a pioneer on this topic, Falnes investigated the two-body WEC system and concluded that, for an axisymmetric system utilizing heave motion, it is possible to achieve the maximum power absorption and that the equivalent excitation force can exceed the excitation force on either body [28]. Beatty et al [29] calculated the optimum natural frequency for the submerged body and found a significant energy increase by altering this natural frequency. Liang and Zuo [30] explored the effects of different mass ratios between the submerged and floating bodies and found the optimum and sub-optimum conditions for energy absorption for both regular and irregular waves. Korde [31], Babarit [32], Candido and Justino [33], Yu and Li [34] and Shami et al [35] also contributed to the theoretical

study of the system in different aspects. At the same time, large prototypes using the concept of the self-reactive structure have been tested or deployed in the ocean. The most well-known prototypes include those developed by WaveBob [12], SeaBeavl [36], and Ocean Power Technologies which is illustrated in Figure 1-7 [37].

Figure 1-7 An Ocean Power Technology's PB3 power buoy is under sea trial

1.1.4 Power take-off (PTO)

The power take-off (PTO), which is the mechanism whereby a WEC extracts energy from the waves and converts it into electricity, is widely recognized as one of the most critical component in the ocean wave energy technology [38]. A PTO must have the following features: high energy conversion efficiency, high performance predictability, high system reliability and low maintenance. These properties are essential for potential commercialization [39]. Knowing the importance of PTO, researchers have come up with a broad range of concepts. Some of those ideas have already been adopted and prototyped and have yielded reasonable results [9][40]. With its high load capacity and maturity, the hydraulic PTO has been a popular choice. It is typically composed of hydraulic pumps, high-pressure pipes, pressure accumulators, hydraulic motors, and electrical generators [41]. Henderson has developed a WEC named Pelamis using a hydraulic PTO, the 1/7 scale prototype was tested in a water tank and achieved satisfying energy conversion efficiency

[42]. More contributions of hydraulic PTO can be found in the work published by Falcao [43], Bjarte-Larsson and Falnes [44], and Gaspar et al [45]. Another widely adopted concept is a direct drive PTO implemented with a linear generator. Research on this typical PTO usually include a point absorber where the direct drive PTO can take advantage of the motion without intermediate mechanisms, simplifying the system and helping reliability. Elwood et al [46] developed a two-body WEC with a specially designed linear generator PTO and tested in the ocean, yet the results were not satisfying. Lejerskog et al designed and tested a direct drive single body point absorber where the rope drives the PTO [47]. Uppsala University built a full scale point absorber with linear generator as PTO and conducted sea trial, which is illustrated in Figure 1-8 [48]. Muller [49], Vermaak and Kamper [50], and Eriksson [51] also made contributions on this issue. However, the different PTOs all have notable defects. The hydraulic PTOs all share the challenge of system complexity that reduces the efficiency and creates reliability concerns for the components. Direct drive PTOs gain from a simpler structure, but the permanent magnetic generator suffers from the low speed operation due to the reciprocating motion of the ocean waves, undermining the overall PTO efficiency.

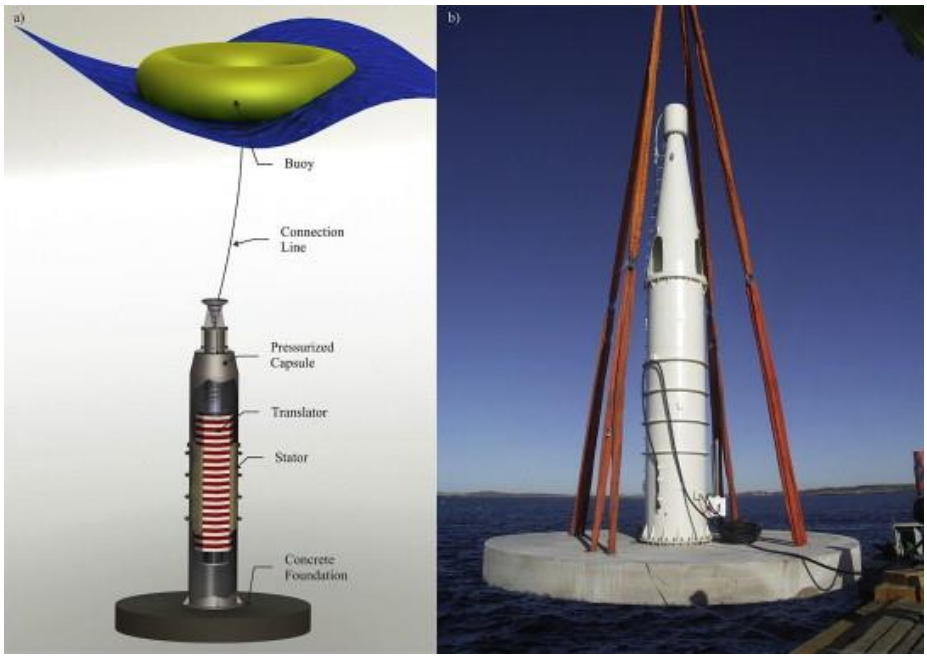

Figure 1-8 Linear generator PTO used in a point absorber built by Uppsala University [48]

1.2 Objective

The overall objective for this dissertation is to improve the power absorption of the WECs from ocean waves through innovative design, theoretical analysis and optimization. To achieve this target, multiple objectives need to be achieved.

The first objective of this dissertation is to come up with a design of the PTO that can solve the current issue on the PTO. As it is brought up in the last section, and the pioneer of the ocean wave energy research Falcao denoted "The power equipment (PTO) is possibly the single most important element in wave energy technology, and underlies many (possibly most) of the failures to date" [9]. It is self-evident that the designing a PTO with high reliability and energy transfer efficiency for harvesting the ocean wave energy is of great importance.

The second objective of the dissertation is to verify the frequency matching effect of using a self-reactive structure for the point absorber. Due to the low excitation frequency of the ocean wave, the floater need to be designed with huge dimension so it can achieve frequency matching. By adding a reactive body, the structure should be able to match any frequency through parameter adjusting, yet this hypothesis still lack of verification and need to be proved.

The last objective of the dissertation is to achieve optimum power absorption through parameter optimization. By tuning the parameters in the design of PTO and the WEC and find the optimized parameter either analytically or numerically. It can be expected that the optimum power for different wave conditions can be acquired.

1.3 Contribution

The major contribution of the dissertation consist of several aspects:

- The design of a compact mechanical PTO using MMR mechanism which can transform the reciprocating bi-directional linear motion of the ocean wave excitation into uni-directional rotation of the generator is introduced in the dissertation.
- A comprehensive study on the MMR PTO is conducted both analytically and experimentally. Multiple prototypes in different scale are developed and tested in various environment including dry lab and wave tank. The major design parameters

that can influence the performance of the MMR PTO is explored and discussed with the support of the experiments.

- A self-reactive point absorber is designed to assemble with MMR PTO, the optimum power absorption for the point absorber under different wave conditions are derived. The influence of the inertia of the PTO and the drag damping coefficient of the second body is explored.
- Through wave tank test, a point absorber with different constraint is tested under different wave conditions. The advantage of the self-reactive structure for the point absorber is experimentally verified.

1.4 Overview

The dissertation is organized as follows:

In chapter two, the design of the self-reactive with MMR PTO is introduced, the working principle and advantages for both the MMR PTO and the self-reactive point absorber are explicitly explained.

In chapter three, the dynamic analysis for the self-reactive point absorber with MMR PTO is established, and the theoretical optimum for the proposed WEC under different wave conditions is derived.

In chapter four, the dry lab experiments of the MMR PTO is conducted. Through dry lab bench testing, the MMR mechanism is verified, the dynamic model of the MMR PTO is refined with the observed test results.

In chapter five, a wave tank test for the proposed self-reactive point absorber with MMR PTO is conducted.

In chapter six, the dissertation is concluded and the potential works that can be extended from the dissertation are introduced.

2. Design and development of the self-reactive point absorber with MMR PTO

2.1 Chapter Introduction

As the pioneer of the ocean wave energy research Falcao denoted “The power equipment (PTO) is possibly the single most important element in wave energy technology, and underlies many (possibly most) of the failures to date” [9]. It is self-evident that the designing a PTO with high reliability and energy transfer efficiency for harvesting the ocean wave energy is of great importance. In the chapter, a PTO using mechanical motion rectifying (MMR) mechanism is introduced. This mechanism can transform the bi-directional linear motion of the ocean wave into the uni-directional rotation of the generator. It is designed to improve the efficiency as well as reliability of the current existing PTOs with a simple compact structure. The working principle as well as the advantage of the design are introduced explicitly, multiple prototype types are developed to prove the concept and verify the performance.

Besides the PTO design, due to the low excitation frequency of the ocean waves in nature, it is impractical and economically unworthy to build a single body floating structure that has a natural frequency that matches with the wave excitation frequency [52]. To solve this problem, a two body self-reactive structure is adopted in the design of the point absorber by adding a submerged body. Through analysis, the effect of a two body structure is introduced analytically and the WEC is prototyped for further verification.

2.2 Design of the MMR PTO

2.2.1 Detailed design of the MMR PTO

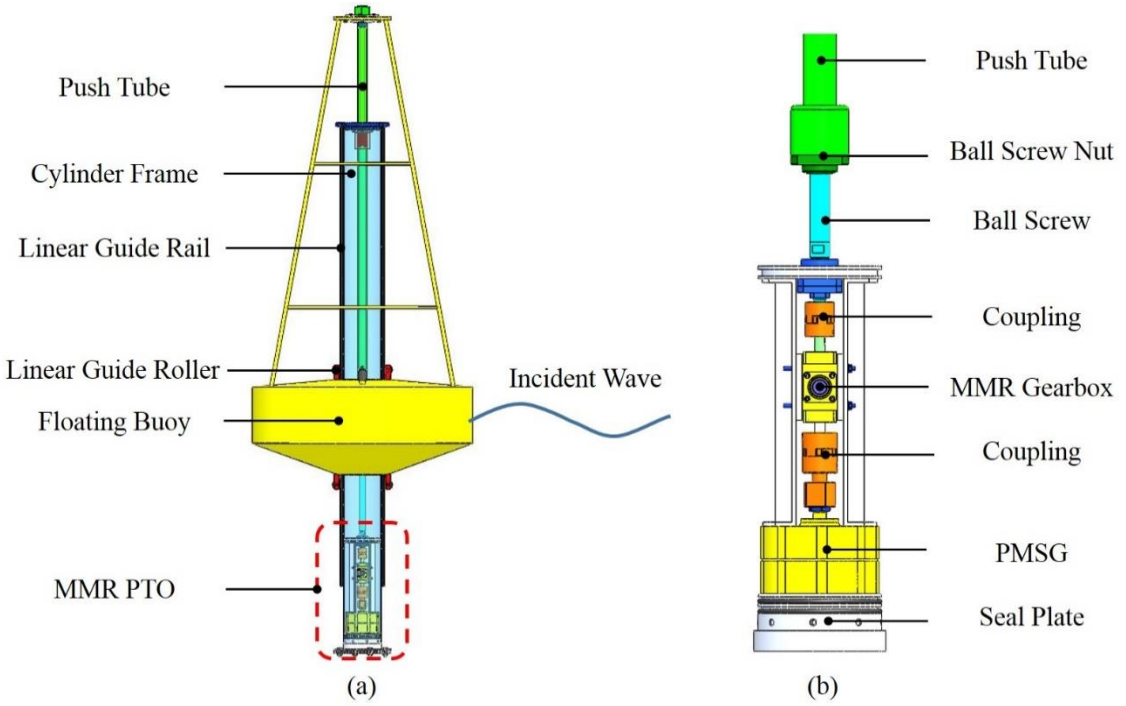

Figure 2-1 Design of a point absorber with MMR PTO

The design of the proposed PTO is shown in Figure 2-1. A point absorber in Figure 2-1(a) is designed to harvest energy from the heave motion of the ocean wave as illustrated, with the buoy floating on the ocean surface and the cylinder fixed (single-body WEC) or connected to a submerged body (two-body WEC). The buoy can move along the cylinder under the excitation of the incident wave to generate relative motion between the buoy and the cylinder. A push-pull tube connected with the buoy will drive the ball nut on the bull screw, as illustrated in Figure 2-1(b). The proposed MMR PTO consists of a ball screw for linear-to-rotary motion transforming, an MMR gearbox for changing the bidirectional rotation into unidirectional rotation, and a permanent magnet synchronous generator (PMSG) for generating electricity. The relative heave motion between the floating buoy and the cylinder drives a tube to perform linear push and pull motion, in which the tube is rigidly connected with the ball screw nut. The ball screw is then driven reversely and generates bidirectional rotation from the oscillatory wave motion. The bidirectional

rotation is then rectified through the MMR gearbox into unidirectional rotation, and at last, rotates the PMSG for generating electricity.

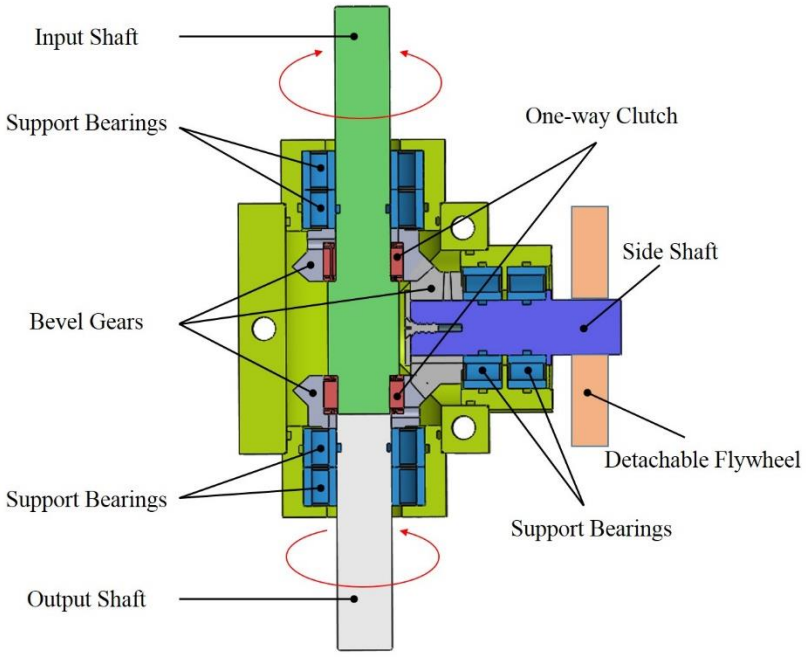

Figure 2-2 The detailed design of the MMR gearbox;

The detailed schematic of the MMR gearbox is illustrated in Figure 2-2. The MMR gearbox consists of one input shaft, one output shaft, one side shaft, three bevel gears, two one-way clutches, and several supportive bearings. The input shaft is connected to the ball screw and inputs the bidirectional rotation into the gearbox. The one-way clutches are embedded between the input shaft and the bevel gears in opposite directions. The one-way clutch allows only relative rotation in one direction and locks the other direction. As illustrated in Figure 2-2, when the input shaft is rotating in one direction, the top one-way clutch is engaged, and the bottom one-way clutch is disengaged. Through the transmission of the three gears, the rotation direction is changed into a reversed direction against the input shaft. When the input shaft is rotating in another direction, however, the top one-way clutch will disengage and the bottom one-way clutch will engage, so the input shaft is capable of driving the gear directly, and the output of the gearbox is still in the same direction as the input shaft. As a result, the bidirectional rotation input towards the gearbox is transmitted into the unidirectional output of the gearbox. One noticeable phenomenon of the MMR gearbox is that the one-way clutch locks the relative motion rather than the absolute motion.

So when the output side of the MMR gearbox has a higher rotating speed than the input side, both one-way clutches are disengaged and the generator will continue rotating (freewheeling) under the rotational inertia till the input speed and the generator speed are the same again. This phenomenon of decoupled freewheeling motion grants the MMR gearbox with unique dynamic performance that can improve the efficiency at low rotation speed and higher reliability on components, which is introduced in detail in the next paragraph.

2.2.2 Reliability analysis on the MMR PTO

The reliability of the PTO can be separated into two topics, one is the system level of reliability, and the other is on the component level [53]. On the system level, the MMR system, apparently, has more components, and may bring the system some disadvantages, for instance, more failure modes and higher failure chances if all the components all share same designed lifespan and distribution of failure chances. However, it is also very important to improve the reliability of each components individually, so that it statically can service longer time period and not fail due to fatigue under the similar load, and the advantages of the MMR mechanism come from that. Firstly, for the non-MMR PTO, the load is in alternating condition, whereas the components of the MMR PTO are under uni-directional torque load. The Goodman Diagram is presented below to further explain the case,

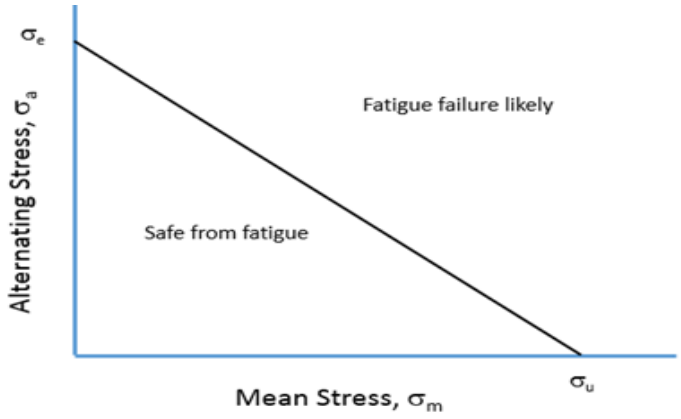

Figure 2-3 The Goodman Diagram.

Figure 2-3 shows the Goodman diagram which shows the safety region for the component under either the alternating stress or regular stress [54][55]. The straight line is the critical safe line. The zone below the line is considered to be safe and above the line is considered likely to fail of fatigue

In the figure,

- σ_a is the alternating stress
- σ_e is the endurance stress limit
- σ_m is the mean stress
- σ_u is the ultimate stress

For most of the components, the ultimate stress σ_u is larger than the endurance stress limit σ_e. If we assume the components are working under the stress of the endurance stress, for the non-MMR system, the mean stress is zero and the alternating stress is the same as the endurance stress. For the MMR case, however, the mean stress is half of the endurance stress and the alternating stress is also half of the endurance stress for the torque is rectified and on one direction only. The relationship can be presented as below:

$$\sigma_{m_{nonmmr}} = 0, \sigma_{a_{nonmmr}} = \sigma_e$$

$$\sigma_{m_{mmr}} = \frac{\sigma_e}{2}, \sigma_{a_{mmr}} = \frac{\sigma_e}{2}$$

This relationship is illustrated in Figure 2.4.

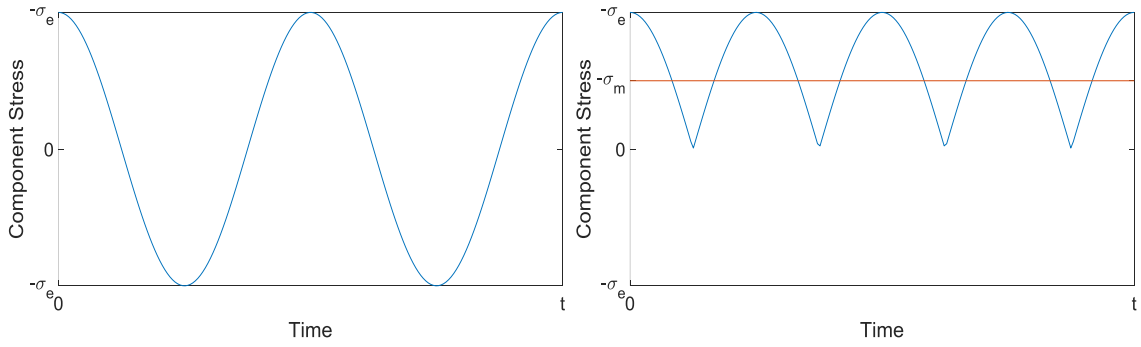

Figure 2-4 Left: The stress plot of non-MMR PTO; Right: The stress plot of MMR PTO

If draw two points of the both MMR PTO and non-MMR PTO on the Goodman Diagram, the point of the non-MMR PTO is on the point of $(0, \sigma_e)$ whereas the MMR PTO is on $(\frac{\sigma_e}{2}, \frac{\sigma_e}{2})$, As the ultimate stress σ_u is larger than the endurance stress limit σ_e, the point of

MMR PTO should be below the straight line and on the safe zone as illustrated in Figure 2-5. Indicating that on the component level, the design of MMR mechanism can help to improve the components' fatigue life. In addition, for the one-way clutches and gears of the MMR PTO, the designed load is only on half of the cycles, which can also improve the lifespan of the MMR PTO.

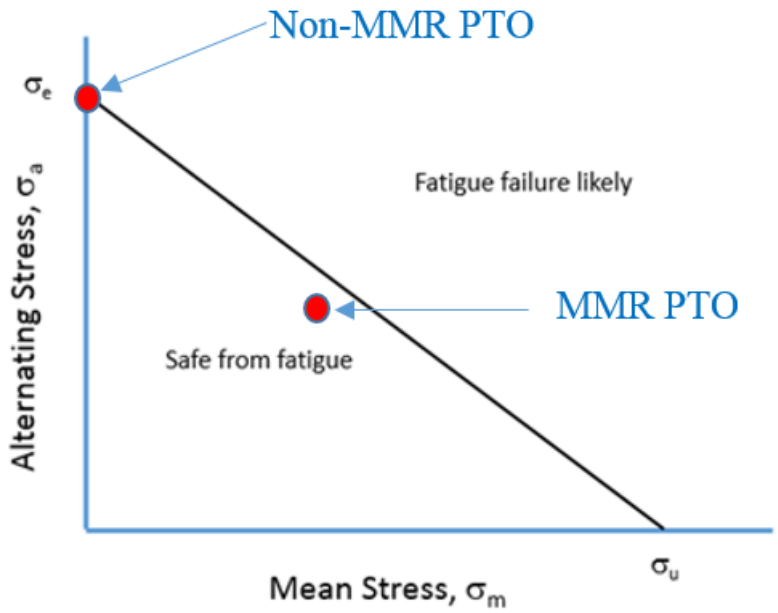

Figure 2-5 Non-MMR PTO and MMR PTO on the Goodman Diagram

2.2.3 Developed prototypes

Three prototypes with various sizes are developed during the project. The first one is a small size prototype rated at 50W and worked as the proof of concept which is shown in Figure 2-6. Figure 2-7 and Figure 2-8 shows another two prototypes developed, one at 500W and another at 10kW. These prototypes are used at different stages of the projects and tested to verify theoretical analysis.

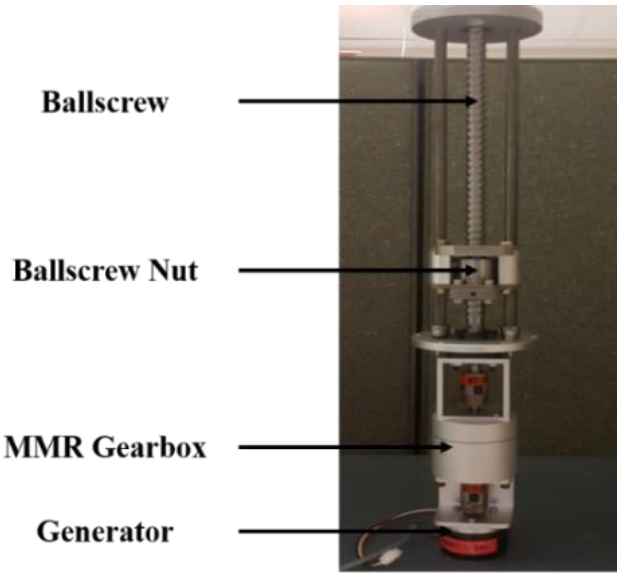

Figure 2-6 A 50W MMR PTO prototype that works as proof of concept

As illustrated in Figure 2-6. The 50W prototype is the earlist prototype developed to verify the concept of MMR PTO. Unlike the structure introduced above, the ball screw is not embeded inside a push tube. Two push tubes on the side are connected with the ball screw nut through a supporting structure. This design is more complicated than the design introduced above, hence more components are required. The components for the 50W prototype are mostly machined using a in-lab CNC and not much measurement was conducted onto the machine. As a result, the precision of the prototype is not very good and the prototype is only used for proof of concept.

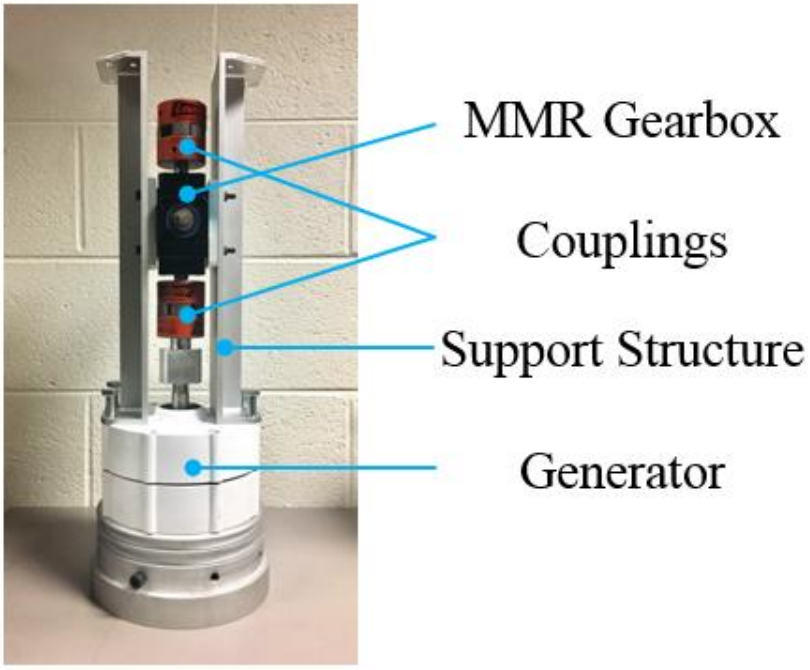

Figure 2-7 A 500W MMR PTO prototype

Figure 2-7 shows the prototype of the 500W PTO, which is the one depicted in the start session of this chapter. Different from the 50W prototype that used more as a proof of concept, the 500W used a more compact design and more commercial components to guarantee the precison of the mechanical parts so the mechanical efficiency of the PTO can be improved.

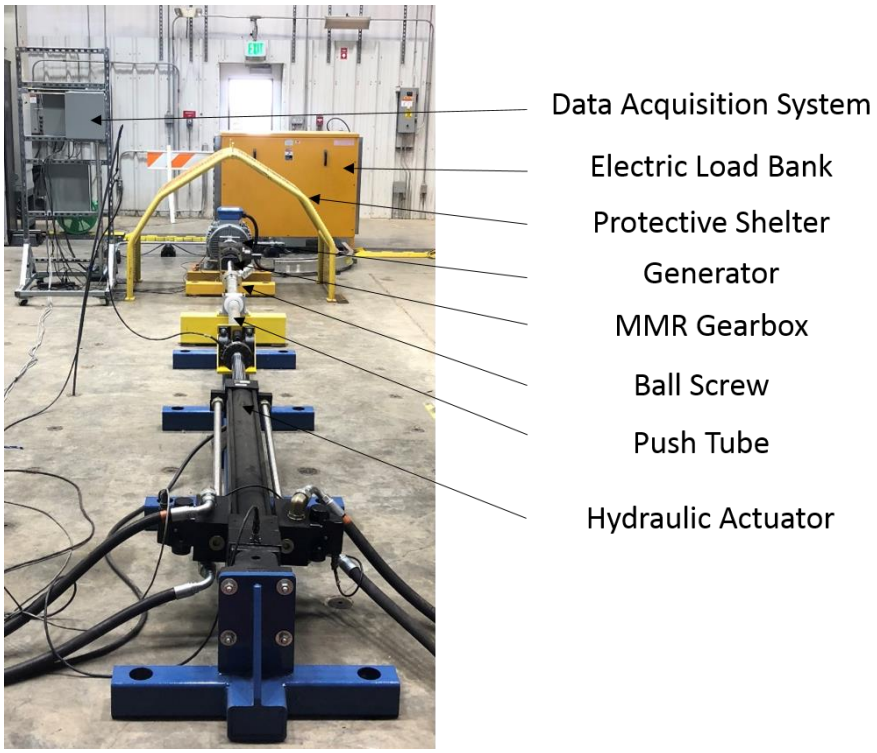

Figure 2-8 A large scale 10kW MMR PTO placed in horizontal direction

Figure 2-8 shows the largest prototype introduced in this dissertation, which is a 10kW prototype that is designed for reliability testing. Different from the previous two prototypes, the 10kW prototype is designed to be deployed in horizontal direction. The reason is the hydraulic linear actuator that is capable of testing the prototype in this scale need to be placed in horizontal direction. As a result, the supporting structure is redesigned to match with the testing condition.

2.3 Design of the Self-reactive Point Absorber

2.3.1 Design and analysis on the single body point absorber

One of the most direct and simple concept for harvesting energy from ocean wave is by applying to floater on the surface of the ocean to move along with the wave. The kinematic energy of the floater can be used to drive a generator for electricity.

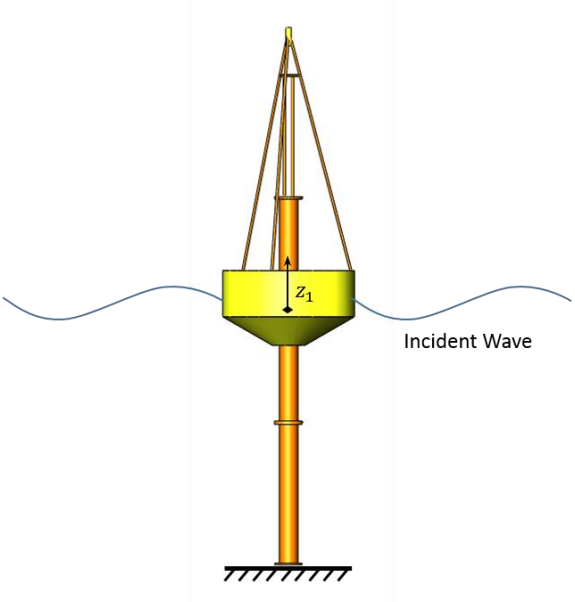

Figure 2-9 Concept illustration of the single body point absorber

Figure 2-9 illustrates the concept of a single body point absorber, where the floating buoy moves along a fixed structure under the excitation of the ocean wave. The free body diagram for the single body point absorber can be find in Figure 2-10.

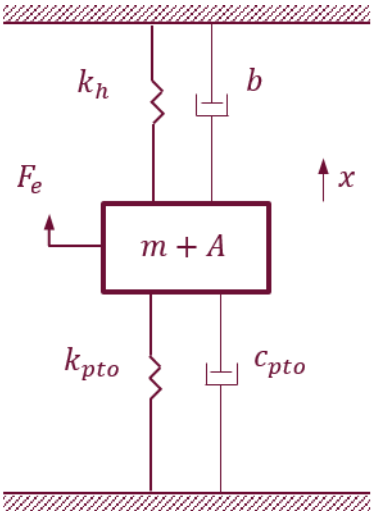

Figure 2-10 Free body diagram for the single body point absorber

In the free body diagram [56],

- x is the vertical coordinate (heave) of the buoy
- m is the dry mass of the buoy
- A is the heave induced added mass
- b is the heave induced radiation damping coefficient
- F_e is the heave induced excitation force
- k_h is the hydrostatic stiffness
- c_{pto} is the PTO linear damping coefficient
- k_{pto} is the PTO linear spring stiffness

The equation of motion can then be described as:

$$(m + A)\ddot{x} + (c_{pto} + b)\dot{x} + (k_{pto} + k_h)x = F_e \qquad \textit{E. 2-1}$$

Assuming the single body point absorber works in the regular wave case, the frequency domain excitation force of and the response displacement of the floating buoy can then be described as:

$$F_e = f_e e^{j\omega t} \qquad \textit{E. 2-2}$$

$$X = Xe^{j\omega t} \qquad \textit{E. 2-3}$$

With this assumption, the analytical solution for the displacement of the floater can be written as:

$$X = \frac{f_e}{-\omega^2(m+A)+j\omega(c_{pto}+b)+(k_{pto}+k_h)} \qquad \textit{E. 2-4}$$

To resonant natural frequency of the point absorber can be derived as:

$$\omega = \omega_n = \sqrt{\frac{k_{pto}+k_h}{m+A}} \qquad E.\ 2\text{-}5$$

To achieve the optimum power, plug in the equation for natural frequency with power,

$$P_{ave} = \frac{1}{2} c_{pto} \frac{{f_e}^2}{(c_{pto}+b)^2} \qquad E.\ 2\text{-}6$$

It is easy to derive that the optimum power can be achieved when the PTO damping efficient is the same with the radiation damping coefficient($c_{pto} = b$), and the power it can reach can be described as:

$$P_{ave} = \frac{1}{2}\omega^2 c_{pto}|X|^2 = \frac{1}{8b}{f_e}^2 \qquad E.\ 2\text{-}7$$

This result shows that for the single body point absorber, the optimum power can be acquired when the frequency dependent parameters of the floating buoy is known [15][31]. However, in real world situations, the excitation frequency of the ocean wave is usually very low, the typical wave frequency can be ranging between 0.07 Hz and 0.25 Hz, which will lead to a huge dimension for the point absorber to achieve frequency match with the ocean wave [9]. For the increase in dimension does not only change the mass and added mass of the point absorber, but also change the hydrostatic stiffness. According to Falcao [9], for a hemispherical buoy, the optimal radius to achieve resonance in regular waves with a frequency of 0.1 Hz is 26.2m. Building a buoy with that size will bring in difficulties in manufacturing, transportation, deploying, as well as maintenance. As a result, it is impractical for the single body point absorber to be adopted widely for real-world applications.

2.3.2 Design and analysis on the two body self-reactive point absorber

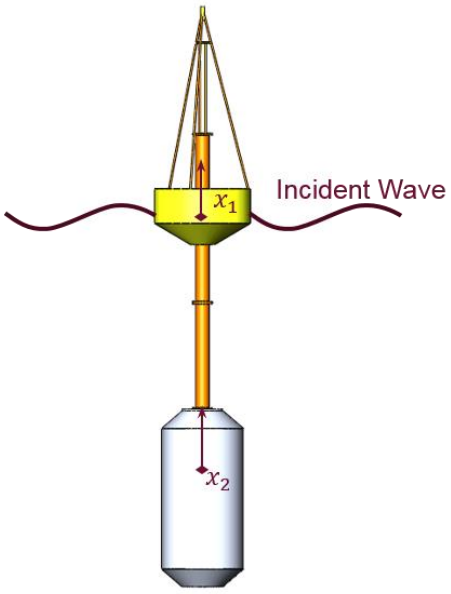

Figure 2-11 Concept illustration for the two body self-reactive point absorber

As a result, another approach has been come up to achieve frequency matching with the excitation of the ocean wave. By adding a submerged body towards the buoy and generate relative motion between the two bodies, another natural frequency between the relative motion of the two bodies is added and can be tuned to match with the wave frequency. Since the added submerged body is a part of the WEC, and the reactive motion for the WEC is between the floating buoy and the submerged body, the two body WEC is called as self-reactive point absorber. Figure 2-11 shows an example of a self-reactive point absorber where a tank shape second body is added to the WEC.

The free body diagram for a typical two body self-reactive point absorber can be found in Figure 2-12. Since it is considered to be working in an ideal case, the influence between the two bodies are considered small and the drag damping is ignored as well for simplification [56].

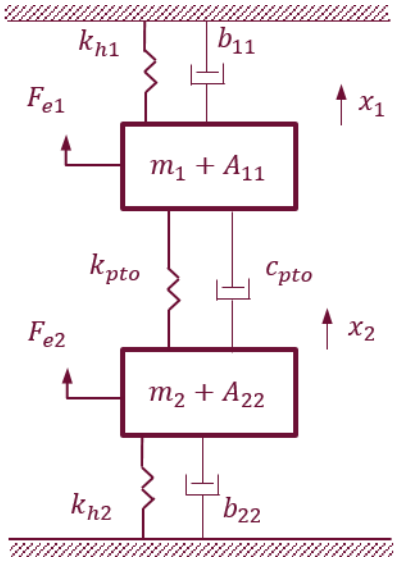

Figure 2-12 Free body diagram for the two body self-reactive point absorber

• $x1$ and $x2$ are the respective displacement in heave of the buoy and submerged body

• $m1$ and $m2$ are the respective dry body masses of the buoy and submerged body

• $A11$ and $A22$ are the respective added masses of the buoy and submerged body

• $b11$ and $b22$ are the respective radiation damping of the buoy and submerged body

• $Fe1$ and $Fe2$ are the respective excitation forces on the buoy and submerged body

• $kh1$ and $kh2$ are the respective hydrostatic stiffness's of the buoy and submerged body

• $cpto$ and $kpto$ are the linear PTO damping coefficient and spring stiffness

The equation of motion for the two body self-reactive point absorber can then be described as:

$$(m_1 + A_{11})\ddot{x}_1 + A_{12}\ddot{x}_2 + (c_{pto} + b_{11})\dot{x}_1 + (b_{12} - c_{pto})\dot{x}_2 + (k_{pto} + k_{h1})x_1 - k_{pto}x_2 = F_{e1} \quad \textit{E. 2-8}$$

$$(m_2 + A_{22})\ddot{x}_2 + A_{21}\ddot{x}_1 + (c_{pto} + b_{22})\dot{x}_2 + (b_{21} - c_{pto})\dot{x}_1 + (k_{pto} + k_{h2})x_2 - k_{pto}x_1 = F_{e2} \quad \textit{E. 2-9}$$

If the self-reactive point absorber is again assumed to be placed in the regular wave condition, the excitation force can be written in the form of

$$F_{e1}(t) = F_1 e^{j\omega t} \quad \textit{E. 2-10}$$

$$F_{e2}(t) = F_2 e^{j\omega t} \quad \textit{E. 2-11}$$

The solution for the displacement of the bodies in heave can be written as:

$$X_1(t) = X_1 e^{j\omega t} \quad \textit{E. 2-12}$$

$$X_2(t) = X_2 e^{j\omega t} \quad \textit{E. 2-13}$$

By reforming the equation of motion into matrix form, the new equation can be written as:

$$(-\omega^2 \boldsymbol{M} + j\omega \boldsymbol{C} + \boldsymbol{K})\boldsymbol{X} = \boldsymbol{F} \quad \textit{E. 2-14}$$

Here,

$$\boldsymbol{M} = \begin{bmatrix} m_1 + A_{11} & A_{12} \\ A_{21} & m_2 + A_{22} \end{bmatrix} \quad \textit{E. 2-15}$$

$$\boldsymbol{C} = \begin{bmatrix} c_{pto} + b_{11} + b_{v1} & b_{12} - c_{pto} \\ b_{21} - c_{pto} & c_{pto} + b_{22} + b_{v2} \end{bmatrix} \quad \textit{E. 2-16}$$

$$\boldsymbol{K} = \begin{bmatrix} k_{pto} + k_{h1} & -k_{pto} \\ -k_{pto} & k_{pto} + k_{h2} \end{bmatrix} \quad \textit{E. 2-17}$$

$$\boldsymbol{X} = \begin{bmatrix} X_1 \\ X_2 \end{bmatrix}, \boldsymbol{F} = \begin{bmatrix} F_1 \\ F_2 \end{bmatrix} \quad \textit{E. 2-18}$$

Similar to the single body point absorber, the objective of listing the function is to optimize the output power, where the objective function is:

$$Maximize\ P_{pto} = c_{pto}(\dot{x}_1 - \dot{x}_2)^2 \quad \textit{E. 2-19}$$

By expanding the equation of motion, the absorbed power can be rewritten as:

$$P_{ave} = \frac{1}{T}\int_0^T F_{pto}(\dot{x}_1 - \dot{x}_2)dt = \frac{1}{2}\omega^2 c_{PTO}|X_1 - X_2|^2 \quad \textit{E. 2-20}$$

In this equation, the relative motion between the two bodies can be given in a close-form solution,

$$|X_1 - X_2| = \left|\frac{p+jq}{(a+jb)c_{PTO}+(c+jd)k_{PTO}+e+jf}\right| \quad \textit{E. 2-21}$$

where,

$$p = (-\omega^2(m_2 + A_{22} + A_{21}) + k_{h2})F_1 + (\omega^2(m_1 + A_{11} + A_{12}) - k_{h1})F_2$$

$$q = \omega(b_{22} + b_{21} + b_{v2})F_1 - \omega(b_{11} + b_{12} + b_{v1})F_2$$
$$a = -\omega^2(b_{11} + b_{22} + b_{12} + b_{21} + b_{v1} + b_{v2})$$
$$b = -\omega^3(m_1 + A_{11} + A_{12} + m_2 + A_{22} + A_{21}) + \omega(k_{h1} + k_{h2})$$
$$c = b/\omega = -\omega^2(m_1 + A_{11} + A_{12} + m_2 + A_{22} + A_{21}) + (k_{h1} + k_{h2})$$
$$d = -a/\omega = \omega(b_{11} + b_{12} + b_{v1} + b_{22} + b_{21} + b_{v2})$$
$$e = \omega^4[(m_1 + A_{11})(m_2 + A_{22}) - A_{12}A_{21}] - \omega^2[(m_1 + A_{11})k_{h2} + (m_2 + A_{22})k_{h1} + (b_{11} + b_{v1})(b_{22} + b_{v2}) - b_{12}b_{21}] + k_{h1}k_{h2}$$

$$f = -\omega^3[(m_1 + A_{11})(b_{22} + b_{v2}) + (m_2 + A_{22})(b_{11} + b_{v1}) - A_{12}b_{21} - A_{21}b_{12}] + \omega[k_{h2}(b_{11} + b_{v1}) + k_{h1}(b_{22} + b_{v2})]$$

E. 2-22

By taking the derivative to both c_{PTO} and k_{PTO}, the optimum condition for each of the PTO component can be acquired with a close form solution, where,

$$k_{pto|opt} = -\frac{ce+df}{c^2+d^2} \qquad \textit{E. 2-23}$$

$$c_{pto|opt} = \frac{1}{\omega}\frac{|cf-de|}{c^2+d^2} \qquad \textit{E. 2-24}$$

The close-form results for the optimum power of the self-reactive point absorber can then be found as:

$$P_{ave|opt} = \frac{1}{4}\omega^2\frac{p^2+q^2}{|ae+bf|+(ae+bf)} \qquad \textit{E. 2-25}$$

With the solution for both the single body point absorber and two body point absorber acquired. Further compare between the two designs can be approached.

Figure 2-13 shows the comparison of the optimized power results of the single body and two body point absorber, together with the results for the two WECs when the stiffness of the PTO is zero. The mass-ratio is used as the scale for comparison. Here, the mass ratio is defined as the ratio between the total mass of the submerged body (added mass plus dry mass) and the dry mass of the top buoy. Through optimization, the optimum power of the two body self-reactive point absorber can reach to the optimum power of the single body

regardless of what mass ratio is picked. This indicate that when the PTO damping coefficient and the PTO stiffness is optimized, the single body and the two body point absorber shares the same power limit which is derived early by Falnes [57]. However, in real world cases, the mechanical PTOs discussed in this dissertation usually do not have a spring component to provide stiffness. Therefore the PTO stiffness k_{PTO} is usually zero. At this time, if the wave condition is decided in advance, the baseline is the power output of the single body WEC. Compared with the baseline, due to the self-reactive structure induced additional frequency, by choosing the mass ratio accordingly, the two body self-reactive point absorber can reach to the theoretical optimum power [30][58].

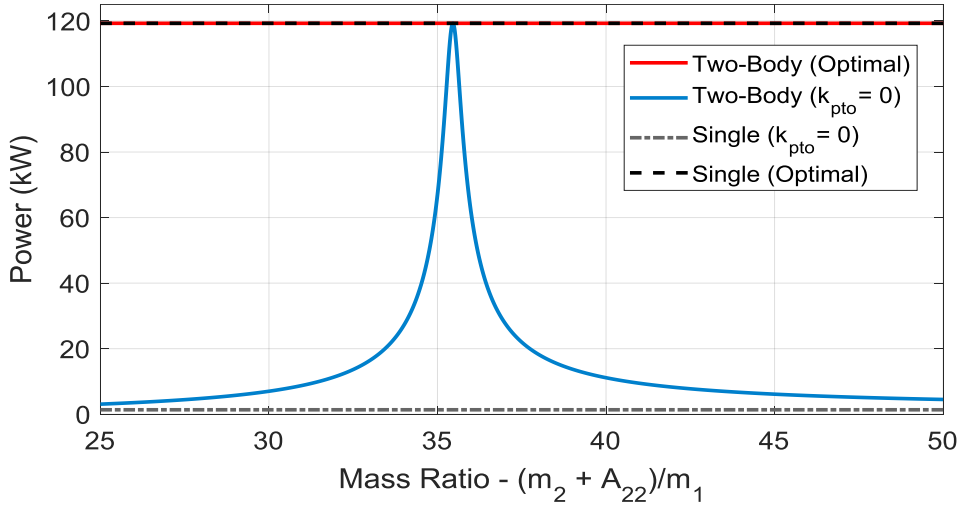

Figure 2-13 Power output solved analytically for the single body and two body point absorber

This result indicate that by adopting a self-reactive two body structure, even when the floating buoy has a relative small size in dimension and embedded with a realistic PTO without stiffness, it is still possible to achieve the theoretical optimum power.

The previous analysis proved the advantage of designing a submerged body for the point absorber, hence the submerged body is added to the design used in this dissertation. Figure 2-14 shows the manufactured floating buoy which is made by sheet aluminum, it is designed with an inner chamber so the dry mass of the floating buoy can be adjusted by filling in extra materials based on different requirement.

Figure 2-14 The manufactured floating buoy for the self-reactive point absorber

The submerged body shown in Figure 2-15 is built by assembling a commercial water tank with two metal sheet fabricated corn shape structure. The reason for choosing this shape will be introduced in the later chapter. Similar to the floating buoy, the water tank used in the submerged body can also be filled with other materials, so the mass of the second body can be adjusted in a range.

Figure 2-15 The manufactured submerged body for the self-reactive point absorber

2.4 Shape Optimization for the Submerged Body

Through frequency domain approaches, the power absorption of the proposed two body self-reactive point absorber can be acquired. Simulation can be conduct to optimize different parameters to achieve optimum power absorption for the WEC with MMR PTO. There exists multiple shapes for the submerged body in the two body point absorber design. For example, the Powerbuoy of the Ocean Power Technology company used a flat plate shape second body, whereas the Wavebob used a corn shape. However, there is not a certain consistent conclusion to decide which one can help the WEC to achieve more energy absorption. To decide this, three submerged bodies with different shapes are simulated using WEC-Sim in both regular and irregular wave conditions to detect the relationship between the different submerged body shape and power generation and optimize the WEC's performance.

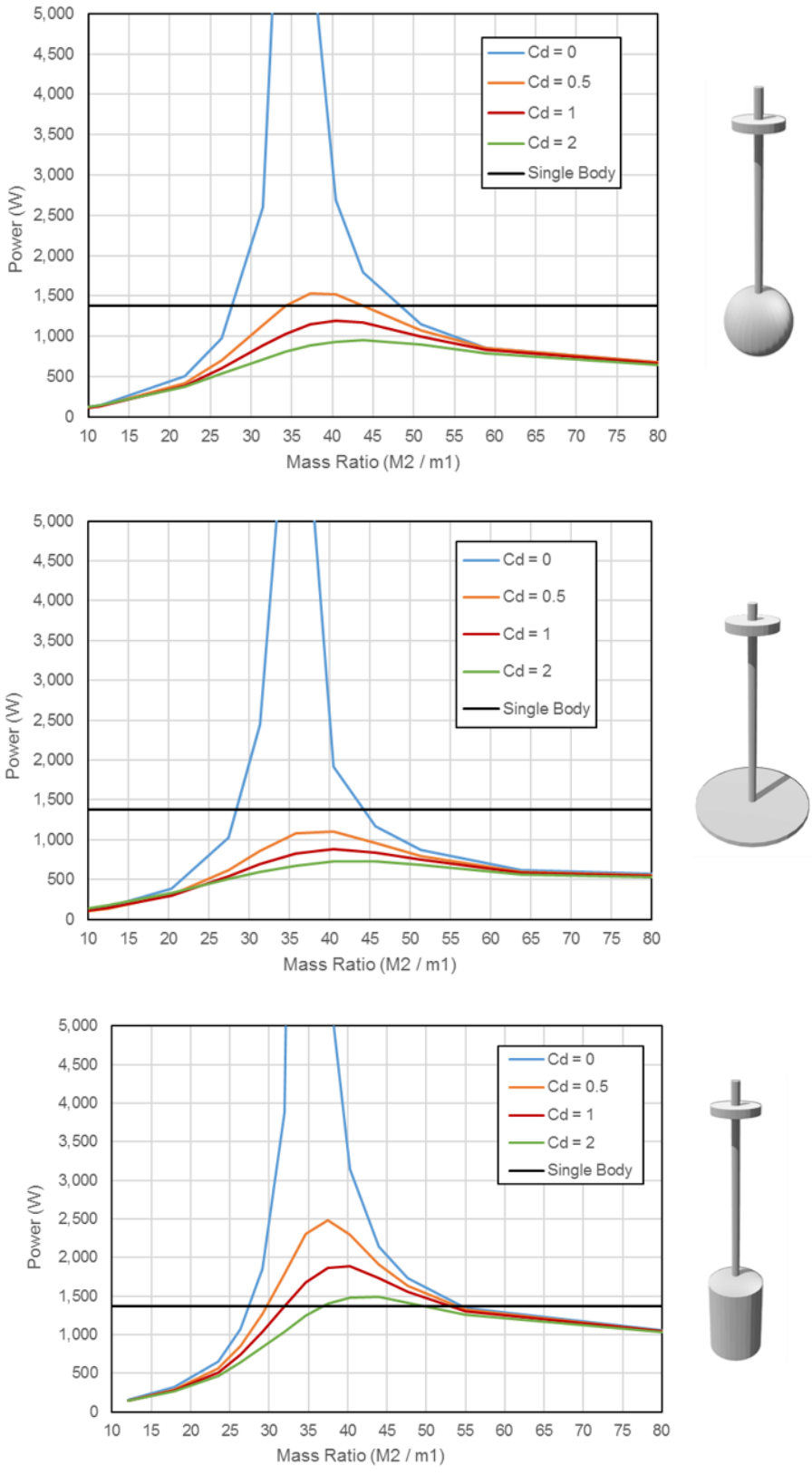

Figure 2-16 Compare of performance with different submerged body in regular wave

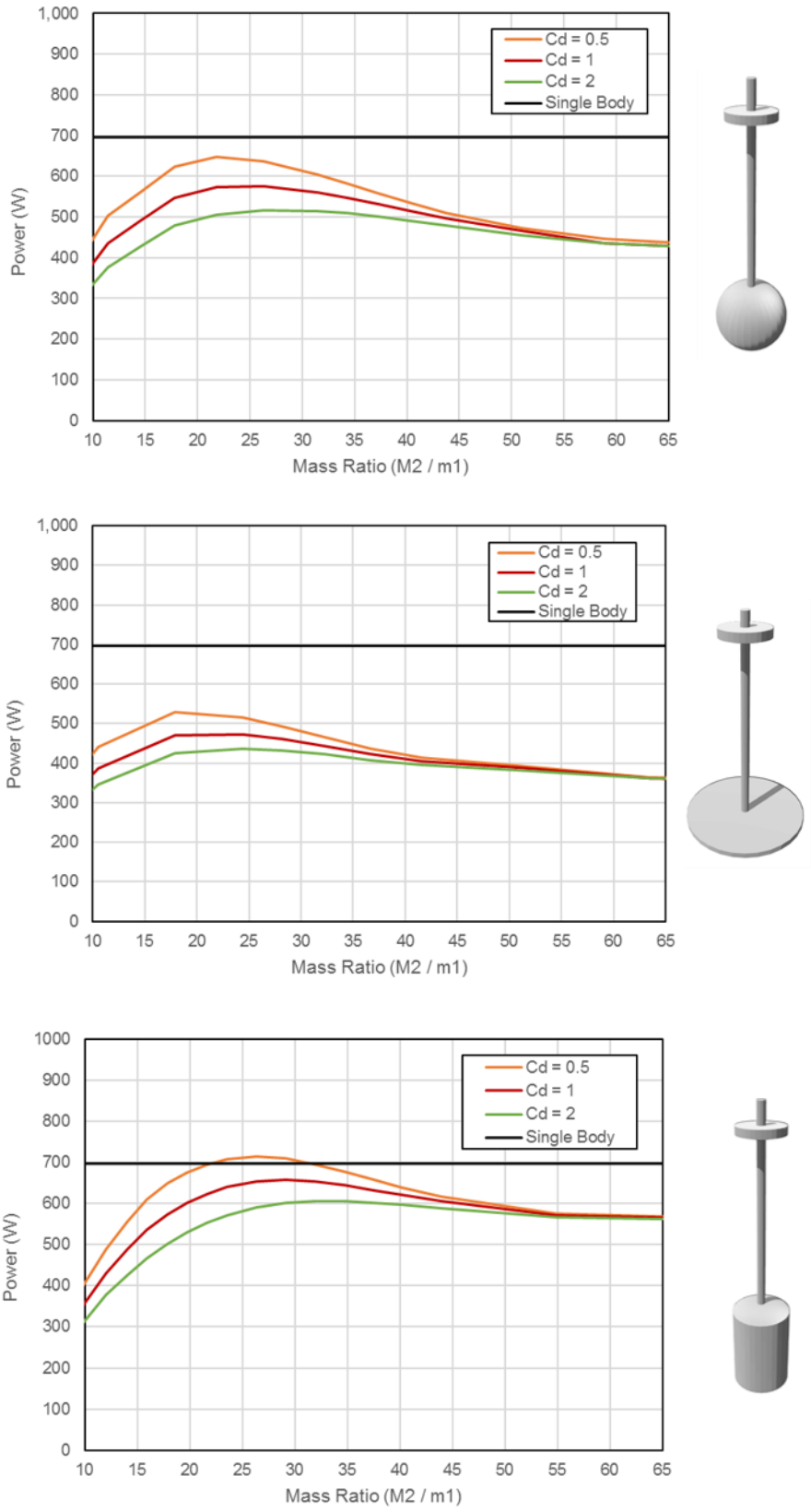

Figure 2-17 Compare of performance with different submerged body in irregular wave

The three different submerged body selected are a flat shape, a ball shape, and a water tank shape. The simulation is done based on the 1:20 scale prototype which has a 1.2m diameter for the floating buoy. For the regular wave test, the wave input parameter is with the period of 6s and the wave height is 1.5m. Different drag damping coefficient are also selected to find out the influence. In addition, similar comparison are made through irregular waves as well.

The results are shown in Figure 2-16 and Figure 2-17, and several conclusions can be observed as following:

The mass ratio between the submerged body and the floating buoy is important for obtaining the optimum power absorption and should be selected carefully to achieve best performance in the consideration of the typical wave conditions for the desired deployment location.

Drag damping can have a negative effect on extracting energy from the wave. With the increase of the drag damping coefficient, the overall absorbed power, especially the peak, decreased dramatically, which indicates that the drag damping effect should be minimized and keep the constant as small as possible.

The tank shape has the best performance as the second body for wave energy conversion. It possesses the highest power generation compared with the other two different submerged bodies regardless of which drag damping coefficient is chosen.

As a result, the tank shape is chosen as the standard submerged body in this research project and has been used in all the prototype.

2.5 Chapter Summary

In this chapter, the detailed design of the self-reactive point absorber with MMR PTO is introduced. The working principle of the MMR PTO is explained explicitly. The unique phenomenon of engagement and disengagement brought by the MMR mechanism is discussed. Moreover, the analysis on the difference between the single body and two body point absorber is made. The analysis show that the self-reactive structure can help the point absorber to achieve theoretical optimum power with small floating buoy size. At last, the study on the different body shapes are made, the results show that the tank shape second body can have the best effect among all the three second bodies tested.

3. Modeling, analysis, and optimization of the self-reactive point absorber with MMR PTO

3.1 Chapter Introduction

The design and development of the MMR PTO is introduced in the last chapter. To better understand the mechanism of the MMR PTO and how receive best results for absorbing power from ocean when it is paired with a self-reactive point absorber. It is necessary to conduct analytical study and build dynamic model to simulate the performance.

In this chapter, the dynamic modeling of the self-reactive point absorber with MMR PTO is established. Simulations based on the model are conducted to analytically describe the phenomenon that can happen during the operation. Through the simulation, the engagement and disengagement can be observed. The major parameters that can influence the performance of the MMR PTO are derived, and the influence of those parameters are solved analytically [59].

At last, through numerical optimization approach, the optimum power that can be achieved by a self-reactive point absorber with selected size is acquired. The optimum power for both the MMR PTO and the non-MMR PTO is compared, it can be found that the MMR PTO can help the point absorber to expand the frequency domain power absorption. The influence of different inertia of the PTO and drag damping coefficient are also explored. It is noticed that increasing the inertia can attribute to better power absorption for the MMR PTO, and the increase of the drag damping coefficient can be harmful for extracting power and should be reduced during the design process.

3.2 Modeling of the MMR PTO

The mechanical motion rectifying mechanism used in the MMR PTO has granted the PTO with some unique phenomenon and dynamic property, and a unique dynamic model is desired to depict the performance of the MMR PTO numerically [60][61]. The scheme for the MMR PTO is illustrated in Figure 3-1.

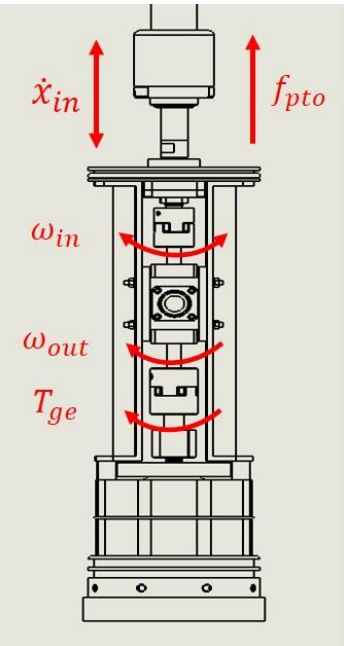

Figure 3-1 Scheme for MMR PTO

where,

- f_{pto} is the force on the PTO
- $\dot{x}_{in}$ is the input speed from the *relative* motion of the WEC to the ball screw
- ω_{in} is the input rotation speed from the ball screw to the MMR gearbox
- ω_{out} is the output rotation speed from the MMR gearbox to the generator
- T_{ge} is the reactive torque from the generator

The mathematical expression between ω_{in} and $\dot{x}_{in}$ involves the lead length of the ball screw l_{lead} as:

$$\omega_{in} = \frac{2\pi\dot{x}_{in}}{l_{lead}} \qquad E.\ 3\text{-}1$$

When the nut on the screw travels with a distance of l_{lead}, the ball screw rotates exactly one turn. When the rotation is directed to the three-phase AC generator, the voltage expression on each phase of the generator can be written as []:

$$\begin{cases} u_1 = k_e\omega_{out}\, sin(\omega_c t) \\ u_2 = k_e\omega_{out}\, sin(\omega_c t + \frac{2}{3}\pi) \\ u_3 = k_e\omega_{out}\, sin(\omega_c t - \frac{2}{3}\pi) \end{cases} \qquad E.\ 3\text{-}2$$

where,

- u_1 u_2 and u_3 are the induced electromagnetic forces (EMF) of each phase
- k_e is the voltage constant of the generator, unit V/rpm or V/rad/sec
- ω_c is the voltage angular frequency of the generator, which is the generator's rotation speed ω_{out} multiply by the pairs of the poles of the generator

The electric current on each phase of the generator shunted with a resistive load can be expressed by:

$$i_n = \frac{u_n}{(R_{in}+R_{ex})}\ ,\ (n = 1,2,3) \qquad \textit{E. 3-3}$$

where i_n is the current on each phase of the generator and R_{in} and R_{ex} are the internal and external resistances on each phase of the generator. Meanwhile, the current in d-axis is simplified to be zero to keep constant flux. The torque can then be expressed as:

$$T_{ge} = \sum_1^3 k_t i_n = \frac{3k_e k_t \omega_{out}}{2(R_{in}+R_{ex})} \qquad \textit{E. 3-4}$$

where k_t is the torque constant of the generator, unit N-m/A. Introducing a linear PTO damping coefficient c_{pto} to represent the damping when the generator is driven by the WEC gives

$$c_{pto} = \frac{T_{ge}\omega_{out}}{x_{in}^2} = \frac{T_{ge}}{\omega_{out}}\frac{4\pi^2}{l_{lead}^2} = \frac{6\pi^2 k_e k_t \omega_{out}}{(R_{in}+R_{ex})l_{lead}^2} \qquad \textit{E. 3-5}$$

When the MMR gearbox is engaged, which is, when either one-way clutch is engaged, the PTO has $\omega_{out} = |\omega_{in}|$. With the input force f_{pto} to the system, the PTO system equation can be written as:

$$m_e\ddot{x}_{in} + c_{pto}\dot{x}_{in} = f_{pto} \qquad \textit{E. 3-6}$$

where m_e is the equivalent inerter due to the generator's and flywheel's rotation inertia [], or called PTO inerter. Specifically, the equivalent inerter of the PTO system can be expressed as:

$$m_e = \left(J_{ge} + J_{fw}\right)\frac{4\pi^2}{l_{lead}^2} \qquad \textit{E. 3-7}$$

Here the term inerter is used instead of inertia because the force is proportional to the relative acceleration $\ddot{x}_{in}$ of the two bodies.

E.3-5 describes the PTO dynamics in the engaged condition when either one of the one-way clutches is engaged, where the generator is driven by the input shaft. In such a case the PTO will couple the input motion with the generator through the ball screw. However, when the output speed of the MMR gearbox exceeds that of the input speed, $\omega_{in} < \omega_{out}$, the overall PTO decouples into two subsystems: one is the ball screw without load driven by the nut, another is the generator rotating under the moment of inertia stored in the inerter. The equation of such disengaged case is then written together as:

$$\begin{cases} f_{pto} = 0 \\ m_e\dot{\omega}_{out} + c_{pto}\omega_{out} = 0 \end{cases} \qquad when \;\; \omega_{in} < \omega_{out} \qquad \textit{E. 3-8}$$

In the disengaged condition, both one-way clutches are disengaged, the MMR gearbox is disconnected from the generator. The energy stored in the inertia of the generator and flywheel will drive the generator until the speed of the input shaft, which is driven by the WEC motion, catches up.

For the non-MMR PTO, however, the ball screw and the generator are always directly connected, so the PTO force can always be described using the PTO equation for the engaged condition.

The simulation results for the MMR PTO compared with the non-MMR linear PTO are illustrated in Figure 3-2. It can be found that when it is disengaged, the generator and the ball screw will be decoupled, and the reactive PTO force become zero as illustrated in the top figure. However, the energy stored in the equivalent mass will continue rotating the generator, keeping the output voltage greater than zero. Combining two figures, the MMR PTO is able to continuously output power when the input force is almost zero, indicating that the MMR PTO has a potential to produce more power output through the disengagement mechanism.

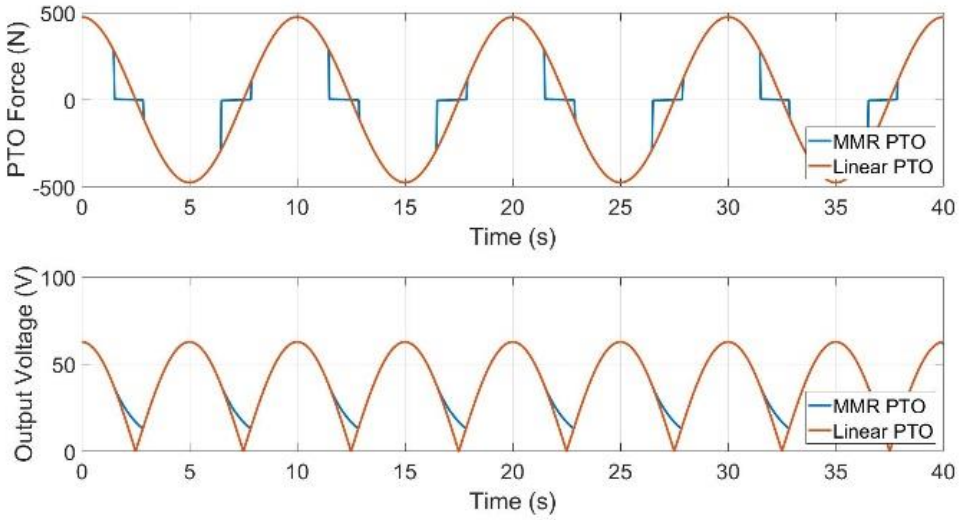

Figure 3-2 Simulation results of the PTO force and output voltage for the MMR PTO in comparison with linear PTO under sinusoid excitation 0.1Hz

From the previous analysis, it can be found that the disengaged time during one period of the operation for the MMR PTO can be influenced by three factors, one is the inertia which decides how much total energy can be stored, one is the damping coefficient of the generator which decides how fast the energy dissipates, the last one is the excitation frequency which decides how fast the speed of disengaged parts can catch up each other. As a result, the disengagement ratio, which represents how much time the MMR PTO is disengaged during one period, can be solved numerically to find out the influence of the three parameters.

From Figure 3-3, it is easy to observe that when the equivalent mass (inertia) of the disengaged part is large, or when the damping coefficient of the generator is small, or when the excitation frequency is high, the disengagement ratio is large, which matches with the intuition. However, further verification on the relationship of these three parameters with the disengagement ratio need to be explored through test. The results of the exploration will be presented in the following chapter.

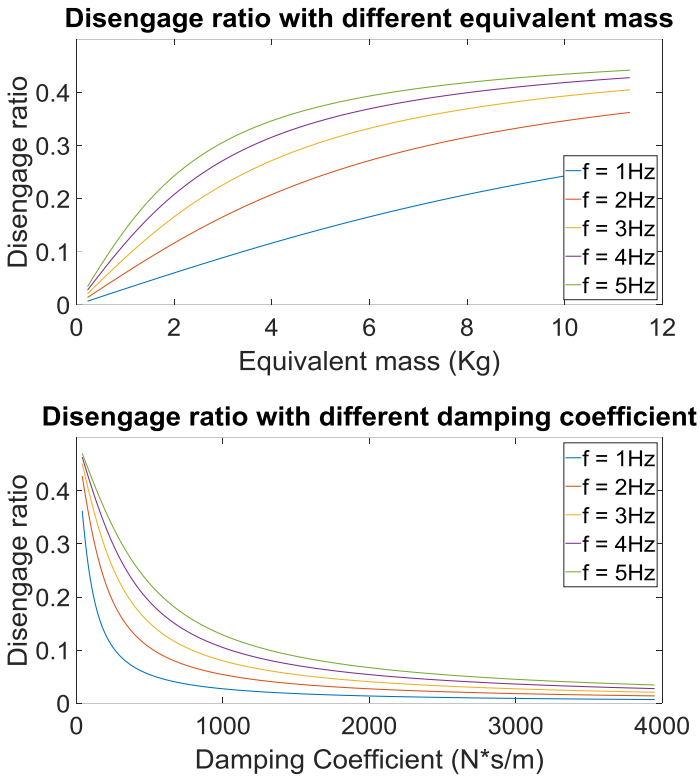

Figure 3-3 Disengage ratio with different equivalent mass and damping coefficient under different excitation frequency

3.3 Modeling of the Self-reactive Point Absorber with MMR PTO

The equations of the proposed WEC in heave can be described as following:

$$\begin{cases} m_1\ddot{x}_1 = f_e^1 + f_r^1 + f_h^1 + f_{pto} + f_d^1 \\ m_2\ddot{x}_2 = f_e^2 + f_r^2 + f_h^2 - f_{pto} + f_d^2 \end{cases} \qquad E.\ 3\text{-}9$$

Here,

- m_1 and m_2 are the physical mass of the floating buoy and the submerged body
- f_e^i are the hydrodynamic excitation force on the buoy and submerged body, (i=1, 2)
- f_r^i are the radiation force on the buoy and submerged body, (i=1, 2)
- f_h^i are the hydrostatic force on the buoy and submerged body, (i=1, 2)
- f_d^i are respectively the drag damping induced force of the floating and submerged body, i=1, 2

The operation condition of the proposed WEC is in moderate sea state. Beatty et al. have experimentally verified that by using the linear wave theory, the wave forces can be acquired accurately except for the viscous and drag damping [62]. According to the linear wave theory, the incident wave induced radiation force can be written in the frequency domain as [56]:

$$\begin{cases} f_r^1 = -A_{11}(\omega)\ddot{x}_1 - A_{12}(\omega)\ddot{x}_2 - c_{11}(\omega)\dot{x}_1 - c_{12}(\omega)\dot{x}_2 \\ f_r^2 = -A_{22}(\omega)\ddot{x}_2 - A_{21}(\omega)\ddot{x}_1 - c_{21}(\omega)\dot{x}_1 - c_{22}(\omega)\dot{x}_2 \end{cases} \quad E.\ 3\text{-}10$$

where,

- ω is the frequency of the excitation wave.
- $A_{11}(\omega)$ and $A_{22}(\omega)$ are the frequency-dependent added mass of the floating buoy and the submerged body.
- $A_{12}(\omega)$ and $A_{21}(\omega)$ are the frequency-dependent added mass of the floating buoy and the submerged body due to the motion coupling with the other body, as the result, these two terms share same value.
- $c_{11}(\omega)$ and $c_{22}(\omega)$ are the frequency-dependent hydrodynamic damping coefficients of the floating buoy and submerged body.
- $c_{12}(\omega)$ and $c_{21}(\omega)$ are the frequency-dependent hydrodynamic damping coefficients of the floating buoy and submerged body due to the motion coupling with the other body, as the result, these two terms share same value.

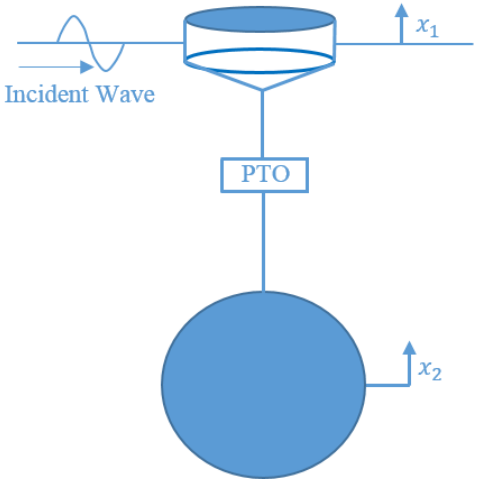

Figure 3-4 Schematic of the proposed self-reactive WEC in heave

The wave forces described above are usually utilized to study the performance of the WEC in frequency domain [63]. However, for the nonlinear system, a time domain approach is commonly used and the radiation force in time domain is usually described by the Cummins equation [64]:

$$\begin{cases} f_r^1 = -A_{11}(\infty)\ddot{x}_1 - A_{12}(\infty)\ddot{x}_2 - \int_{-\infty}^{t} k_{11}(t-\tau)\dot{x}_1(\tau)d\tau - \int_{-\infty}^{t} k_{12}(t-\tau)\dot{x}_2(\tau)d\tau \\ f_r^2 = -A_{22}(\infty)\ddot{x}_2 - A_{21}(\infty)\ddot{x}_1 - \int_{-\infty}^{t} k_{21}(t-\tau)\dot{x}_1(\tau)d\tau - \int_{-\infty}^{t} k_{22}(t-\tau)\dot{x}_2(\tau)d\tau \end{cases} \quad E. 3\text{-}11$$

$$k_{ij}(t) = \frac{2}{\pi}\int_0^{\infty} c_{ij}(\omega)cos\omega t\, d\omega \qquad (i,j = 1,2) \qquad E. 3\text{-}12$$

where,

- $A_{ij}(\infty)$ is the added mass when the frequency approaches to infinity $(i,j = 1,2)$.

The frequency-dependent hydrodynamic parameters in Equations (8) and (9) are acquired by the commercial software WAMIT using Boundary Element Method (BEM) [65]. The meshed plot and results are shown in Figure 3-5 and Figure 3-6, and the dynamic equations are solved numerically.

Here, the PTO force for the MMR PTO applied on the two bodies are presented as following to be in coherence with Equation (5):

$$f_{pto} = \begin{cases} -m_e(\ddot{x}_1 - \ddot{x}_2) - c_{pto}(\dot{x}_1 - \dot{x}_2) & \omega_{out} = |\omega_{in}| \\ 0 & \omega_{out} > \omega_{in} \end{cases} \qquad E. 3\text{-}13$$

where,

- m_e is the inerter from the rotary inertia of the generator and flywheel.
- c_{pto} is the equivalent PTO damping from the generator, which can be calculated with Equation (3).

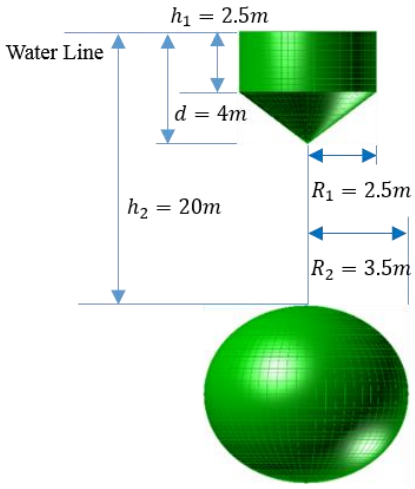

Figure 3-5 The mesh plots for calculating the hydrodynamic parameters using WAMIT

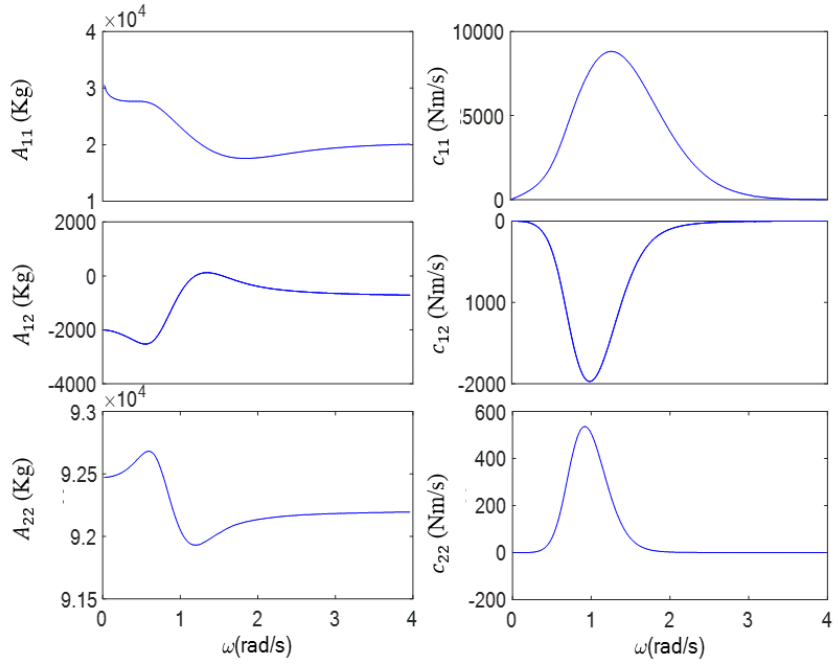

Figure 3-6 The WAMIT calculated hydrodynamic parameters for the self-reactive point absorber

Besides the MMR PTO, the power takeoff force from the non-MMR PTO without using the mechanical motion rectifying mechanism can be shown as:

$$f_{pto} = -m_e(\ddot{x}_1 - \ddot{x}_2) - c_{pto}(\dot{x}_1 - \dot{x}_2)) \qquad E.\ 3\text{-}14$$

The radiation damping calculated from the linear wave theory for a submerged body is usually very small [62]. As a result, the relative motion acquired from the simulation is huge when the wave frequency approaches the natural frequency of the WEC. In reality, however, the existence of the additional nonlinear damping term prevents that from occurring. Experimental results have proven that the real damping is much larger than the results acquired by the WAMIT [65]. This damping term is considered to be the consequence of the drag effect and should be considered in simulation. Generally, the drag damping caused force can be expressed as a quadratic term:

$$\begin{cases} f_d^1 = -\frac{1}{2}\rho c_{d1} A_{c1}(\dot{x}_1 - v_1)|\dot{x}_2 - v_1| \\ f_d^2 = -\frac{1}{2}\rho c_{d2} A_{c2}(\dot{x}_2 - v_2)|\dot{x}_2 - v_2| \end{cases} \qquad \textit{E. 3-15}$$

where,

- ρ is the density of the ocean water.
- c_{d1} and c_{d2} are the drag coefficients for the floating buoy and submerged body, which depends on the geometric shapes of the bodies.
- A_{c1} and A_{c2} are the characteristic areas for the floating buoy and submerged body.
- $\dot{x}_1$ and $\dot{x}_2$ are the velocity for the floating buoy and submerged body.
- v_1 and v_2 are the velocity of the surrounding water for the floating buoy and submerged body.

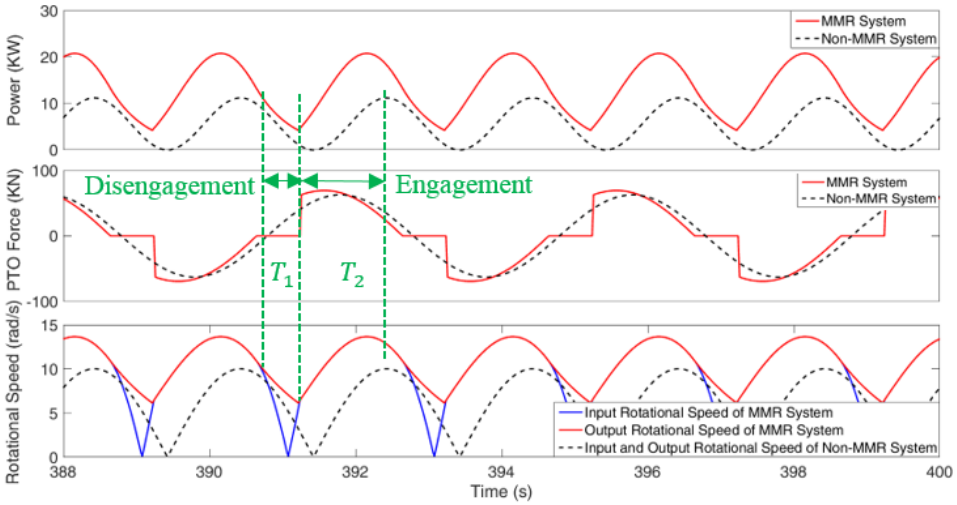

Figure 3-7 Simulation results of the proposed WEC with MMR PTO and Non-MMR PTO under regular wave. Wave period $T = 4s$*, wave height* $H = 2m$*, inerter* $m_e = 10^5 kg$*, equivalent damping* $c_{pto} = 10^5 N * s/m$*, drag coefficient* $c_{d2} = 0.5$.

The analyzed time domain dynamic performance of the point absorber with MMR PTO is then simulated using the WEC-Sim, which is a time domain solver based on MATLAB built by National Renewable Energy Laboratory (NREL) and Sandia National Laboratory of United States [66][67]. Figure.5 illustrates model built into MATLAB Simulink for the WEC-Sim analysis. Since the MMR PTO has a piecewise nonlinear property, a separate block is used for describing the correct dynamic property of MMR PTO when the generator has been coupled/decoupled to the system. In addition to that, all the frequency dependent hydro-parameters has been included in the Simulink model so the real time simulation is reasonable.

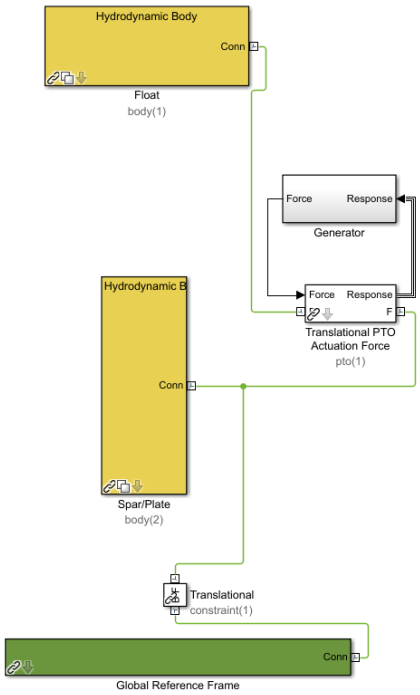

Figure 3-8 The Simulink model used for the WEC-Sim analysis

The choices for the value on the floating buoy from different researchers are not always consistent and it is usually considered to be small, so it is ignored in this paper. In addition, based on the experiment results presented in the work of Zurkinden, et al [68] and Engström et al [69], the drag coefficient of the second body c_{d2} should depend on the shape and surface roughness. As the consequence, a series of different values for the c_{d2} between 0.25 and 2 are selected to study the differences of the system performance as what Babarit, et al has done [70].

The simulation results in time domain for the proposed WEC with MMR system and non-MMR system are illustrated in Figure 3-7. The inerter is exaggerated to be larger than common so disengagement can be observed more clearly, as shown in the figure. Another concept adopted here is to divide one full time period of the MMR WEC into two separated time periods, one is T_1 where the MMR PTO is disengaged, and the other is T_2 where the MMR PTO is engaged. The ratio between the disengaged period T_1 and one full period $(T_1 + T_2)$ is defined as the disengaged ratio. This ratio works as an indicator of the capability of the MMR PTO to stay disengaged. The three major parameters that could

influence the disengage ratio are the inerter of the rotation inertia of flywheel and generation, equivalent PTO damping and the period of the excitation wave, the detailed derivatives can be found in [71]. Figure 3-9 illustrates the disengaged ratio of the proposed MMR PTO under different conditions. When the ratio between the equivalent damping and the inerter is small, the energy stored in the inertia will dissipate slower, thus a higher disengage ratio is acquired. In addition, when the wave period is smaller, the disengage ratio will also be higher as the energy dissipate speed is constant, thus the smaller wave period lead to a larger disengage ratio.

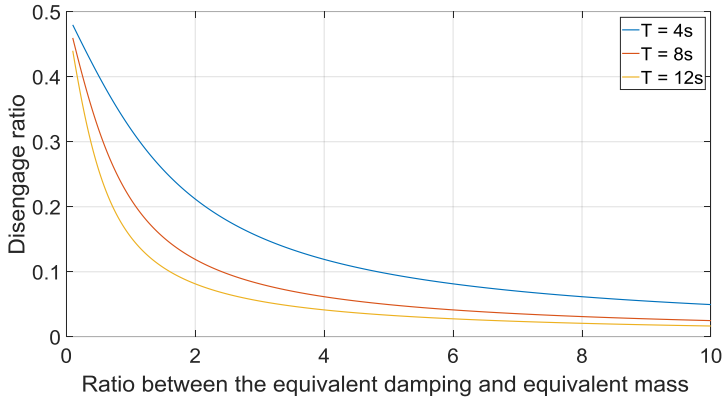

Figure 3-9 Disengage ratio of the MMR PTO under different wave conditions. Results in the Figure use wave height $H = 2m$*, inerter* $m_e = 10^5 kg$*, equivalent damping* $c_{pto} = 10^5 N * s/m$*, drag coefficient* $c_{d2} = 0.5$.

3.4 Optimization of Power Absorption

With the dynamic properties of the PTO and the WEC explored in the previous sections, optimization for the proposed PTOs is necessary for maximum power absorption.

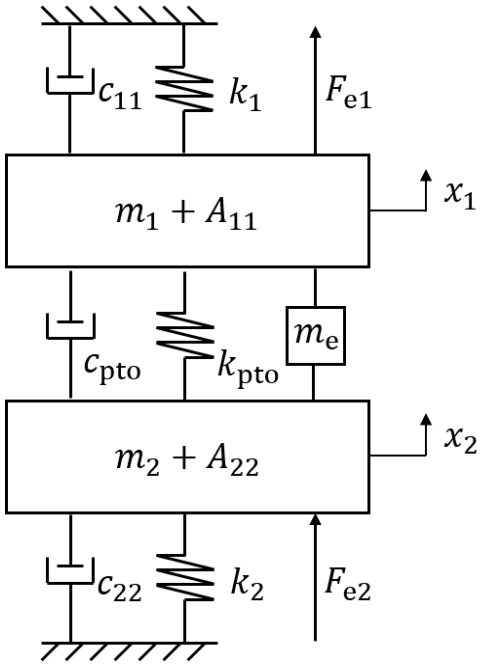

Figure 3-10 Free body diagram of the self-reactive point absorber with PTO inertia cosidered

Figure 3-10 illustrates the scheme of the designed WEC, the model is simplified by neglecting multiple factors including the phase difference of the excitation force and the hydro parameters generated from the interference between the two bodies, the reason is that these terms are usually small and the error caused by neglecting such terms is acceptable [30]. The results obtained from the simplified model serve as the starting point of the optimization to improve the optimization efficiency. The objective function of the optimization can be presented as:

$$Maximize\ P_{pto} = c_{pto}(\dot{x}_1 - \dot{x}_2)^2 \qquad E.\ 3\text{-}16$$

Here, the WEC is assumed to be under excitation of sinusoid wave input, so by maximizing the PTO power P_{pto}, the total energy absorption can reach its maximum as well. Combining the dynamic modeling of the PTO and WEC together. The equations of motion of the proposed WEC oscillating in heave can be derived through the scheme as:

$$\begin{cases}(m_1 + A_{11})\ddot{x}_1 + m_{pto}(\ddot{x}_1 - \ddot{x}_2) + c_{11}\dot{x}_1 + c_{pto}(\dot{x}_1 - \dot{x}_2) + k_1 x_1 + k_{pto}(x_1 - x_2) = F_{e1} \\ (m_2 + A_{22})\ddot{x}_2 + m_{pto}(\ddot{x}_2 - \ddot{x}_1) + c_{22}\dot{x}_2 + c_{pto}(\dot{x}_2 - \dot{x}_1) + k_2 x_2 + k_{pto}(x_2 - x_1) = F_{e2}\end{cases}$$

E. 3-17

Here, the E. 3-17 can only be used for describing the WEC with non-MMR PTO, because the equation describes a linear system. The system equation is then written in frequency domain to solve a close form solution, when the WEC is excited under regular wave. The system is rewritten with the assumption that $F_{e1} = F_1 e^{i\omega t}$, $F_{e2} = F_2 e^{i\omega t}$, $x_1 = X_1 e^{i\omega t}, x_2 = X_2 e^{i\omega t}$, and then it is described as,

$$-\omega^2 AX + i\omega CX + KX = F \qquad \textit{E. 3-18}$$

where,

$$A = \begin{bmatrix} m_1 + A_{11} + m_e & -m_e \\ -m_e & m_2 + A_{22} + m_e \end{bmatrix} \qquad \textit{E. 3-19}$$

$$C = \begin{bmatrix} c_{11} + c_{pto} & -c_{pto} \\ -c_{pto} & c_{22} + c_{pto} \end{bmatrix} \qquad \textit{E. 3-20}$$

$$K = \begin{bmatrix} k_1 + k_{pto} & -k_{pto} \\ -k_{pto} & k_2 + k_{pto} \end{bmatrix} \qquad \textit{E. 3-21}$$

$$X = \begin{bmatrix} X_1 \\ X_2 \end{bmatrix}, F = \begin{bmatrix} F_{e1} \\ F_{e2} \end{bmatrix} \qquad \textit{E. 3-22}$$

Rewritten the equation in the form of solution,

$$X = (-\omega^2 A + i\omega C + K)^{-1} F \qquad \textit{E. 3-23}$$

Define:

$$Z(i\omega) = -\omega^2 A + i\omega C + K = \begin{bmatrix} Z_{11} & Z_{12} \\ Z_{21} & Z_{22} \end{bmatrix} \qquad \textit{E. 3-24}$$

And the expanded form is:

$$\begin{cases} Z_{11} = -\omega^2(m_1 + A_{11} + m_e) + i\omega\left(c_{11} + c_{pto}\right) + k_1 + k_{pto} \\ Z_{12} = \omega^2 m_e - i\omega c_{pto} - k_{pto} \\ Z_{21} = \omega^2 m_e - i\omega c_{pto} - k_{pto} \\ Z_{22} = -\omega^2(m_2 + A_{22} + m_e) + i\omega\left(c_{22} + c_{pto}\right) + k_2 + k_{pto} \end{cases} \quad \textit{E. 3-25}$$

The solution can be written as:

$$X_1 = \frac{Z_{22}F_1 - Z_{21}F_2}{det(Z)}, X_2 = \frac{Z_{11}F_2 - Z_{12}F_1}{det(Z)} \quad \textit{E. 3-26}$$

Knowing the solution for the equations of the system, in the frequency domain, the power absorbed can be expressed as:

$$P_{pto} = \frac{1}{2}\omega^2 c_{pto}|X_1 - X_2|^2 \quad \textit{E. 3-27}$$

By expanding which, the equation can be rewritten as:

$$P_{pto} = \frac{1}{2}\omega^2 c_{pto}\left|\frac{p+iq}{(a+ib)m_e+(c+id)c_{pto}+(e+if)k_{pto}+g+ih}\right|^2 \quad \textit{E. 3-28}$$

where:

$$\begin{cases} p = k_2F_1 - k_1F_2 - \omega^2(m_2 + A_{22})F_1 + \omega^2(m_1 + A_{11})F_2 \\ q = \omega c_{22}F_1 - \omega c_{11}F_2 \\ a = \omega^4(m_1 + m_2 + A_{11} + A_{22}) - \omega^2(k_1 + k_2) \\ b = -\omega^3(c_{11} + c_{22}) \\ c = \frac{b}{\omega}, d = -\frac{a}{\omega}, e = -\frac{a}{\omega^2}, f = -\frac{b}{\omega^2} \\ g = \omega^4(m_1 + A_{11})(m_2 + A_{22}) - \omega^2((m_1 + A_{11})k_2 + (m_2 + A_{22})k_1 + c_{11}c_{22}) + k_1k_2 \\ h = -\omega^3((m_2 + A_{22})c_{11} + (m_1 + A_{11})c_{22}) + \omega(k_2c_{11} + k_1c_{22}) \end{cases} \quad \textit{E. 3-29}$$

Since the studied PTO is a rigid system with solid connection, the stiffness of the PTO k_{pto} is chosen to be zero constantly. Since the mass ratio between the two bodies can also influence the power absorption, it is set as constant that the mass of the submerged body is 10 times of the floating buoy here.

By taking the partial derivative of the c_{pto} and m_e for the E.3-28:

$$\frac{\partial P_{pto}}{\partial m_e} = \frac{\omega^2 c_{pto}(p^2+q^2)\left((a^2+b^2)m_e+(ac+bd)c_{pto}+(ag+bh)\right)}{\left((am_e+cc_{pto}+g)^2+(bm_e+dc_{pto}+h)^2\right)^2} \quad \textit{E. 3-30}$$

$$\frac{\partial P_{pto}}{\partial c_{pto}} = \frac{0.5\omega^2(p^2+q^2)((bm_e+h)^2+(am_e+g)^2-(c^2+d^2)c_{pto}^2)}{\left((am_e+cc_{pto}+g)^2+(bm_e+dc_{pto}+h)^2\right)^2} \quad \textit{E. 3-31}$$

It is certain that $p^2 + q^2 \geq 0$. The minimum can be acquired when the two partial derivatives are zero:

$$(a^2 + b^2)m_e + (ac + bd)c_{pto} + (ag + bh) = 0 \quad \textit{E. 3-32}$$

$$(bm_e + h)^2 + (am_e + g)^2 - (c^2 + d^2)c_{pto}^2 = 0 \quad \textit{E. 3-33}$$

From the equation (29), it is easy to acquire an addition condition that:

$$ac + bd = 0 \quad \textit{E. 3-34}$$

Bring in E.3-34 and solve E.3-32 and E.3-33 can obtain the optimal inerter of the PTO rotation inertia and the optimal PTO damping:

$$m_{e\_opt} = -\frac{ag+bh}{a^2+b^2} \quad \textit{E. 3-35}$$

$$c_{pto\_opt} = \sqrt{\frac{(a^2+b^2)m_e^2+(h^2+g^2)+2(ag+bh)m_e}{c^2+d^2}} \quad \textit{E. 3-36}$$

The c_{pto_opt} can be simplified by using the condition that$(a^2 + b^2) = (c^2 + d^2)\omega^2$, the equation become:

$$c_{pto\_opt} = \frac{|ah-bg|}{\omega(c^2+d^2)} \quad \textit{E. 3-37}$$

Through the previous equations, the frequency domain optimized inerter and equivalent damping c_{pto_opt} and m_{e_opt} can be acquired. Knowing the c_{pto_opt} and m_{e_opt}, the monotonic property is checked for the derived equations that the results obtained is the optimum condition instead of a saddle point, and the optimum condition for the inerter and damping coefficient of the non-MMR PTO is obtained. The results acquired from the closed-form solution for simplified system can be used as initial guess for the numerical optimization process and give great improvement on the compute efficiency. If a drag

damping term is linearized for simplification, the solution can give good prediction. However, in this paper, the author choose to use the numerical approach for better accuracy.

For WEC with MMR based PTO, however, due to its nonlinearity, there is no closed-form solution for the optimal inerter and the optimal damping. The modified constrained complex method is adopted to find the optimum condition for the MMR based WEC (and for non-MMR PTO also) [72][73].

Using the same WEC with MMR PTO, different choice on the PTO parameters, mainly on the damping coefficient and equivalent inertia, can lead to different power absorption results. Moreover, the optimum damping coefficient is different under various dominant wave periods. As a result, if the optimum damping coefficient used in the prototype changes as the wave condition changes, the power absorption will significantly increase and further benefit the overall power absorption.

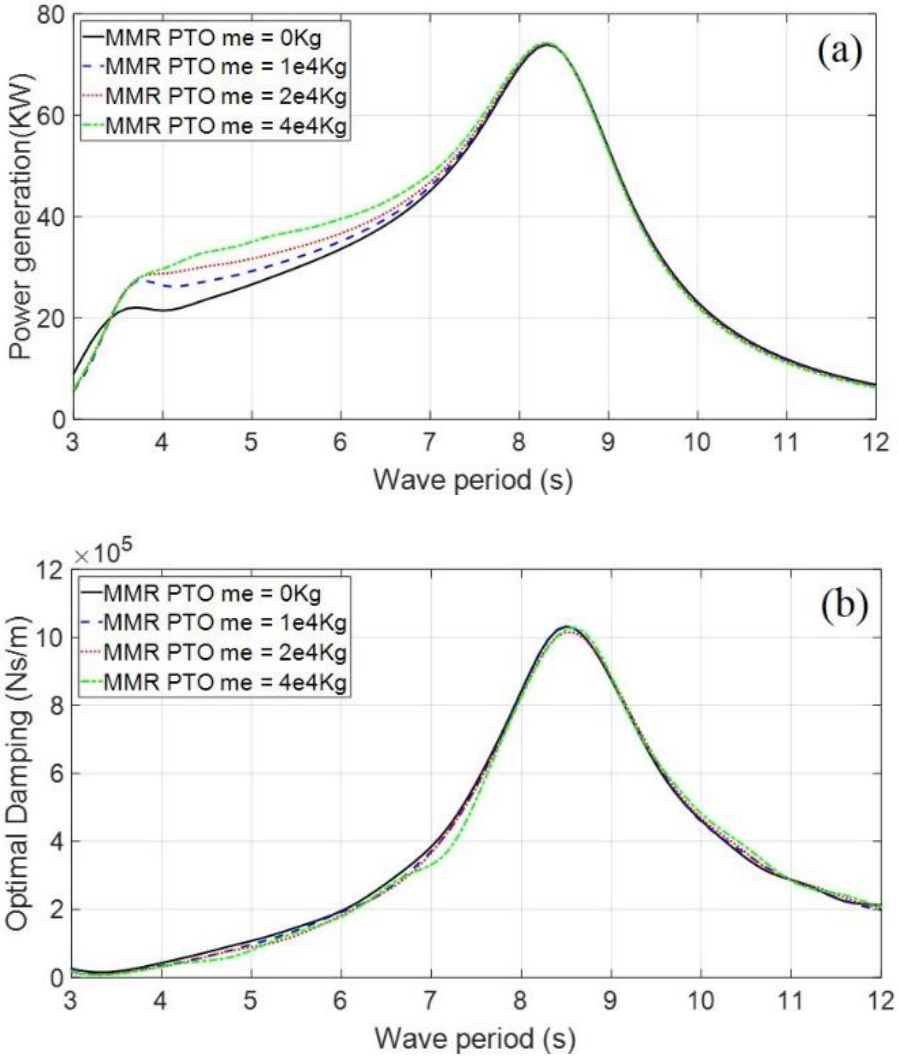

Figure 3-11 (a) Optimum power of the MMR system (b) Optimum PTO damping coefficient of MMR system with various designs of inerter under regular wave excitation. For the results shown in this Figure , wave height $H = 2m$, the drag coefficients $c_{d1} = 0.25$, $c_{d2} = 0.5$.

In the real design process, the damping coefficient can be changed conveniently by adjusting the duty-cycle of the DC/DC electric converter connected with the generator. The equivalent inerter, however, is usually constant and difficult to be tuned. In order to give practical guidance to the design of the WEC, different equivalent inerter are adopted and are regarded as constant once chosen. The equivalent damping coefficient, on the contrary, is set to be the variable that need to be optimized. Figure 3-11(a) shows the optimal power

of a two-body self-reacting WEC with MMR PTO under regular wave excitation. The corresponding optimal equivalent damping coefficient is plotted in Figure 3-11(b). It is easy to observe that there are two peaks for the optimal output power. One is around 4s, which is close to the natural frequency of the floating buoy ($\omega_1 = \sqrt{\frac{k_1}{m_1+A_{11}}} = 1.57 rad/s$, and the corresponding period is $T_1 = \frac{1}{\omega_1} = 4s.$). Therefore, the motion of the floating buoy is very large around 4s. The other peak power happens around 8s, which is the damped natural frequency of the two-body system. The corresponding optimal damping is maximum in Figure 3-11(b). When the inerter increases from 0 to $4 * 10^4 kg$, the optimal power between the two peaks increases as well. The disengagement ratio also increases with the increase of inerter. At large excitation wave periods, the optimum equivalent damping is large. According to the results illustrated in Figure 7, the large equivalent damping will lead to a small disengage ratio, which makes the system close to a non-MMR system. As the consequence, the optimal power around 8s does not change with different inerter.

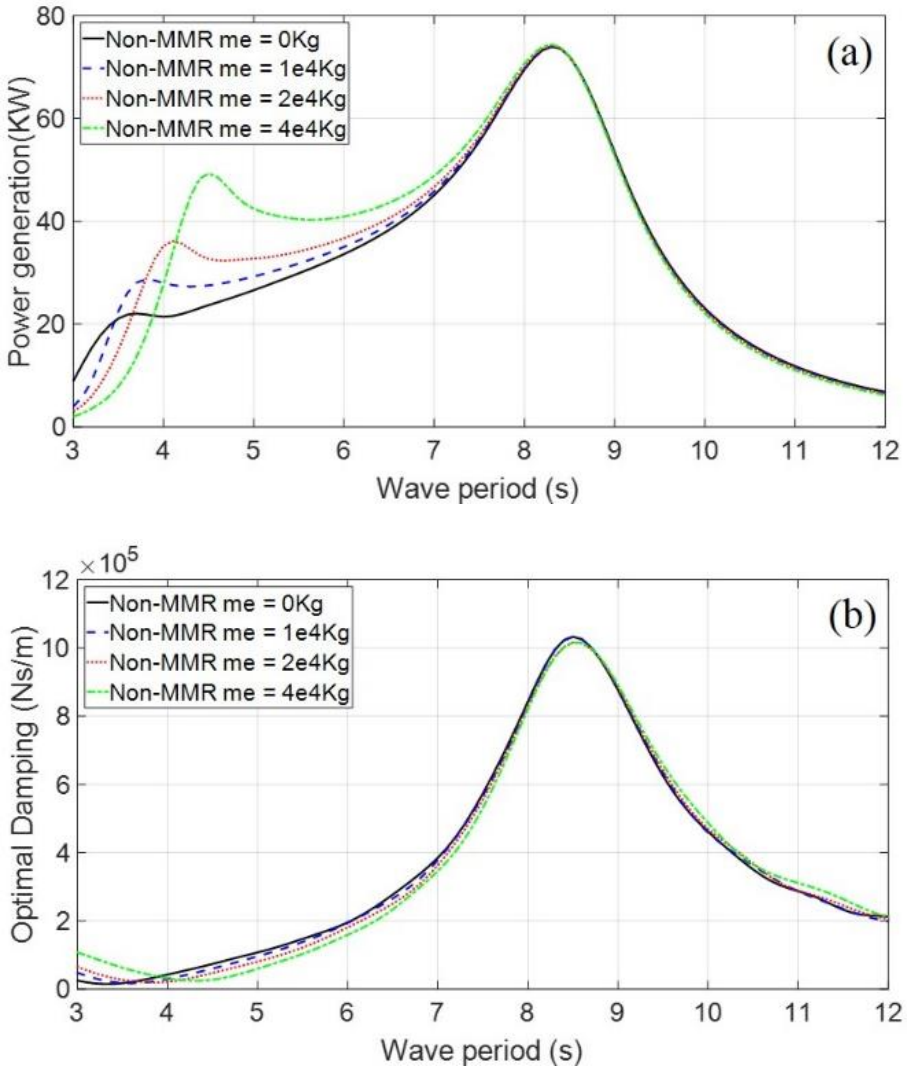

Figure 3-12 (a) Optimum power of the non-MMR system, (b) Optimum PTO damping coefficient of non-MMR system with various selection of inerter under regular wave excitation. For the results shown in this Figure , wave height $H = 2m$, the drag coefficients $c_{d1} = 0.25$, $c_{d2} = 0.5$.

Figure 3-12(a) shows the optimal power of WEC with non-MMR PTO under regular wave excitation. The corresponding optimal power takeoff damping is plotted in Figure 3-12(b). It is easy to observe that the effect of inerter in a non-MMR system is different from what is shown in the MMR system. The inerter appeared in the power takeoff force in Equation (15) is related with the relative acceleration of the floating buoy and submerged body. As a result, it acts as an inerter. Therefore, different selection of inerter in a non-MMR system

change the mass of the WEC and therefore influence the peak and period of the response. In Figure 3-12(a), when the inerter increases from 0 to $4 * 10^4 kg$, the optimal wave period corresponding to left peak power increases. At the same time, the left peak power increases as well. However, the power decreases fast when the excitation wave period is smaller than the left peak period at low excitation wave period. On the other hand, for a MMR system, due the disengagement mechanism, the peak power on the left does change much for various inerter.

For the influence of the inerter on MMR and non-MMR PTO. From Figure 3-11 and Figure 3-12, due to the disengagement mechanism of MMR system, the PTO inerter helps to increase the power absorption at small wave periods. The peak period of MMR system is not sensitive to the variation of inerter. For a non-MMR system, however, different inerter will lead to a different period where first peak shows up, the maximum power can be changed as well. Therefore, when the inerter increases, the absorption power decreases dramatically when the excitation wave period is far always for the peak period in non-MMR system.

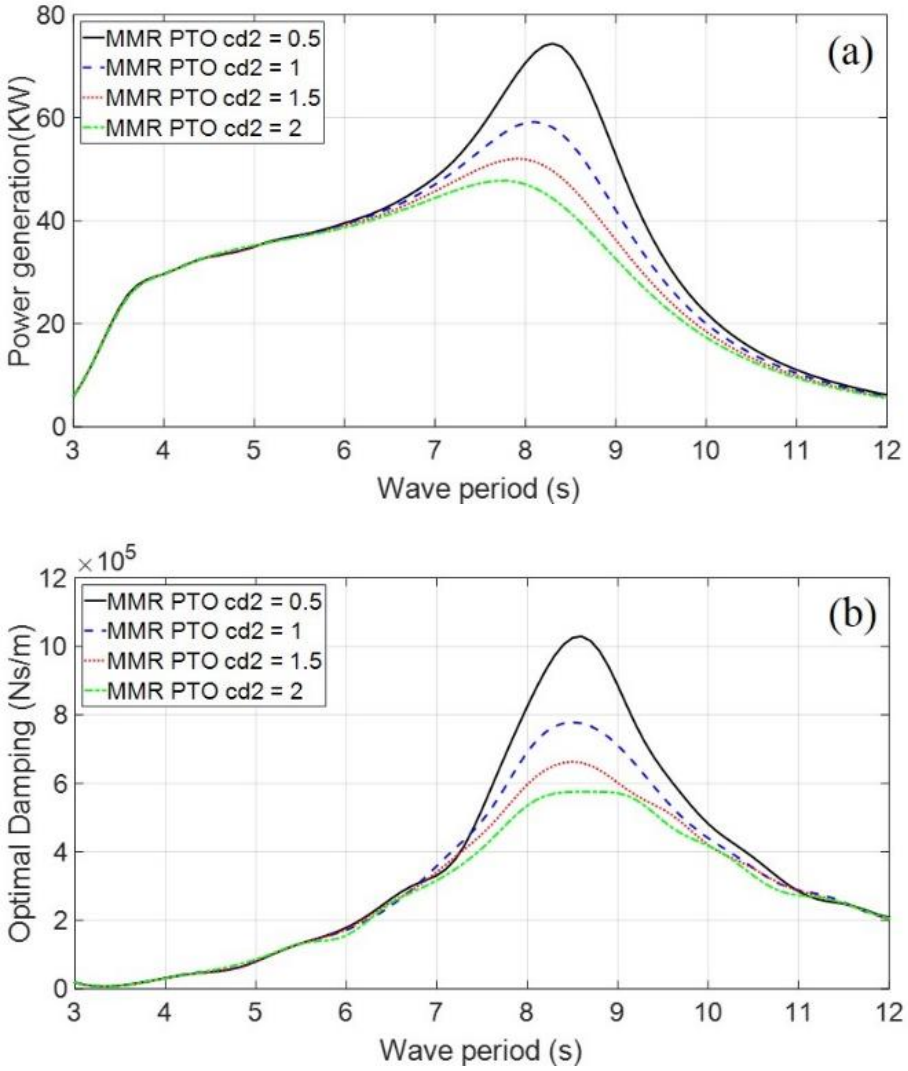

Figure 3-13 (a) Optimum power of the MMR system (b) Optimum PTO damping coefficient of MMR system with various selection of drag coefficient c_{d2} under regular wave excitation. For the results shown in this Figure, wave height $H = 2m$; inerter $m_e = 4 * 10^4 kg$; the drag coefficients $c_{d1} = 0.25$.

In addition to the inerter, another factor that could significantly influence the power absorption is the drag damping coefficient. As described in the previous section, it is difficult to determine the drag coefficient accurately in reality. However, the influence of the drag coefficient can still be explored by selecting various drag coefficient c_{d2} and investigate the effect on the power absorption. Figure 3-13 and Figure 3-14 shows the optimal power and corresponding equivalent damping of MMR and non-MMR PTO under

various drag coefficients c_{d2}. With the increase of drag damping c_{d2}, the optimal power and corresponding damping for the first peak have little change. This is due to the first peak is induced by the floating buoy, so the results will not change much since the property of the floating buoy doesn't change. The optimal power absorption from the second peak, on the contrary, is affected significantly by the drag coefficient, indicating that the motion of the second body is large, thus the drag damping could has greater effect.

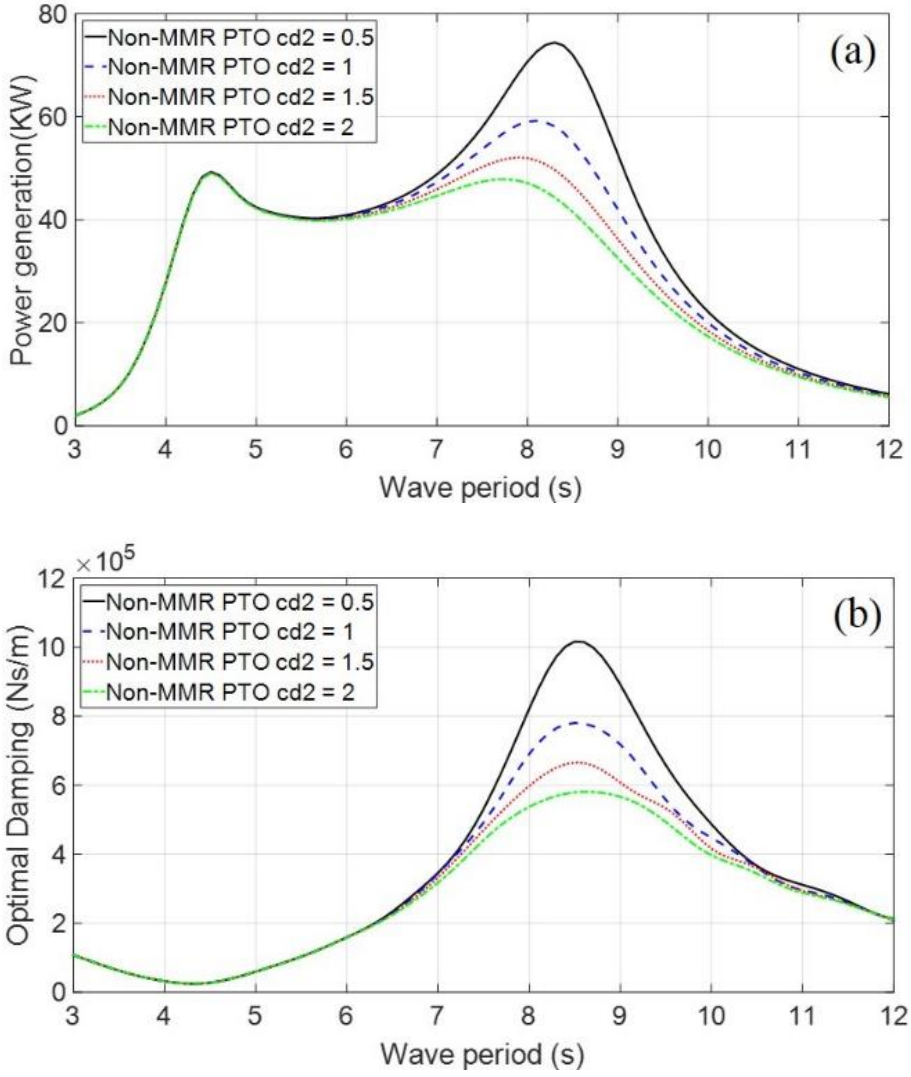

Figure 3-14 (a) Optimum power of the non-MMR system (b) Optimum PTO damping coefficient of the non-MMR system with various selection of drag coefficient c_{d2} under regular wave excitation. For the results shown in this Figure, wave height $H = 2m$; inerter $m_e = 4 * 10^4 kg$; the drag coefficients $c_{d1} = 0.25$.

Previous results are all acquired based on the regular wave, yet the more meaningful results are the power absorption under the irregular wave. To further explore the optimum power absorption of the proposed WEC, the irregular wave condition are used for optimization. The irregular waves is approximated with the superposition of regular waves with wave spectrum. A Pierson-Moskowitz spectra shown in Equation (38), which is an empirical equation that defines the distribution of energy with wave frequency in the fully developed sea, is used here to describe the irregular wave spectra [74][75].

$$S(\omega) = 263 H_s^2 T_e^{-4} \omega^{-5} exp(-1054 T_e^{-4} \omega^{-4}) \qquad E.\ 3\text{-}38$$

where,

- H_s is the significant wave height.
- T_e is the energy period.
- ω is the wave frequency.

For time domain simulation, the irregular wave force is approximated with the sum of *N* components, as shown in the following equation,

$$f_{ei}(t) = \sum_{i=1}^{n} f_{ei}(\omega_i)\, A_{\omega_i} cos(\omega_i t + \alpha_i + \psi_i(\omega_i)\ ) \qquad E.\ 3\text{-}39$$

where,

- $f_{ei}(\omega_i)$ is the excitation force at ω_i under regular excitation.
- $A_{\omega_i} = \sqrt{2S(\omega_i)\Delta\omega}$ is the amplitude of wave component at ω_i. $S(\omega_i)$ is the spectra component at ω_i. $\Delta\omega$ is the frequency step length, which is 0.01rad/s in this paper.
- ω_i is the frequency component
- ψ_i is the phase of excitation force $f_{ei}(\omega_i)$ at ω_i under regular excitation.
- α_i is a random phase in the interval $[0, 2\pi]$.

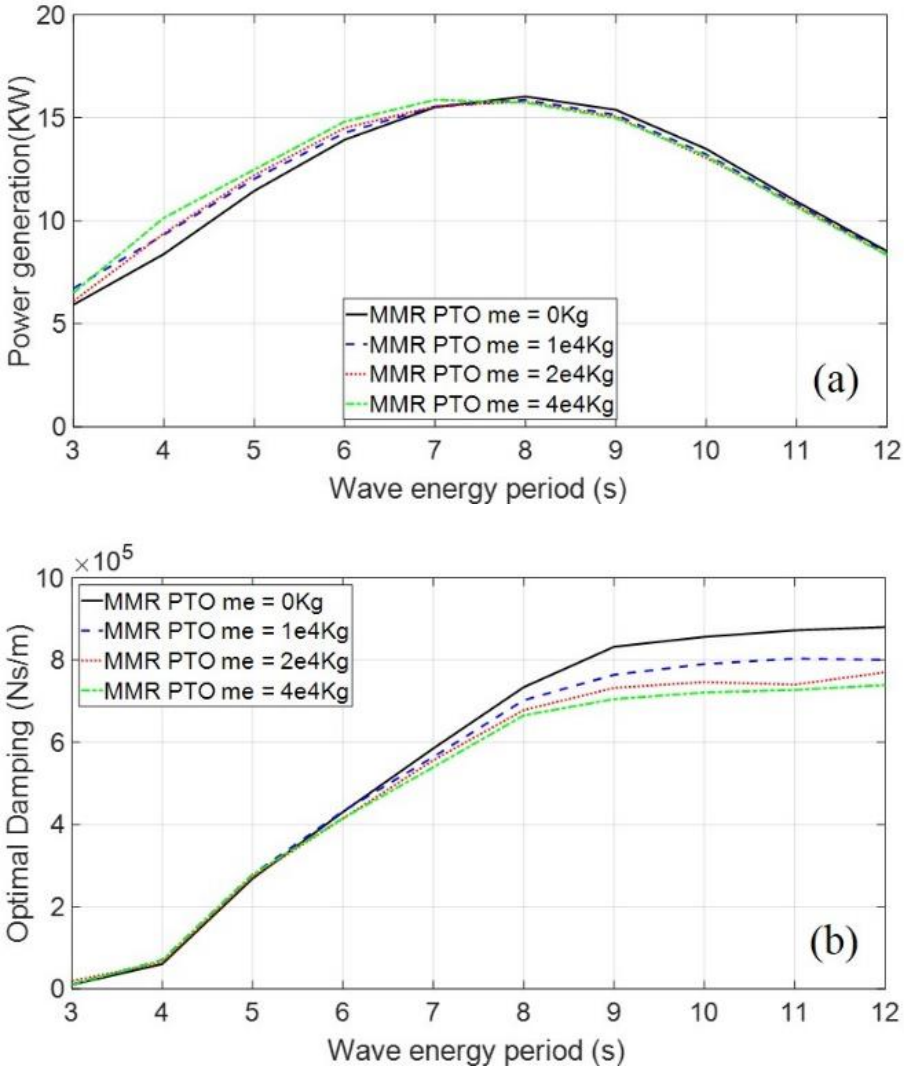

Figure 3-15 (a) Optimum power of the MMR system (b) Optimum PTO damping coefficient of MMR system with various selection of inerter m_e under irregular wave excitation. For the results shown in this Figure, significant wave height $H_s = 2m$; the drag coefficients $c_{d1} = 0.25$, $c_{d2} = 0.5$.

Figure 3-15 shows the optimal power and damping coefficient of the WEC with MMR PTO in irregular waves with different dominant wave energy period. Due to the nonlinearity brought from the random phase used in the simulation, the results are not smooth curve. However, similar trend with the regular wave results can be found. At the first peak where the floating buoy matches the dominant energy period, the optimal damping coefficient is small and the larger inerter can benefit the system with larger

disengage ratio. As the result, the MMR system with larger inerter can have better energy absorption performance. Since the irregular wave can be regarded as a superposition of a series of regular waves, it will weaken the difference brought by the different inerter as shown in Figure 3-15, the optimal power is close with different inerter.

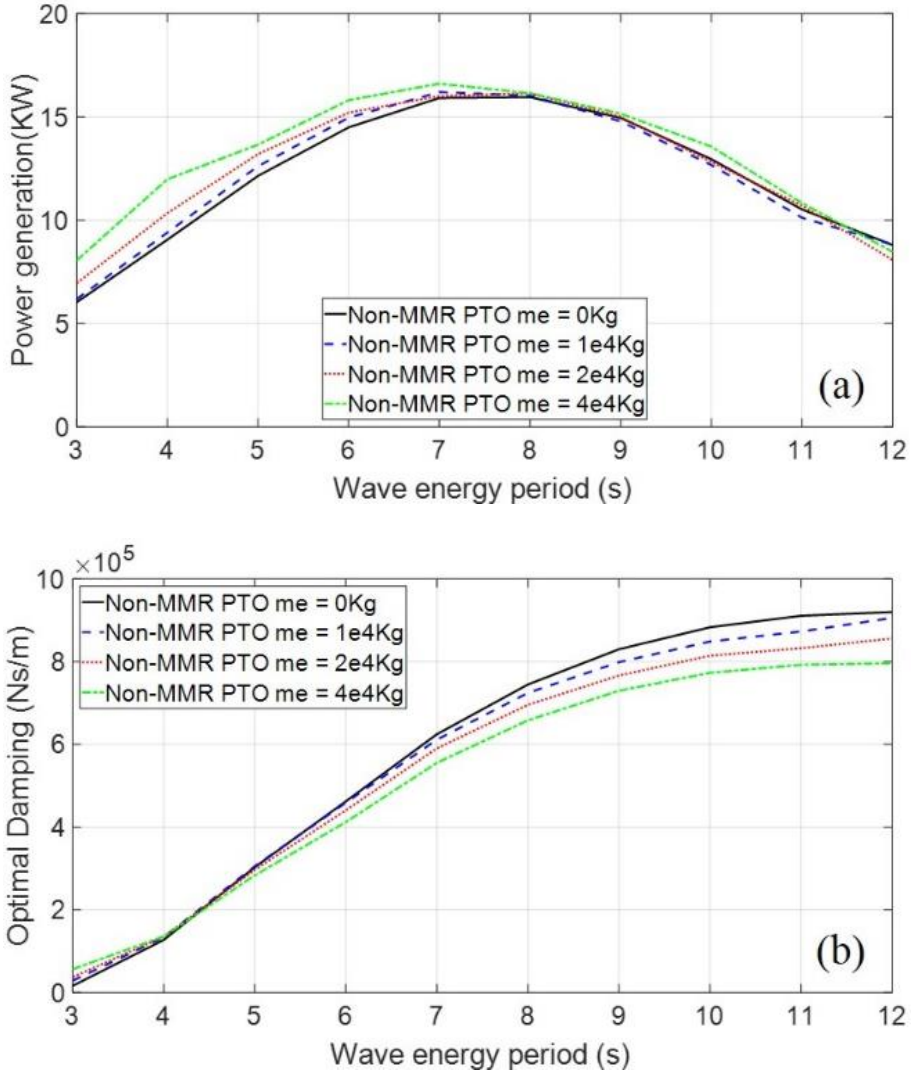

Figure 3-16 (a) Optimum power of the non-MMR system (b) Optimum PTO damping coefficient of the non-MMR system with various selection of inerter m_e under regular wave excitation. For the results shown in this Figure, significant wave height $H_s = 2m$; the drag coefficients $c_{d1} = 0.25$, $c_{d2} = 0.5$.

Figure 3-16 illustrates the optimal power and damping coefficient under irregular wave of the WEC with non-MMR PTO. For the non-MMR system, the inerter is directly connected

with the floating buoy and can change the resonant frequency of the floating buoy. As the result, the optimal power can be absorption near the first peak is different for the WEC with different inerter. It should be noted that although the optimal power near the first peak is different for both the MMR and non-MMR PTO, the principle behind the scene is different. The MMR system is resulted from the different disengage ratio and the non-MMR system is resulted from the change of the resonant frequency of the floating buoy.

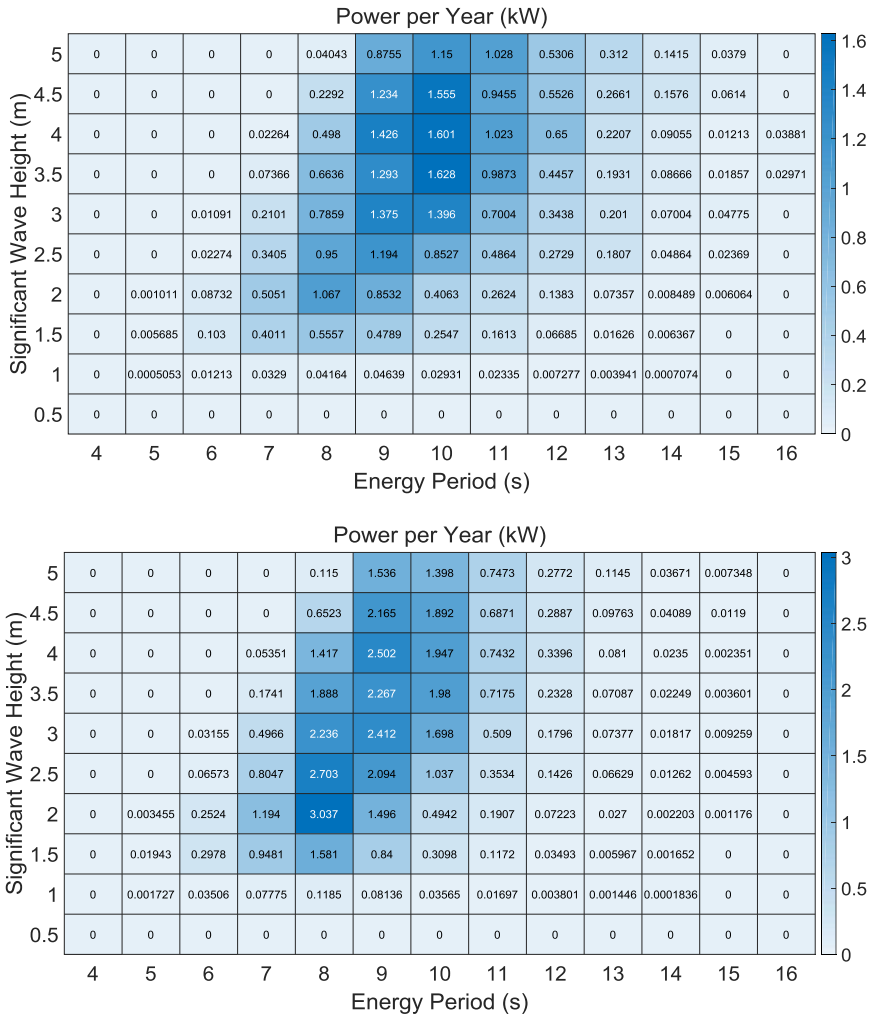

Figure 3-17 (Top) Power heat map for the WEC with constant damping coefficient; (Bottom) Power heat map for the WEC with optimized damping coefficient

To verify the difference between using the optimized damping and a constant damping coefficient, simulation has been conducted using the wave conditions at the Pacific Marine Energy Center - South Energy Test Site (PMEC-SETS) [76]. The prototype scale used in

the simulation is the same with the one used in the previous figure, that the WEC has a 5m diameter buoy floating on the ocean surface.

Figure 3-17 shows the comparison of the power generation between the WEC with constant damping coefficient and optimized damping coefficient. By using the optimized damping coefficient for each wave condition, the yearly power acquired can be significantly improved. Using the wave condition for the PMEC-SETS, the yearly power generation with all the wave conditions considered can be improved by over 43%.

3.5 Chapter Summary

In this chapter, the dynamic modeling for the MMR PTO and the self-reactive point absorber is established. Through modeling and simulation, the unique dynamic property of engagement and disengagement for the MMR PTO is observed. It is noticed that this unique phenomenon can contribute to better energy harvesting effect of the PTO. The three major parameters that can influence the disengagement ratio of the MMR PTO, which are the inertia, the damping coefficient and the excitation frequency, is found.

A numerical optimization approach is used to optimize the power absorption for both the MMR and non-MMR PTO. It is found that due to the mechanism of engagement and disengagement, when the wave period is small and close to the natural frequency of the floating buoy, the increase of the inerter in the MMR PTO can help the WEC to stabilize the optimum power generation. For the non-MMR system, however, the increase of the inerter will change the mass property of the system and mitigate the frequency where the first peak happens to a larger wave period; the peak power will be larger yet decrease much faster. At large wave periods, the MMR PTO have similar performance with the non-MMR PTO. The dominant factor is the self-reactive structure design. In conclusion, in real ocean situations, the MMR PTO is more preferable as the performance is more stable with a wider bandwidth.

In addition, the influence of the drag damping is investigated. Since the first body is floating on the ocean surface, the major variance is the drag coefficient on the second body. It can be concluded that the drag damping generally will have a negative effect for the energy absorption, especially when the WEC reaches its natural frequency. Generally, the

design of the reactive body should take in consideration of the drag effect and minimize the drag damping coefficient to improve the performance of the WEC.

4. Dry lab test of the MMR PTO

4.1 Chapter Introduction

In this section, the prototyped MMR PTO is tested on a test bench in the dry lab environment to verify the simulated results. Through the test, the dynamic model is revised and refined for more accurate prediction on the performance of the proposed. In addition, the parameter choices, such as damping coefficient, inertia of the PTO and the excitation frequency of the MMR PTO, are explored and concluded through the test. The test results show that the MMR can achieve high improvement compared with the non-MMR PTO, confirming the analyzed results in the previous sections. At last, a 10kW large scale prototype is sent to the National Renewable Energy Laboratory (NREL) to conduct break down test and find the weak parts in the design.

4.2 Dynamic Performance Verification on 50W Prototype

4.2.1 Test set-up

The first prototype which is the smallest rated at 50W was tested firstly as the proof of concept. Figure 4-1 illustrates the test set-up for the 50W prototype.

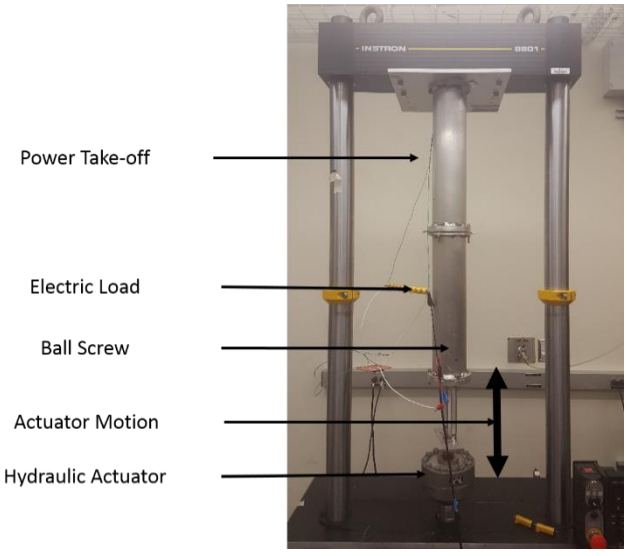

Figure 4-1 50W MMR PTO prototype test set-up

The prototype is assembled inside an aluminum cylinder and mounted upside down on a plate that is locked on the top of the test machine. The push rod of the PTO is actuated by

the hydraulic actuator at the bottom of the test machine. The actuator provides a linear excitation to the PTO. The sensor embedded in the test machine measures the input force and displacement to the PTO. And the voltage output of the generator is measured on the electric load connected to the generator. All the signals are recorded by the DAQ system of the Instron machine.

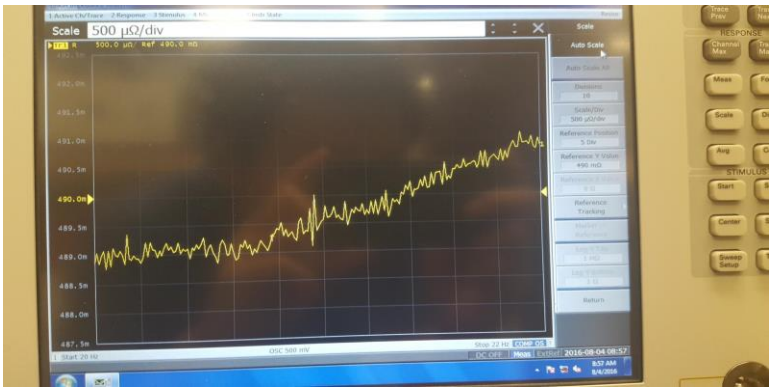

Figure 4-2 Impedance analyzer reading of the inner resistance of the generator

Table 1 Parameters for the components used in the 50W prototype

Value	Component parameter
$0.242\ (Nm/A)$	torque constant of the generator
$40(rpm\ /\ V)$	electric constant of the generator
$4.2\ ohm$	inner resistance of the generator
--	outer resistance of the generator
$1.36\ Kg$	mass of the push rod
$1.21\ Kg$	mass of the ball screw nut
$4.95 \times 10^{-5}\ Kg \cdot m^2$	moment of inertia of the ball screw
$1.74 \times 10^{-5}\ Kg \cdot m^2$	moment of inertia of the coupling
$2.01 \times 10^{-5}\ Kg \cdot m^2$	moment of inertia of the MMR gearbox
$5.40 \times 10^{-5}\ Kg \cdot m^2$	moment of inertia of the generator

By using an impedance analyzer as illustrated in Figure 4-2, the inner resistance and inner inductance of the generator is measured. Because the impedance of the inductor jωL is

much smaller than the inner resistance at low frequency, the output voltage of the generator can be calculated using the measured voltage on the electric load. Unlike to other prototypes that used 3 phase AC generator, the 50W scale prototype used a DC generator, hence the output voltage during the test is always positive. Table 1 listed all the parameters used in the 50W PTO, different outer resistors with various resistance are used during the test to create different damping coefficient of the generator.

4.2.2 Test result analysis

The time-domain test results of the MMR PTO are illustrated in Figure 4-3. The test is conducted with a relatively large outer resistor that can give the system small electrical damping to create a more obvious MMR effect. The test machine is actuated at the frequency 3Hz with a sinusoidal displacement of 8mm, which makes the total stroke 16mm. Based on the recorded forces in Figure 4-3, disengagement happens when the absolute value of the force is around 100N. The constant force of the system should come from the dynamic friction of the system. Whenever the movement of the system changes the direction, the friction force also changes direction. The raised parts of the force figure primarily come from the equivalent mass considering the small electric damping used in the test. When the MMR gearbox reengages from the disengagement, the equivalent mass of the generator will be dragged to accelerate, which will cause the force to raise; when the system is disengaged again, the force from the mass will become zero and the force will be pure friction again.

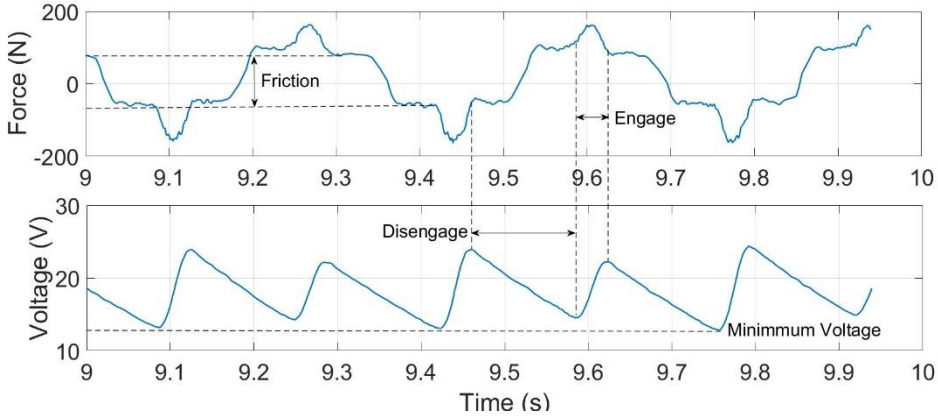

Figure 4-3 Input force and output voltage of the 50W MMR PTO in dry lab test

In addition to the force results, the voltage results also show the obvious phenomenon of the MMR effect. The output voltage on the outer resistor is always larger than zero. Thus, when disengagement happens the MMR PTO will keep outputting power non-stop for better energy harvesting performance.

4.2.3 Dynamic model refinement

Although the engagement and disengagement phenomena are captured well in Figure 4-3 based on the test results, an obvious discrepancy between the modeling and simulation results can be observed. To better characterize the MMR PTO and make the simulation match better, a classic friction model based on Armstrong [77][78] is considered as,

$$F_f = \sqrt{2exp}(F_{brk} - F_C) * exp\left(-\left(\frac{v}{v_{St}}\right)^2\right) * \frac{v}{v_{St}} + F_C * tanh\left(\frac{v}{v_{Coul}}\right) + fv \qquad E.\ 4\text{-}1$$

$$v_{St} = \sqrt{2}v_{brk} \qquad E.\ 4\text{-}2$$

$$v_{Coul} = v_{brk}/10 \qquad E.\ 4\text{-}3$$

where,

- F_f is the friction force
- F_c is the Coulomb friction
- F_v is the viscous friction
- F_{brk} is the break away friction
- v_{brk} is the break away friction velocity
- v_{St} is the Stribek velocity threshold
- v_{Coul} is the Coulomb velocity threshold
- v is the relative velocity
- f is the viscous friction coefficient

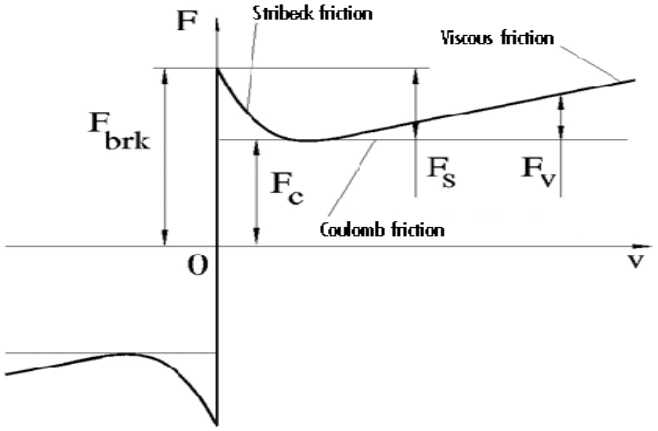

Figure 4-4 The components of the pure friction based on the Stribek friction model []

As the friction mainly consists of three parts, the Coulomb friction, the viscous friction and the Stribek friction, the model is built into the dynamic model of the MMR PTO and the unknown parameters are decided through the empirical data and using the minimum square principle. Figure 4-4 shows how each component of the friction contribute to the overall friction. The simulation results with friction compensation are illustrated in Figure 4-5 along with the test results. The friction model matches with the test results better. The model could be used to further analyse the composite of the friction terms and further improve the efficiency of the further prototypes.

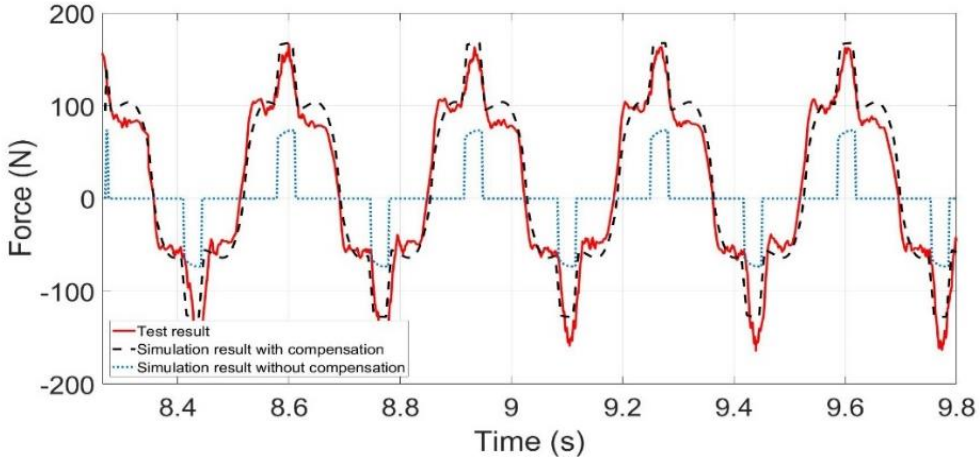

Figure 4-5 Test result and simulation result for the 50W MMR PTO with friction terms added to the dynamic model

The efficiency of the system is calculated and evaluated by two separate criteria. One is the overall efficiency calculated by dividing the output electrical power on the external resistor by the total input power of the PTO. The total input power is calculated by integrating the transient power over one time period.

The overall efficiency is the indication of the ratio between the input power and the usable electric power generated from the generator.

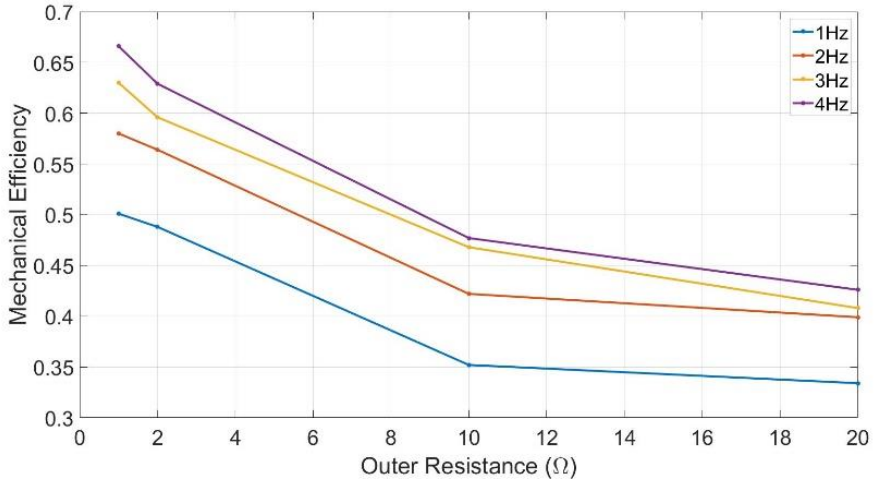

Figure 4-6 Mechanical efficiency of the 50W MMR PTO under various testing conditions

Another criterion is referred to as the mechanical efficiency, which is used to evaluate the mechanical transmission efficiency from ball nut to the generator. By taking the electricity lost on the inner resistor of the generator into account, all the energy lost will only be mechanical energy caused by friction and mechanical damping of the motion transmission. Compared with the overall efficiency, the mechanical efficiency is a more viable criterion to evaluate the motion transmission efficiency and thus is adopted in this paper.

Figure 4-6 shows the mechanical efficiency of the 50W MMR PTO under different test conditions in the lab. As expected, the efficiency increases along with the decrease of the resistance of the load or the increase of the PTO load. For larger PTO load, the portion of the friction lost will be relatively small and thus the mechanical efficiency will be better. On the other hand, when the test frequency increases, the mechanical efficiency increases as well. Two major reasons cause this result. Firstly, as the excitation frequency increases, the disengagement ratio is higher. In addition, when the friction increases, the force input

from the test machine towards the PTO is larger, and the friction caused loss will be relatively smaller, thus the MMR PTO efficiency increases.

4.3 Dynamic Performance Evaluation on 500W Prototype

4.3.1 Updated model of the MMR PTO

From the 50W prototype test, the concept of MMR PTO is verified. In addition, the dynamic model is refined through the test that it can give further guidance to the following testing. Due to some design issues, the friction can be a large source of efficiency loss for the MMR PTO and lead to an efficiency result that is not very satisfying. As a result, the design is further improved with more compact structure and better machining precision to build a larger prototype which is rated at 500W. The prototype is used to not only test on the efficiency, but also to verify how the three major parameters derived in the previous chapter, which are the equivalent mass, the damping coefficient and the excitation frequency, can influence the performance of the MMR PTO. This comprehensive study on the prototype can give further guidance for the future design on a utility scale and achieve better outcome.

Since the dynamic modeling with the friction terms added can predict the performance of the 50W MMR PTO accurately. In this section, a refined model is built for the 500W PTO so the experimental results can have more reliable references to look for.

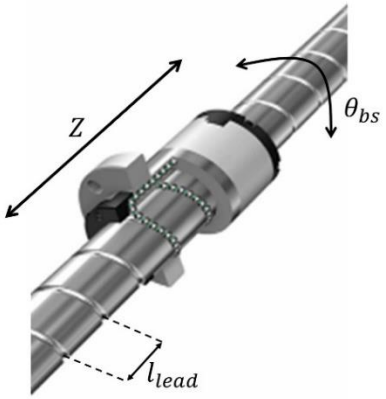

Figure 4-7 Schematic of the ball screw, which is capable of transforming the linear motion into rotary motion

A. Ball screw

The ball screw serves the function of "Motion Transformer" in the design, where the linear motion input of the PTO is transformed into the rotation motion. From the relationship illustrated in Figure 4-7, the kinematic transform using the ball screw can be described as:

$$\frac{z}{l_{lead}} = \frac{\theta_{bs}}{2\pi} \qquad E.\ 4\text{-}4$$

z is the displacement of the ball screw nut and the push-pull tube, l_{lead} is the lead length of the ball screw, and θ_{bs} is the rotation angle of the ball screw. As the consequence of the motion change, the input PTO force on the push tube is transferred into the torque on the ball nut of the ball screw. The ball nut and push-pull tube will also be driven, and the governing equation can be expressed according to the energy conservation law:

$$F_{pto}dz = T_{bn}d\theta_{bs} + \left(m_{bn} + m_{pt}\right)\ddot{z}dz \qquad E.\ 4\text{-}5$$

Here F_{pto} is the linear PTO force and T_{bn} is the external torque on the ball net from the ball screw, m_{bn} and m_{pt} are the mass of the ball screw and push-pull tube. By plugging E.4-4 into E.4-5$F_{pto}dz = T_{bn}d\theta_{bs} + \left(m_{bn} + m_{pt}\right)\ddot{z}dz$ E. 4-5, the relation between the PTO force and the torque on the ball screw can be written as:

$$F_{pto} = T_{bn}\frac{2\pi}{l_{lead}} + (m_{bn} + m_{pt})\ddot{z} \qquad E.\ 4\text{-}6$$

The torque on the ball nut will drive the ball screw and balance the torque transmitted through the MMR gearbox, which can be presented as:

$$T_{bn} = J_{bs}\ddot{\theta}_{bs} + T_{bs} \qquad E.\ 4\text{-}7$$

Here, J_{bs} is the moment of inertia of the ball screw, T_{bs} is the external torque on the ball screw from the MMR gearbox.

B. MMR gearbox

The MMR gearbox is the most important component of the proposed PTO. It is capable of converting the bidirectional rotation input into unidirectional rotation output and driving the generator. With the design of the MMR gearbox, the generator is capable of always rotating in one direction. The unique phenomenon of engagement and disengagement can be presented as the following condition:

$$\begin{cases} when\ \dot{\theta}_{in} = \dot{\theta}_{out} & \rightarrow \quad Engagement \\ when\ \dot{\theta}_{in} < \dot{\theta}_{out} & \rightarrow \quad Disengagement \end{cases} \qquad E.\ 4\text{-}8$$

Here, $\dot{\theta}_{in}$ and $\dot{\theta}_{out}$ are the rotation speed of the input shaft and output shaft respectively. When the MMR gearbox is in the status of engagement, the equation for gearbox transmission can be presented as:

$$T_{in} = T_{out} + \left(J_{is} + J_{cp}\right)\ddot{\theta}_{in} + T_f \qquad E.\ 4\text{-}9$$

Here, T_{in} is the input torque of the MMR gearbox from the ball screw, T_{out} is the torque on the output shaft of the MMR gearbox, J_{is} and J_{cp} are respectively the moment of inertia of the input shaft and coupling, and T_f is the friction torque in the MMR gearbox and generator bearings.

When the input shaft and output shaft are disengaged, however, the PTO system is separated into two subsystems that works independently with each other. One is the push-pull tube, ball nut, and the ball screw connected with the MMR input shaft. Another is the MMR output shaft, the generator and three bevel gears. Then, the input torque on the MMR gearbox from the ball screw can be presented as:

$$T_{in} = \left(J_{is} + J_{cp}\right)\ddot{\theta}_{in} + T_{fs} \qquad E.\ 4\text{-}10$$

Here, the output shaft is decoupled with the gearbox, hence it will be excluded from the dynamics of the gearbox. Since the main friction comes from the rotation transmission of the gears, the friction on the shaft can be smaller than T_f in the engaged case and is represented by T_{fs}.

C. Generator

The generator used in the test is a three-phase PMSG. The torque on the generator T_{ge} from the MMR output shaft can be broken down into two major sources: one is the rotation induced electric resistive torque T_{el} to generate electric energy, and the other is mechanical resistive torque T_{me} majorly from the moment of inertia of the generator:

$$T_{ge} = T_{el} + T_{me} \qquad \textit{E. 4-11}$$

To acquire the electric resistive torque, the electric voltage on each phase of the generator (annotated as Phase a, b and c) is expressed first as:

$$\begin{cases} E_a = k_e \dot{\theta}_{ge} sin\varphi \\ E_b = k_e \dot{\theta}_{ge} sin(\varphi + \frac{2\pi}{3}) \\ E_c = k_e \dot{\theta}_{ge} sin(\varphi - \frac{2\pi}{3}) \end{cases} \qquad \textit{E. 4-12}$$

Here, E_a, E_b, and E_c are the phase voltages of the generator, θ_{ge} and $\dot{\theta}_{ge}$ are the rotation angle and speed of the generator respectively, k_e is the voltage constant of the generator, φ is the electrical phase and it can be expressed by:

$$\varphi = \frac{p}{2}\theta_{ge} \qquad \textit{E. 4-13}$$

Here, p is the number of poles of the generator. Each phase of the generator is wired with an external resistor with same resistance using Y-shape which is illustrated in Figure 4-8, the electric current on each phase can be expressed by:

$$\boldsymbol{I} = \frac{\boldsymbol{E}}{R_{in}+R_{ex}}, \quad \boldsymbol{E} = (E_a, E_b, E_c), \boldsymbol{I} = (i_a, i_b, i_c) \qquad \textit{E. 4-14}$$

Here, i_a, i_b and i_c are respectively the current on each phase of the generator, R_{in} is the internal resistance on each phase of the generator and R_{ex} is the resistance of the external resistor connected to each phase of the generator, with the assumption of impedance from the internal inductance being much smaller than the sum of R_{ex} and R_{in}.

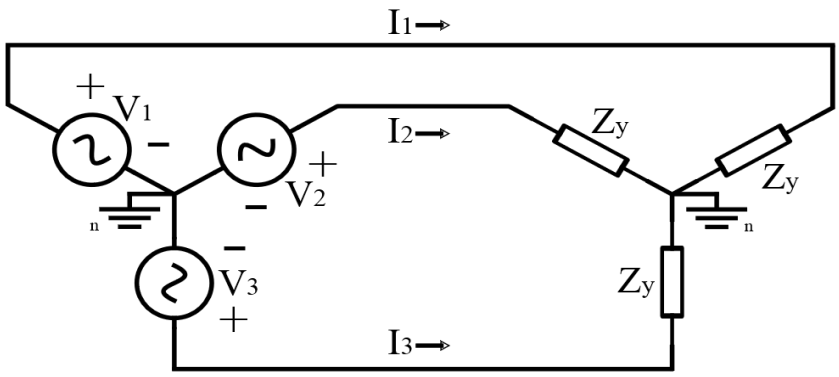

Figure 4-8 Y-shape wiring for the three phase generator

The electric torque load can be found by superposition of the output electric load on the three different phases, which is written as:

$$T_{el} = \frac{3k_e^2}{2(R_{in}+R_{ex})}\dot{\theta}_{ge} \qquad E.\ 4\text{-}15$$

Here, k_t is the torque constant of the generator. Since the electric torque is proportional to the angular speed of the generator, an equivalent rotary damping coefficient c_e is adopted here to describe the relationship between the electric torque and rotation speed of the generator:

$$c_e = \frac{3k_e k_t}{2(R_{in}+R_{ex})} \qquad E.\ 4\text{-}16$$

In addition to the electric torque, the inertia of the generator can induce torque as well. As the output shaft of the MMR gearbox and the connect coupling is constantly rotating in the same speed with the generator, the moment of inertia caused torque is considered here together with the generator, the mechanical resistive torque from the inertia is then represented as:

$$T_{me} = (J_{ge} + J_{cp} + J_{tg} + J_{fw} + J_{ss} + J_{os})\ddot{\theta}_{ge} \qquad E.\ 4\text{-}17$$

Here, $J_{ge}, J_{tg}, J_{fw}, J_{ss}$ and J_{os} are respectively the moment of inertia of the generator core, the transmission gears which are the three bevel gears inside the MMR gearbox, the flywheel, the side shaft, and the output shaft of the MMR gearbox.

D. Friction

The friction of the PTO comes from the interactions and connections of the mechanical components, which includes the revolution friction between the ball screw and ball nut, the friction from the gear meshing and bearings, etc. It is the major source for the energy loss in mechanical components for the designed PTO in this paper compared with other factors including the impact force from backlashes and possible misalignment during the assembling. As a result, it is added to the modeling of the PTO for the previous work of Penalba et al. has pointed out that the over-simplified PTO model can lead to large over-estimation of the total power absorption [79]. In the proposed MMR PTO, the friction is mainly dominated by the rotation transmission of the gears. The friction from different components of the PTO are combined as one term and presented using the following equation:

$$F_f = \begin{cases} F_c + (F_s - F_c)e^{-\left(\frac{v}{v_s}\right)^2} + c_v v & if\ v \neq 0 \\ F_e & if\ v = 0 \end{cases} \qquad E.\ 4\text{-}18$$

where F_f, F_c, F_s, c_v and F_e are the total friction force, the Coulomb friction, the Stribeck friction, the viscous friction coefficient, and the maximum static friction, v and v_s are the velocity of the PTO and the relative velocity threshold for the Stribeck friction. The model introduced is used to describe the PTO under constant movement, when the PTO movement speed is zero, however, the static friction can be any value that is smaller than F_e depending on how much force is cast to start the PTO.

E. Dynamic analysis for the PTO

The components of the PTO system are assembled in series, and the MMR gearbox has a gear transmission ratio of 1:1, the relationship between the components can be acquired:

$$\begin{cases} T_{bs} = T_{in}, \theta_{bs} = \theta_{in} \\ T_{out} = T_{ge}, \theta_{out} = \theta_{ge} \end{cases} \qquad E.\ 4\text{-}19$$

When the MMR gearbox is at the status of engagement, $\theta_{in} = \theta_{out}$, by combining the separated dynamics of each component in series, the dynamic equation for the MMR PTO can be presented as:

$$F_{pto} - F_f = \left[\left(J_{bs} + J_{is} + J_{tg} + 2J_{cp} + J_{ge} + J_{fw} + J_{ss} + J_{os}\right)\frac{4\pi^2}{l_{lead}^2} + \left(m_{bn} + m_{pt}\right)\right]\ddot{z} + \frac{6k_e k_t \pi^2}{(R_{in}+R_{ex})l_{lead}^2}\dot{z} \quad \text{E. 4-20}$$

Here, F_f is the overall friction for the entire PTO. At the time when the system is engaged, the PTO force on the push tube will drive all the components to move together as one system. The shafts, gears, and couplings used in the prototype all have large stiffness that they are treated as rigid body, so there exists no spring term in the dynamic equation. The friction term F_f is from the whole system which relates with the friction torque T_f as $F_f = T_f \frac{2\pi}{l_{lead}}$.

When the MMR gearbox is at the status of disengagement, $\theta_{in} < \theta_{out}$, however, the overall system is separated into two subsystems, one is the ballscrew and MMR input shaft driven by the PTO force, and the other is the generator which uses the kinetic energy stored in the inertia in exchange for the electric energy and continue generating power. The dynamic equation for the two subsystems under disengagement can be described as:

$$\begin{cases} F_{pto} - F_{fs} = \left[\left(J_{bs} + J_{is} + J_{tg} + J_{cp}\right)\frac{4\pi^2}{l_{lead}^2} + \left(m_{bn} + m_{pt}\right)\right]\ddot{z} & Subsystem\ One \\ (J_{cp} + J_{ge} + J_{fw} + J_{ss} + J_{os})\ddot{\theta}_{ge} + T_f + \frac{3k_e k_t}{2(R_{in}+R_{ex})}\dot{\theta}_{ge} = 0 & Subsystem\ Two \end{cases} \quad E.\ 4\text{-}21$$

Here, F_{fs} is the friction term on the subsystem one, which majorly exist in the ballscrew and push-pull tube, and it is small compared with the friction in the engaged case dominated by the MMR gearbox. The two subsystems are independent to each other so each of them can be solved individually. By considering only the viscous damping term c_v or equivalent viscous damping for the friction model $T_f = c_v\dot{\theta}_{ge}$, which is the electric damping. The solution for the rotation speed of the subsystem two is an exponentially decaying curve, which can be expressed as:

$$\dot{\theta}_{ge} = \dot{\theta}_0 e^{kt}, k = -\frac{c_e + c_v}{(J_{cp} + J_{ge} + J_{fw} + J_{ss} + J_{os})} \quad E.\ 4\text{-}22$$

Here, $\dot{\theta}_0$ is the rotation speed of the generator at the time when disengagement happens. With the dynamic equations for the MMR PTO when it is both engaged and disengaged, another important task is to find out the timing when MMR system disengages and its

corresponding influence factors. Here, we assume that the MMR PTO is driven by a sinusoid input with an excitation frequency of $f_{ex}\ in\ Hertz$ and the maximum rotation speed is defined by $\dot{\theta}_{max}$. At time t_0 the disengagement happens, and the equation for the disengaged time can be described as:

$$\dot{\theta}_{max}\ sin\big(2\pi f_{ex}(t_0+\Delta t)\big) = \dot{\theta}_{max}\ sin(2\pi f_{ex}t_0)\ e^{k\Delta t} \qquad \Delta t \to 0 \qquad \textit{E. 4-23}$$

It is easy to acquire the following equation by using trigonometric expansion to the left side of the equation:

$$\dot{\theta}_{max}\sin\big(2\pi f_{ex}(t_0+\Delta t)\big) = \dot{\theta}_{max}[\sin(2\pi f_{ex}t_0)*\cos(2\pi f_{ex}\Delta t)+\sin(2\pi f_{ex}\Delta t)*\cos(2\pi f_{ex}t_0)] \qquad \textit{E. 4-24}$$

When $\Delta t \to 0$, it can be assumed that $\sin(2\pi f_{ex}\Delta t) = 2\pi f_{ex}\Delta t$ and $\cos(2\pi f_{ex}\Delta t) = 1$, replace these conditions back into E.4-24 and it becomes:

$$1 + 2\pi f_{ex}\Delta t * cot(2\pi f_{ex}t_0) = e^{k\Delta t} \qquad \textit{E. 4-25}$$

Use Taylor expansion for $e^{k\Delta t}$ when $\Delta t \to 0$:

$$e^{k\Delta t} = 1 + k\Delta t + \frac{(k\Delta t)^2}{2!} + \frac{(k\Delta t)^3}{3!} + \cdots \qquad \textit{E. 4-26}$$

Plug in E.4-26 back into the previous equation and ignore the high order infinite small terms from the Taylor expansion, the time t_0 where disengagement happens can be solved analytically and can be expressed as:

$$t_0 = \frac{1}{2\pi f_{ex}}\left[arccot\left(\frac{-(c_e+c_v)}{2\pi f_{ex}(J_{cp}+J_{ge}+J_{fw}+J_{ss}+J_{os})}\right)+n\pi\right], n = 0,1,2,3\cdots \qquad \textit{E. 4-27}$$

It is easy to observe from the equation that the initial disengage time is related to the excitation frequency f_{ex}, the equivalent damping coefficient of the generator $c_e + c_v$, and the inertia $(J_{cp} + J_{ge} + J_{fw} + J_{ss} + J_{os})$ that can store energy during the excitation motion. As it can be found out by further interpreting the equation, the initial disengage time turns to be earlier when the excitation frequency is higher, the inertia is larger, or the equivalent damping coefficient is lower.

After a certain time, the exponentially decayed speed of the generator will equal the speed of the input speed of the MMR gearbox, and the two subsystems will reengage into one.

This meeting time, however, is governed by a transcendental equation that can only be solved numerically. It can be assumed that the increase of the inertia and the decrease of the electric damping coefficient can smooth the decay curvature and increase the disengaged time. This assumption is verified later in the testing part. Additionally, the disengage time in the period can be further interpreted using the nondimensionalized term $\epsilon = \frac{c_e+c_v}{2\pi f_{ex}(J_{cp}+J_{ge}+J_{fw}+J_{ss}+J_{os})}$ and disengagement ratio $\mu = \frac{t_{dis}}{t_p}$ where t_p is the period time and t_{dis} is the total disengaged time in one period. The relationship between these two terms can be found in Figure 4-9

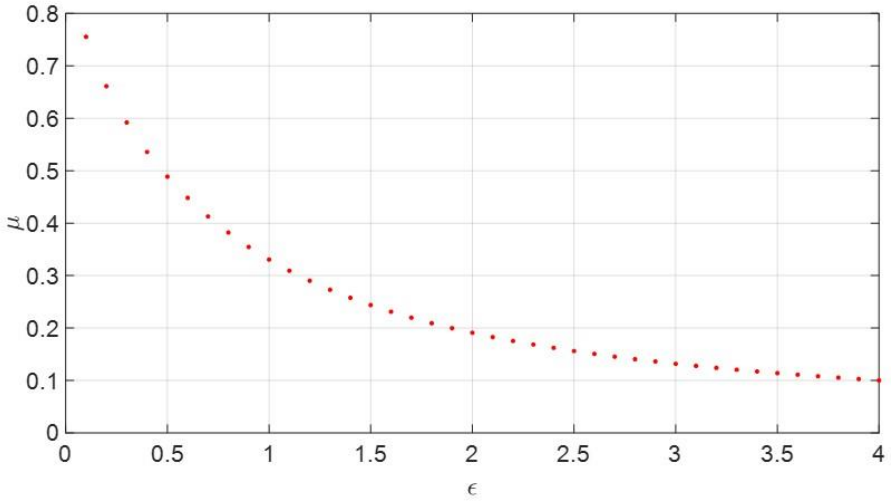

Figure 4-9 Nondimensionalized term ϵ influence on the disengagement ratio μ

4.3.2 Test set-up

Figure 4-10 shows the 500W prototype mounted on the Instron 8801 hydraulic test machine. Different from the 50W prototype that the two push rod can counter the torque generated during the testing, two linear guide rails are used on the test machine to prevent the possible rotation of the linear actuator to guarantee the test accuracy. The force and displacement measurements are recorded with a sampling frequency of 100Hz by the Coco-80 data recorder and DSA from the Crystal Instruments. A power resistor is connected with each phase of the generator as the electric load, whose resistance can be tuned based on the test requirement to bring in different damping coefficient for the PTO. Electric current and voltage on each phase of the generator are also recorded using Coco-80. The values of all the parameters related to the PTO prototype are listed in Table 2.

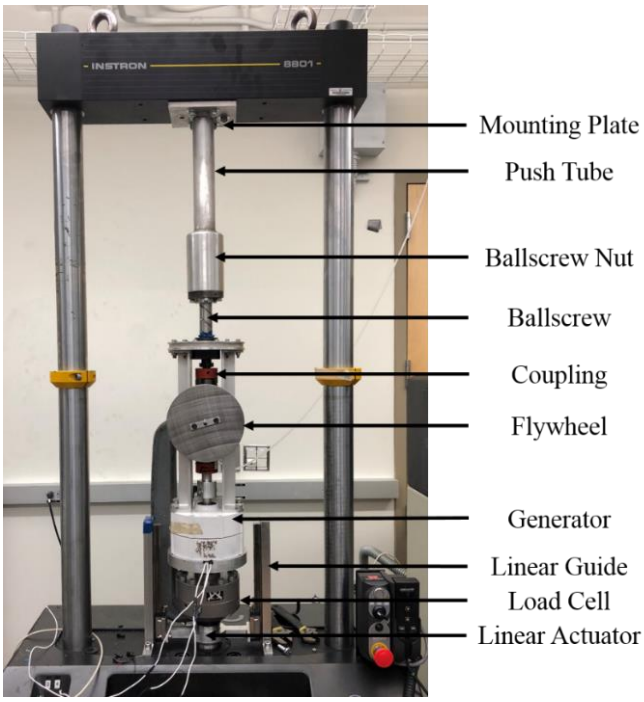

Figure 4-10 Dry lab test set-up for the 500W MMR PTO

4.3.3 Test result analysis

Figure 4-11 shows the input force of the testing machine towards the prototype under the excitation of triangle displacements of 2Hz (square-shaped speed). The generator works in open-terminal state without any external resistance, so the recorded force can only be the friction from the PTO. Through multiple test conditions under different strokes and speeds, the unknown terms of the friction can be determined using the least square method for refining the dynamic model of the PTO system. It is noticeable that some force fluctuation still exists when the velocity is constant, this phenomenon can be explained from two reasons. Firstly, since multiple mechanical transmission components are used in the PTO design, some impact and shock can happen due to the backlash or the misalignment and can cause some unexpected force; Secondly, since the testing machine used a PID controller, some overshoot and fluctuation can also influence the input force towards the PTO, especially when the speed input wave forms are in square and the driving direction can change suddenly.

Table 2 Parameters for the components used in the 500W prototype

Physical meaning	Symbolic expression	Value
Moment of inertia of ballscrew	J_{bs}	$2.34 \times 10^{-4}\text{kg} \cdot \text{m}^2$
Moment of inertia of input shaft	J_{is}	$7.64 \times 10^{-6}\text{kg} \cdot \text{m}^2$
Moment of inertia of transmission gears	J_{tg}	$4.20 \times 10^{-5}\text{kg} \cdot \text{m}^2$
Moment of inertia of couplings	J_{cp}	$1.40 \times 10^{-4}\text{kg} \cdot \text{m}^2$
Moment of inertia of generator	J_{ge}	$5.63 \times 10^{-3}\text{kg} \cdot \text{m}^2$
Moment of inertia of flywheel	J_{fw}	$Based\ on\ choice$
Moment of inertia of side shaft	J_{ss}	$4.52 \times 10^{-6}\text{kg} \cdot \text{m}^2$
Moment of inertia of output shaft	J_{os}	$3.06 \times 10^{-6}\text{kg} \cdot \text{m}^2$
Mass of the ballscrew nut	m_{bn}	1.78kg
Mass of the push tube	m_{pt}	2.16kg
Lead distance of the ballscrew	l_{lead}	60mm
Electric constant of the generator	k_e	$1.31\text{rad}/(\text{s} \cdot \text{V})$
Torque constant of the generator	k_t	$764\text{mN} \cdot \text{m/A}$
Internal resistance of the generator	R_{in}	1.24Ω

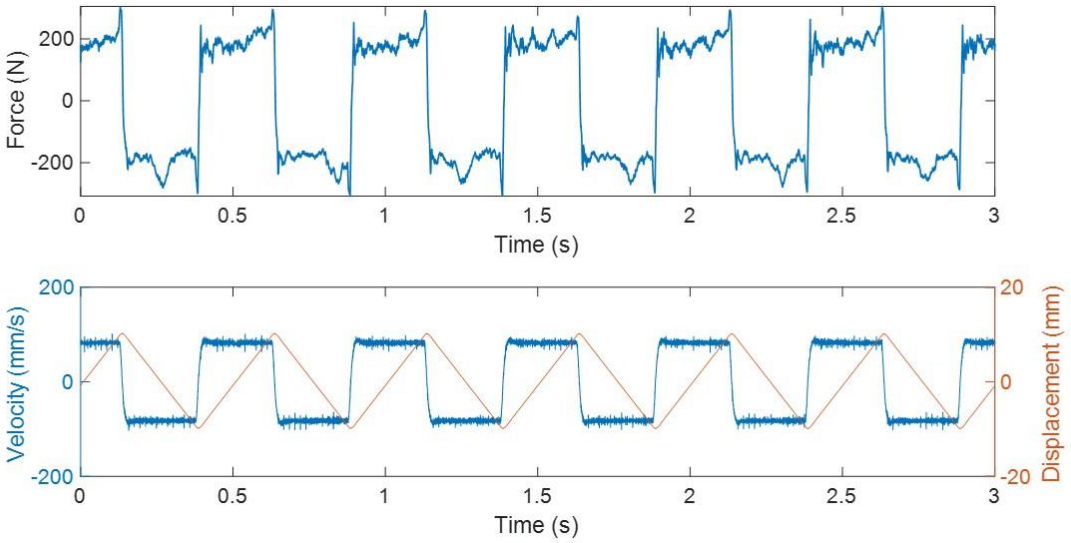

Figure 4-11 Force, velocity, and displacement of the MMR PTO under the excitation of a constant speed with no electric load

Figure 4-12 shows both the test results of the actuating force applied to the PTO under the excitation of a sinusoid wave with frequency of 3Hz and a displacement of 5mm. The wiring for the PMSG is in Y-shape and the external resistor attached to each phase of the generator is 10Ω. No flywheel is attached to the side shaft of the gearbox. The left side of Figure 4-12 is the force of the MMR PTO, and the right figure is the force of non-MMR PTO where the MMR gearbox is replaced by a traditional direct transmission gearbox which uses one shaft to directly transmit the motion. It can be observed from the experiment that the MMR PTO is consisted of two statuses of engagement and disengagement. When MMR PTO is disengaged, the dominant force is the friction. When it is engaged, the system operates with the PTO load again, so the force increases sharply. For the non-MMR PTO, however, the force follows the pattern of the sinusoid excitation and is smoother regardless

of the fluctuation caused by the meshing of the mechanical components and the control overshoot from the Instron's hydraulic actuator controller.

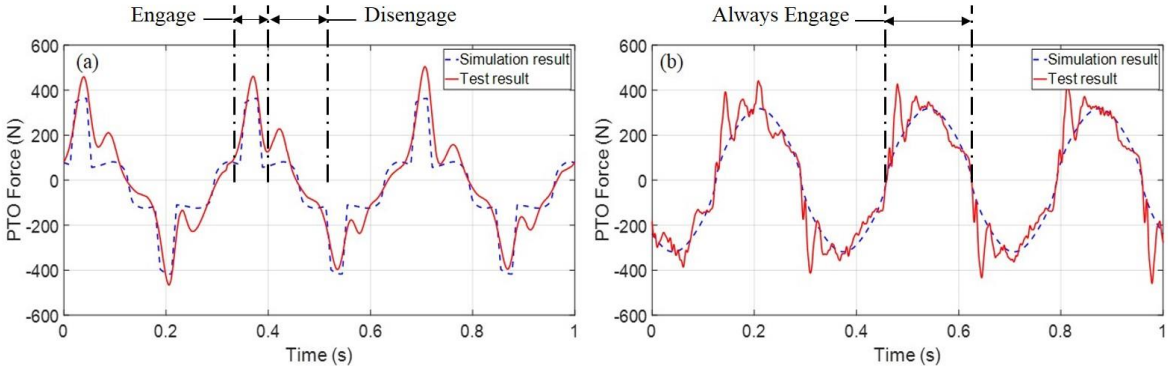

Figure 4-12 The tested and simulated force of (a) MMR PTO and (b) non-MMR PTO under the excitation of a sinusoid wave with a displacement of 5mm at 3Hz, the external resistor is 10Ω with no flywheel attached

The simulation results with the friction characterized are also shown in Figure 4-12 in dash lines. The simulation results match well the performance of the test results, indicating that the dynamic model could work well on predicting the performance of the PTO. In addition, the results proves that the except for some impact force, the friction model achieved good match with the real force, and the friction can be identified as the major factor for the energy loss in the mechanical system. It is also noticeable that the force on the MMR PTO is not identical when it is operated in two different directions. This is because the transmission process is not the same, one direction of the MMR PTO is transmitted directly through one one-way clutch, whereas for the other direction, the transmission has to go through three bevel gears to change the rotation direction. However, if the gearbox is well-designed and aligned well, the force difference between the two sides can be reduced because the gear transmission efficiency is high.

After the disengagement (freewheeling) phenomenon is verified through the comparison between the MMR PTO and non-MMR PTO, further tests are conducted to explore how different equivalent mass, damping, and excitation frequency would influence the performance of the MMR PTO.

Further tests are conducted with different flywheel attached on the MMR side shaft. The moment of inertia of the two different flywheels are shown in Table 3.

Figure 4-13 illustrates the force and voltage output of MMR PTO with a flywheel attached on the MMR side shaft, the moment of inertia of the two different flywheels are shown in Table 3. We give harmonic displacement excitation of 10mm amplitude and 3Hz frequency. The electric load is 10Ω on each phase of the generator. From Figure 4-13, it can be observed that the one with the larger moment of inertia has a larger input force, which matches well with the dynamic modeling for the MMR PTO.

Table 3 Moment of inertia for different flywheels used in the experiment

(The baseline moment of inertia without any flywheel is $5.71 \times 10^{-3} \mathrm{kg} \cdot \mathrm{m}^2$)

Flywheel	Moment of Inertia ($\mathrm{kg} \cdot \mathrm{m}^2$)
No flywheel	0
Flywheel No.1	8.35×10^{-3}
Flywheel No.2	1.67×10^{-2}

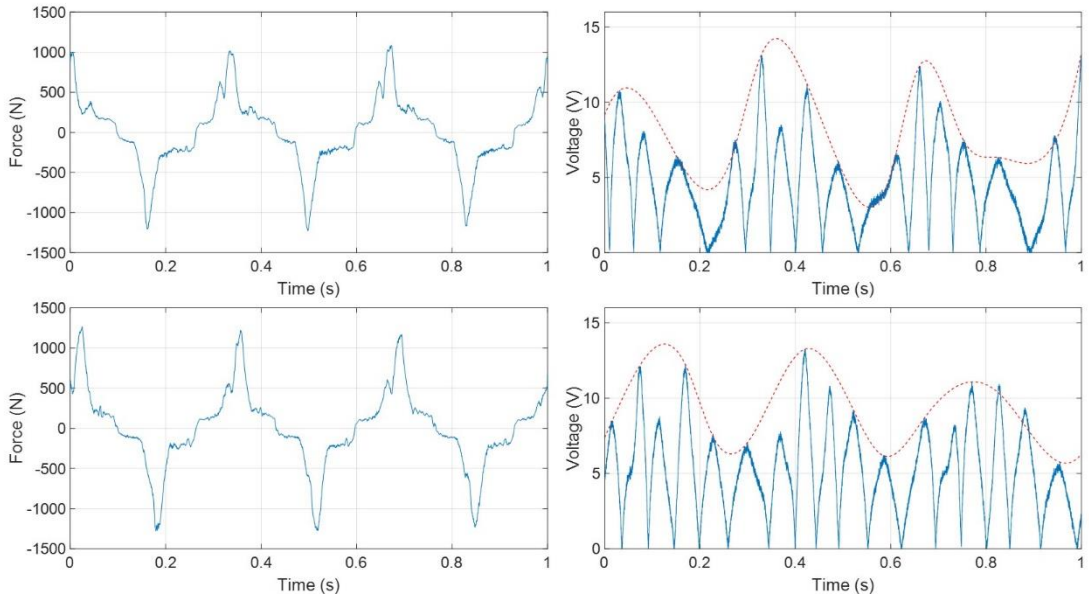

Figure 4-13Top: Force and voltage response of the PTO with flywheel No.1 attached Bottom: Force and voltage response of the PTO with flywheel No.2 attached. Under sinusoid excitation of 10mm amplitude and 3Hz frequency, with external resistance is 10Ω on each phase

The right side of Figure 4-13 shows the voltage signals on one phase of the generator. It can be seen that the voltage output of the MMR PTO with larger flywheel inertia has a relatively steadier overall envelope line, which means that the generator with larger flywheel in the MMR PTO has a slower voltage decaying and more steady rotation speeds. The damping influence to the reaction of the MMR PTO is illustrated in Figure 4-14. The flywheel used in the test is flywheel No.2 with the harmonic excitation of 10mm and 3Hz, and the external resistance on the two test groups is 10Ω and 5Ω on each phase of the PMSG. The electric damping increases as the external resistance becomes smaller. Figure 4-14 (left subfigures) shows that the PTO force with smaller external resistor is larger which is because of the large electrical damping force. Figure 8 right subfigures also shows the voltage fluctuation with small electric damping is smaller, indicating that the disengagement ratio can be negatively affected by the increase of damping.

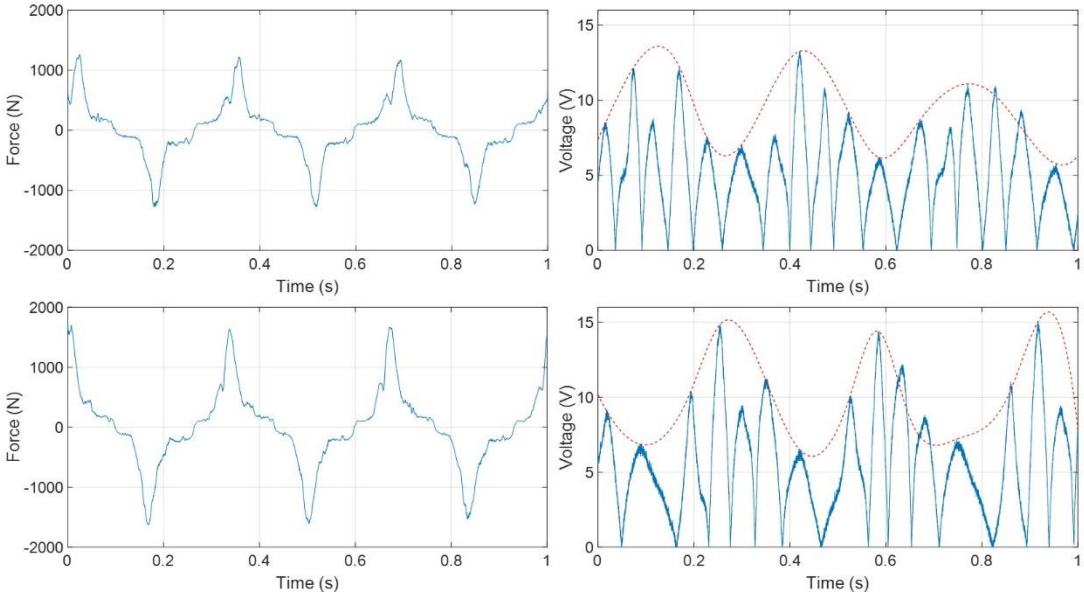

Figure 4-14 Top: Force and voltage response of the PTO with 10Ω external resistance. Bottom: Force and voltage response of the PTO with 5Ω external resistance. Under sinusoid excitation of 10mm amplitude and 3Hz frequency, flywheel No.2 attached

The damping not only changes the disengaged ratio, but also brings difference to the dynamic response to the system. Figure 4-15 shows the force-displacement loop of the MMR PTO under the excitation of 3Hz. The figure shows that different external resistance load not only influence the disengage ratio, but also the position where the maximum PTO

force appears. When the external resistance is large, the disengagement happens earlier, re-engagement is late, and this the disengagement ratio is large. In such case the peak force also appears late in the circle.

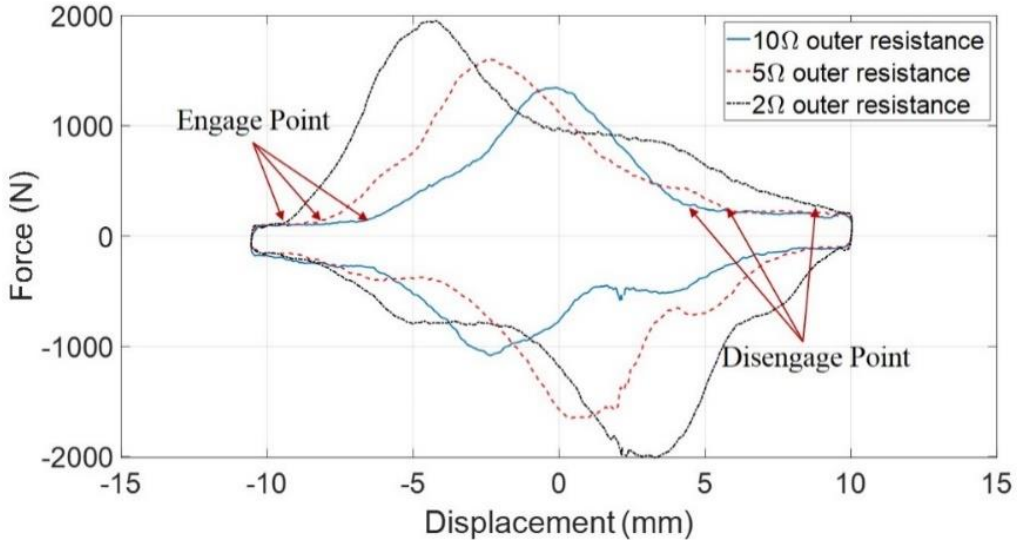

Figure 4-15 Displacement-Force loop of the MMR PTO under the excitation of a sinusoid wave with a displacement of 10mm at 3Hz, the external resistance are 10Ω, 5Ω and 2Ω

At last, the influence of the excitation frequency is shown in Figure 4-16. The flywheel used in the test is flywheel No.2, and the external resistance on the two groups test is 0.5Ω on each phase of the PMSG. The two frequency choices are 0.5Hz and 3Hz. As it can be observed from the figure, when the excitation frequency is 0.5Hz, the force reaction of the MMR PTO is similar to the non-MMR PTO, indicating that there is no disengagement or the disengagement ratio is very small. When the excitation frequency is 3Hz, the disengagement is more obvious, showing the increase of the excitation frequency can help the MMR PTO to achieve higher disengagement ratio.

From the test results, the analytical solution is verified that the increase of rotation inertia and excitation frequency and the decrease of the damping coefficient can contribute to a larger disengagement ratio.

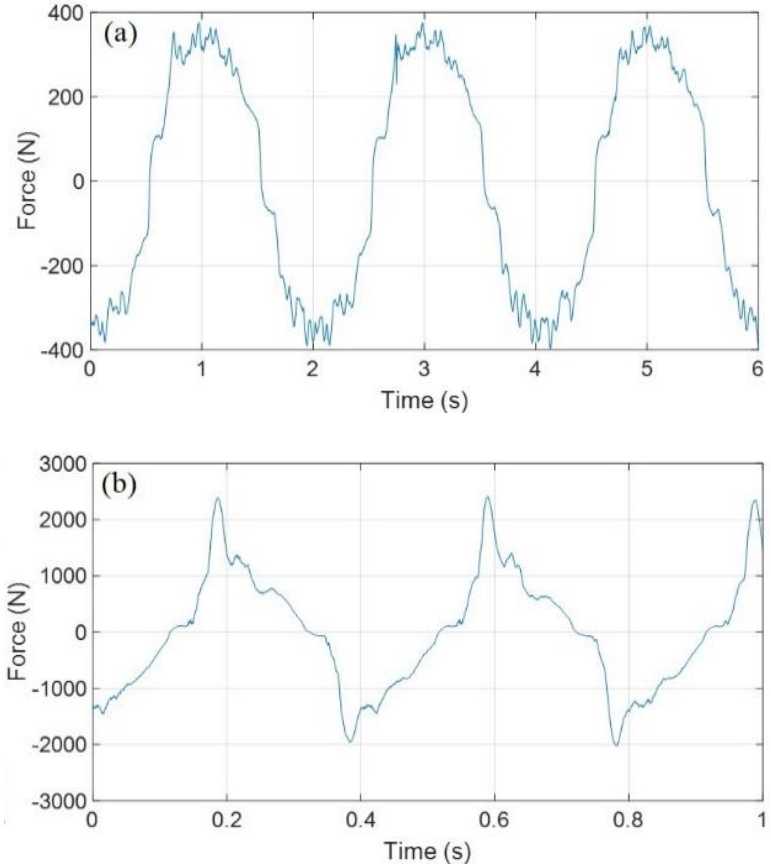

Figure 4-16 Force of MMR PTO under the excitation of a sinusoid wave with a displacement of 10mm at 0.5Hz in (a) and 3Hz in (b), the external resistor is 10Ω and the attached flywheel is flywheel No.2

The influence of the three parameters – rotation inertia, damping coefficient and excitation frequency are discussed individually for their influence to the disengagement of the MMR PTO. As we see in the modeling part, the combined influence can be represented using a dimensionless term $\epsilon = \frac{c_e+c_v}{2\pi f_{ex}(J_{cp}+J_{ge}+J_{fw}+J_{ss}+J_{os})}$. Figure 4-17 shows the relationship of the disengaged ration and the dimensionless term ϵ. Each point in the figure represents one group of test results with different combinations of rotation inertia, damping coefficient and excitation frequency in terms of ϵ value. The results show that the dimensionless term ϵ has an influence on the disengagement ratio μ, and the trend of the influence is close to the simulation result previously introduced in Figure 4-9. The difference at small ϵ might be from the imperfection of the mechanical system and the judgement on the disengagement. The overall results shows the increase of the ϵ has a positive effect on the

disengagement ratio μ. From the test results, it can be observed that by decreasing ϵ, the disengagement ratio can be increased. However, it can be noticed that the maximum ratio for disengagement achieved in the experiments is around 0.4. This is because in the real test situation, the existence of the higher order terms of the friction in the decoupled system can result in large resistive force and reduce the total disengagement period. As a result, the disengagement ratio is limited to a certain value. Considering that in the real working conditions, the MMR PTO does not expect to have a very large disengagement ratio, and since the current model has proved that it can predict the performance well. Consequently, modelling of the higher order term factor in the friction is not considered in this paper.

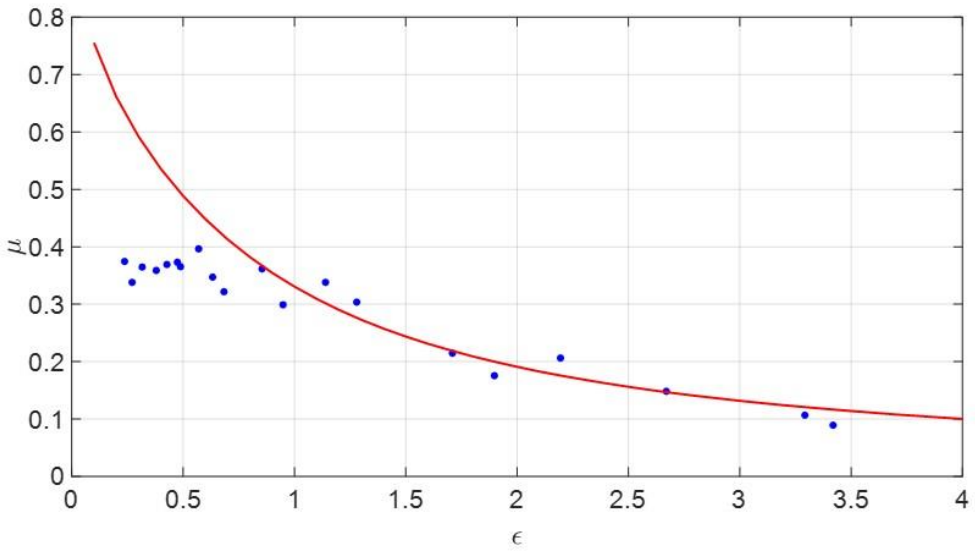

Figure 4-17 Nondimensionalized term ϵ influence on the disengagement ratio μ based on test results

In addition to the disengaged ratio, the mechanical energy transfer efficiency is also an important factor for evaluating the performance of the PTO. The efficiency is calculated by dividing the total electric power on both internal and external resistors over the mechanical power input:

$$Efficiency = \frac{P_{elec}}{P_{mech}}\left(\frac{R_{in}+R_{out}}{R_{out}}\right) \qquad E.\ 4\text{-}28$$

where, P_{mech} is the average mechanical input power from the actuator to the prototype, P_{elec} is the average electric output power on the external power resistor.

Figure 4-18 compares the efficiencies between the MMR and non-MMR PTO without flywheel. The test used the same prototype and the only difference between the two groups of test is the gearbox to achieve the variable control. For the test results shown in Figure 4-18(a), the test is conducted with an external resistance of 1Ω on each phase of the PMSG, whereas the external resistance on Figure 4-18(b) is 10Ω. From the previous test, it can be concluded that when the electric damping is large and disengage ratio is small, the MMR PTO has similar performance with the non-MMR PTO. The energy transfer efficiency test proves this conclusion. However, when the electric damping is small, the MMR PTO can have a much higher efficiency compared with the non-MMR PTO because the MMR PTO has a large disengage ratio and the generator can have a steady rotation speed, indicating another benefit of having large disengagement ratio. The highest mechanical efficiency detected is about 81.2% during the test, exceed some previous design, showing that the MMR PTO can achieve good energy conversion performance.

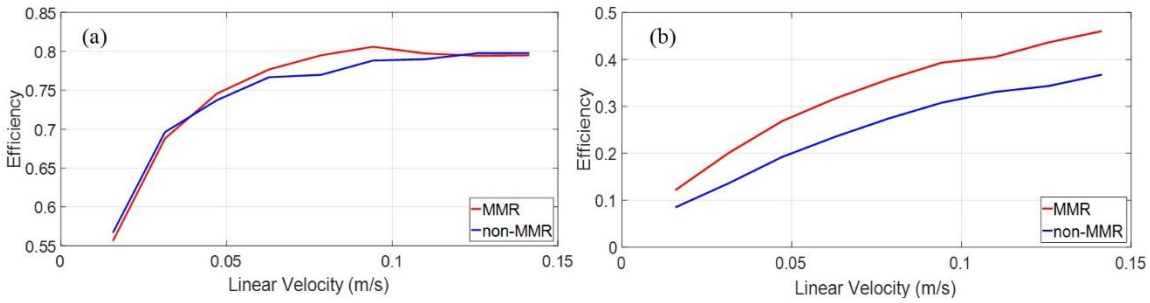

Figure 4-18 Comparison of the efficiency between MMR PTO and non-MMR PTO under different velocity, the external load is 1Ω in (a) and 10Ω in (b), no flywheel is attached

It can be noticed from Figure 4-18 that the efficiency is influenced not only by the external resistance, but also by the linear velocity the test can achieve. To further explain the conditions that can influence the performance of the PTO efficiency, Figure 4-19 illustrates the efficiency of the PTO under different load and excitation conditions. It can be read from the figure that two factors can greatly influence the efficiency: one is the external resistance, and the other is the linear velocity that the PTO reaches. When the external resistance is large, the force from the electric damping is low and the friction dominates. As a result, the efficiency becomes low. When the linear velocity is low, the PMSG works at its low efficiency zone, thus the overall efficiency is influenced as well. It is also

noticeable that the optimum efficiency results showed in the Figure 4-19 is slightly lower than the one showed in Figure 4-18, this is because some components broke during the test and the replaced component caused larger friction. So the test result of the efficiency is about 6.8% lower than the results showed in Figure 4-18.

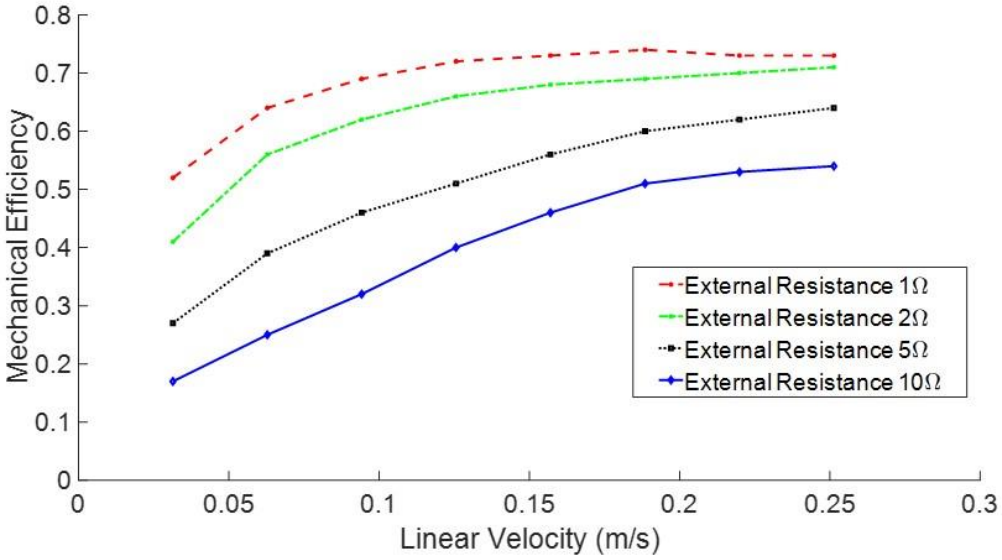

Figure 4-19 The efficiency of the designed MMR PTO under different test linear velocities with different external resistance

From the bench test of the 500W PTO, the dynamic model for the designed MMR PTO is verified and unknown parameters are characterized. The mechanically driven PTO achieved good energy transfer efficiency and have advantages over the non-MMR PTO.

4.4 Reliability Test on Larger Scale Prototype (10KW PTO)

In addition to the smaller scale testing of the 50W and 500W scale, the 10kW prototype is developed for further testing on the reliability improvement of the prototype. Due to the stroke limit and power limit of the small scale test machine, both the 50W and 500W prototypes are only tested with small stroke, which can only be used for characterizing the dynamic property of the PTO but not mimicking the real-world input from the ocean. As a result, the 10kW scale prototype is designed to have large input stroke that can pair with the horizontal linear hydraulic actuator to achieve large force input and large stroke limit.

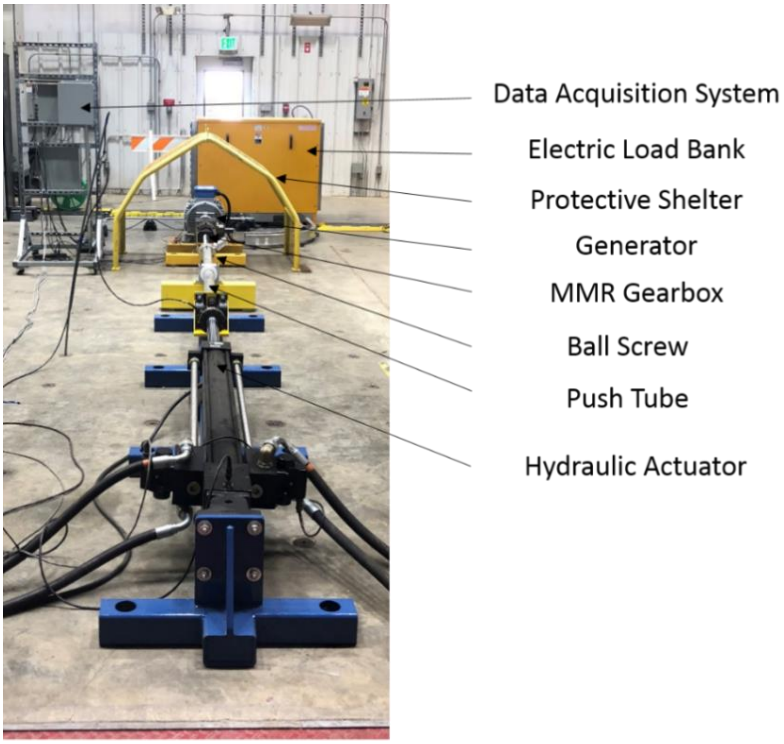

Figure 4-20 The test set-up of 10kW scale MMR PTO prototype

Figure 4-20 shows how the 10kW prototype is tested in NREL, with a hydraulic linear actuator used to drive the prototype and provide input to the system. The design of the 10kW prototype is similar to the previous prototypes yet placed in horizontal direction. The floor of the testing facility is strengthened to provide support that can hold the PTO with acceptable deformation, so that the test results are not influenced and distorted. A 50kW rated load bank is used to dissipate the energy generated during the test. Multiple sensors are adopted to monitor different parameters during the test and recorded by the DAQ. These parameters include the linear input displacement, the force, the temperature of the generator and the gearbox, the rotation speed and the torque of both the input and output side of the MMR gearbox.

Figure 4-21 illustrates the time domains of the input power, input force and linear input speed from the hydraulic actuator towards the MMR PTO with *irregular input* waveform. The input towards the PTO is simulated using time domain approach with the consideration of the characterized dynamics of the PTO. The irregular wave is generated with Bret-Schneider spectrum with a dominant wave period of 3s and significant wave height of 1m

(power flux density 1.47KW/m). The peak to RMS average ratio of the velocity is 4.2 times with the maximum linear velocity of 1.08m/s and RMS average velocity of 0.26m/s. The characterization is achieved through the previous regular wave tests. At the electrical load condition L5 (load is chosen to allow generator to achieve 5kW of power when rotated at rated speed), the peak output power it reached is 18.85kW. The average output power is 1.51kW, and the peak to average ratio is 12.5, which is a reasonable number for irregular wave conditions. In addition, the peak force is 30.84kN and the average force is 3.91kN with a peak to average ratio of 7.9.

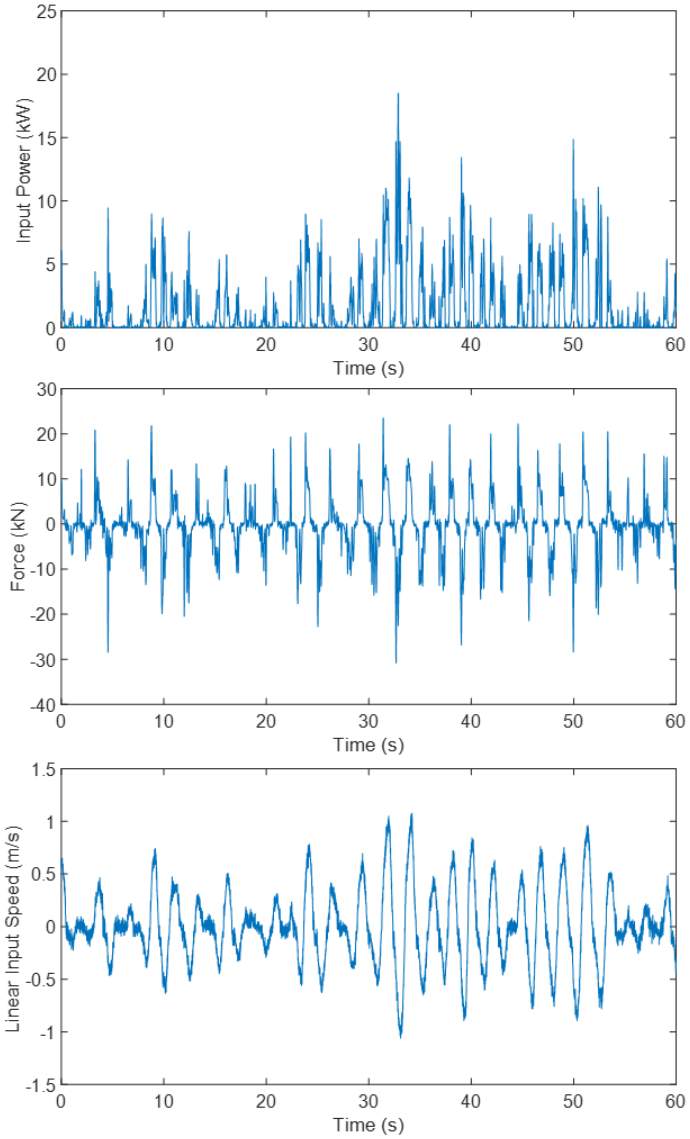

Figure 4-21 Input power, force and linear speed to the MMR PTO using irregular wave condition with 5kW electric load

From the previous irregular wave test, it can be found that the peak to average ratio can be very large and lead to an extremely high value of peak force, which is harmful for the reliability of the system.

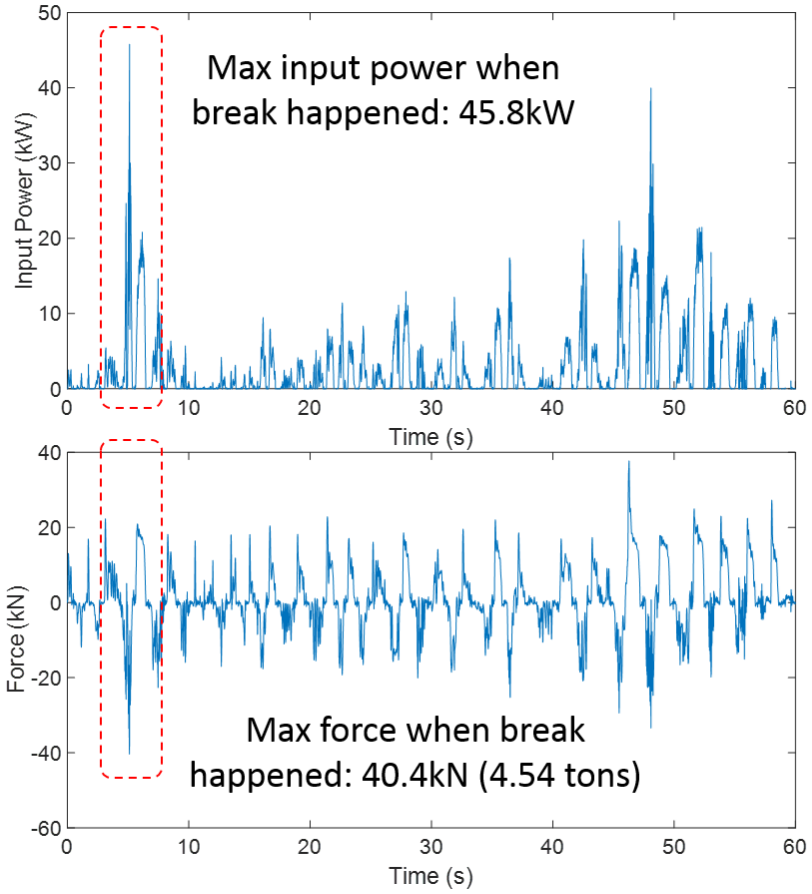

Figure 4-22 Input power and force to the MMR PTO using irregular wave condition when the break mode detected

We gradually increase the electrical load (reducing the load resistance) and drive the gearbox to failure. Figure 4-22 shows the time domain of the input power and force towards the MMR PTO when the break happened where half cycle of power gradually loss is detected. The peak power achieved at the test is 45.8kW and the peak force is 40.4kN, which is about 9 times of the designed input power, showing that the design was robust yet the strategy for countering the high peak to average ratio need to be further improved.

Through the dry lab testing of the 10kW ratio prototype, the performance of the MMR PTO is verified again. The first failure mode is detected, and design experience is gained. The design of the MMR PTO and new strategy, either through control or through more robust

design, for solving the issue of high peak to average ratio will be the main target for the future work.

Figure 4-23 shows the failed part of the MMR gearbox. The input side one-way clutch broke. All the gears survived well. The gears were supported by the bearings on the gearbox housing.

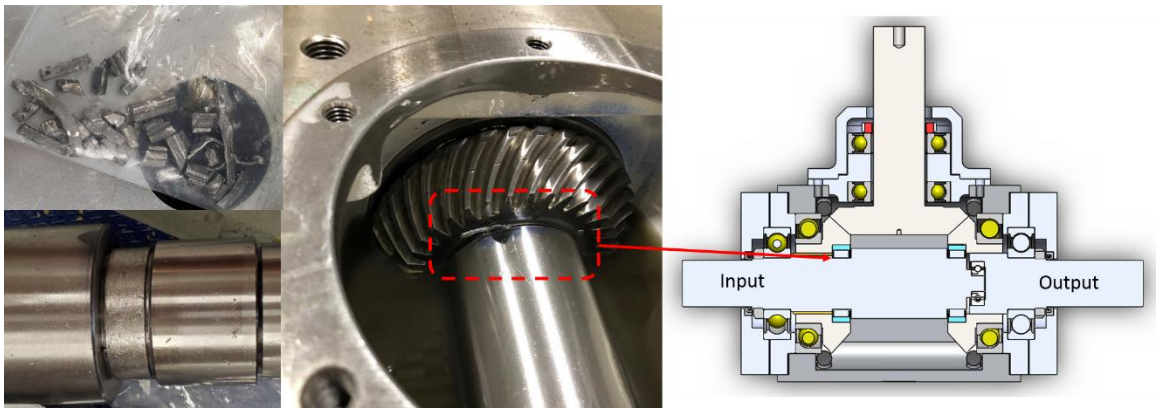

Figure 4-23 The failed one way clutch

From the figure, it can be observed that both the one-way clutch and the shaft it set on have failed. The insert element of the one-way clutch break, and the surface of the shaft is scratched. There are two major possible reasons for this situation. The first reason is due to the misplacement of the clutch, in the slot there exist some room for the consideration of heat expansion of the clutch component, however, the spare room granted the clutch some freedom to move, and it may result the clutch to move to undesired place and fail during the operation. The second reason is there may exist some misalignment, the input shaft and the input side gear are aligned with separate reference, so there may exist some misalignment during the manufacturing process, as the one-way clutch is the link component between the input shaft and the input gear, it may be damaged due to misalignment.

4.5 Chapter Summary

In this chapter, through a series of dry lab testing of the MMR PTO in different scales, multiple achievements have been accomplished.

The tests have verified the performance of the MMR PTO, as the engagement and disengagement effect can be found from the test. The unique phenomenon is able to

improve the efficiency of the PTO when the speed is low or the damping coefficient is small. A 50% of efficiency improvement compared with traditional linear non-MMR PTO can be detected through the test.

The dynamic model of the MMR is refined through the tests. A more accurate model with friction considered is established and have matched well with the test results. The refined model can predict the performance of the MMR PTO well under different load conditions, which is very useful when it is assembled together with the WEC for deployment.

The defects of the design are found during the testing process that the design improvement have been constantly ongoing. The structure of the prototype is simplified with more compact design. Moreover, the reliability is improved by adopting several approaches on improving the maintenance. In addition, the potential failure modes under the irregular wave conditions are detected and can be further improved for a more reliable PTO design in the future.

5. Wave tank test of self-reactive point absorber with MMR PTO

5.1 Chapter Introduction

The performance of the MMR is verified through in-lab test, yet further verification is desired to test it with a WEC. In this chapter, two major work is done: One is to conduct experiment on the WEC with MMR PTO to find out how the MMR PTO can perform; the other is to explore how different configurations of a point absorber can influence the total energy absorption. Through the work described in this section, the WEC with MMR PTO proved its quality through the water tank test with different configurations. The comparison between the configurations are also concluded.

5.2 Wave Tank Test Set-up

To verify the performance of the proposed WEC, the prototype of a two-body WEC was assembled and tested in the water tank at the Alfond W2 Ocean Engineering Lab in the University of Maine. The water tank is 30 meters long, 9 meters wide with the water depth as 4.7 meters. The beach of the water tank has a porous structure and is able to minimize the influence the reflection wave to the WEC. A wave probe was set at 4.88 meters away from the wave maker to monitor the wave condition during the test. The WEC prototype was placed 11.15 meters from the wave maker. The column of the second body is guided to only allow heave motion with linear bearing mounted on a bridge across the water tank. A load cell was assembled between the two bodies to record the force input towards the PTO. In addition, the relative motion between the two bodies was monitored by a string pot. The output voltages from the generator at different electrical resistances were recorded as well. All the signals from the sensors were loaded into a DAQ system. Figure 5-1 shows the tank layout with general dimensions.

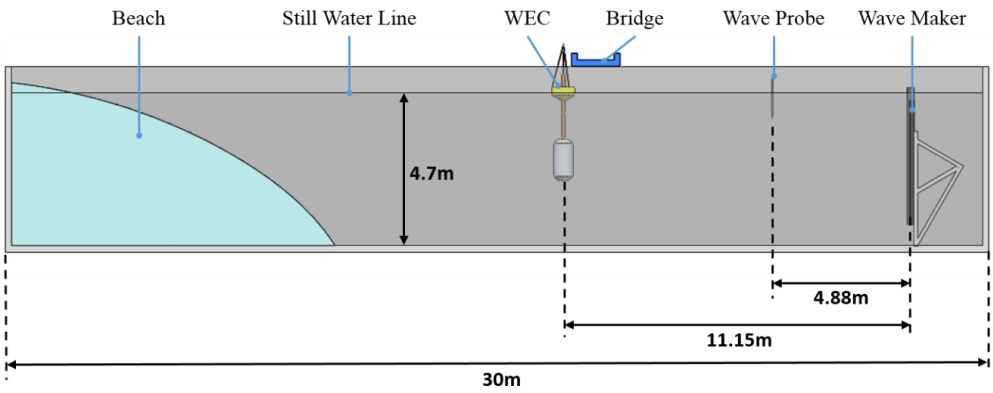

Figure 5-1 Wave tank layout and dimensions

A 1:30 scale point absorber that assembled with the 50W PTO was selected to accommodate the wave tank capabilities [80]. The model consists of a floating buoy, a PTO column (which houses the PTO components) and a submerged body, which is connected to the bottom of the PTO column. During setup, additional buoyancy was added to keep the submerged body afloat while additional weight was added to the bottom to ensure its center of gravity was below its center of buoyance. The device configuration are shown on the left of Figure 5-2.

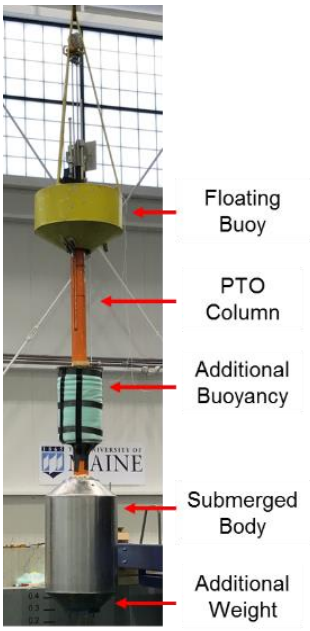

Figure 5-2 Configuration of the tested self-reactive point absorber

To characterize the WEC dynamic precisely and verify the previous simulation results, body mass property test and free decay tests were conducted separately for both bodies to identifying the unknown terms. The process is illustrated in Figure 5-3. Figure 5-3(a) and Figure 5-3(b) describe the body identification for the buoy and the second body, they were lifted by a forklift and swung in air to acquire the property of center of the gravity and the dry mass. A breakdown of the physical properties for the floating buoy and the submerged body (including the PTO column) is given in Table 4.

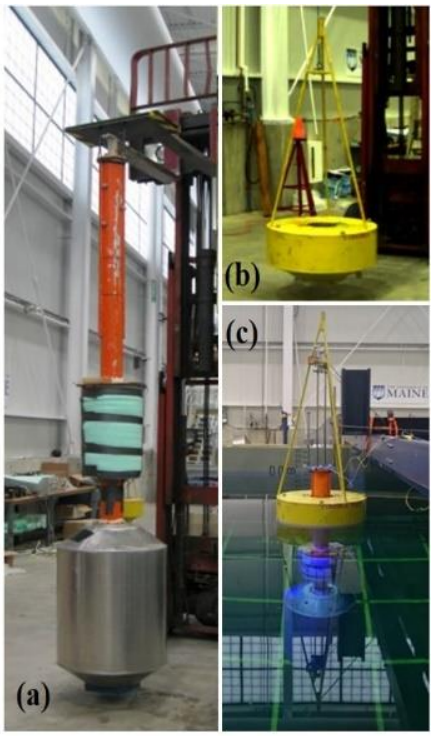

Figure 5-3 Body identification and free decay test of the water tank test

In the free decay test for the buoy, the floating buoy was pushed into water with an initial displacement first. Due to the hydrostatic restoring force, the body started to move in heave when it was released. The motion gradually decayed as the result of radiation damping and drag damping. A similar approach was used for the second body as well. Figure 5-4 shows the free decay test results for the two bodies. The result was then used through curve fitting to verify the hydro parameters. The added mass parameters match well with the simulation results, the damping terms, however, is larger. This is due to the drag damping, as a result, additional viscous damping coefficient is added based on the curve fitting results as compensation [81].

Table 4 Properties of the 1:30 scale WEC model

Quantity	Floating Buoy	Submerged Body
Mass (kg)	60.10	334.20
CG (cm from bottom)	35.63	57.71
Pitch Period (sec.)	2.87	3.54
Pitch MOI (kg-m^2)	29.10	410.70

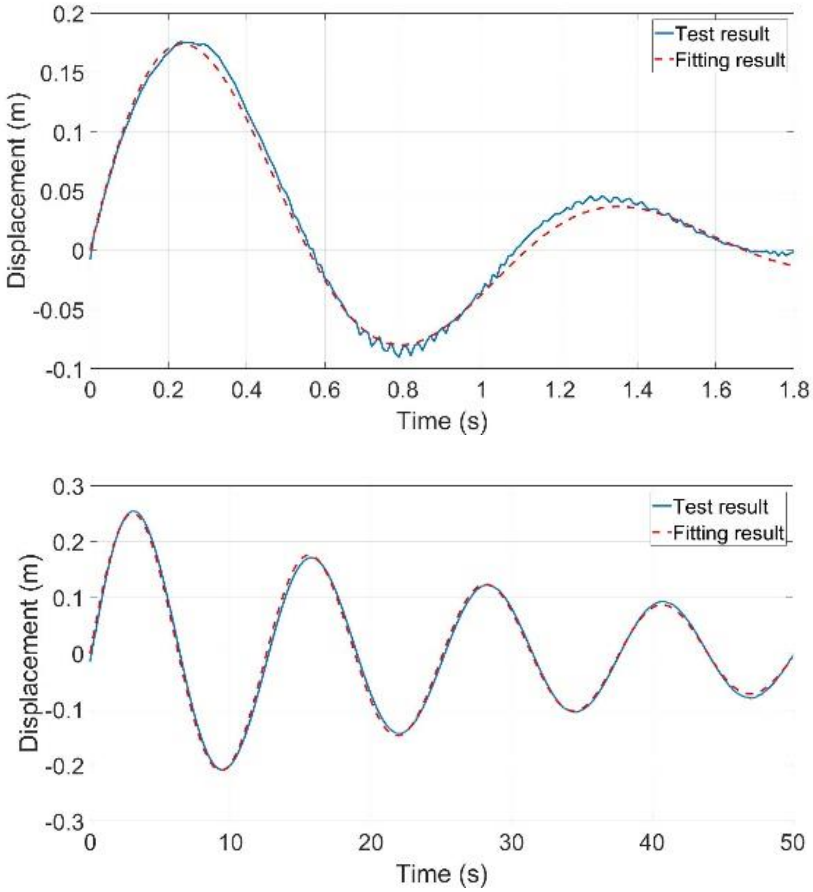

Figure 5-4 Left: Free decay test results and fitted results for the buoy; Right: Free decay test results and fitted results for the second body

There are three configurations tested in the water tank, as illustrated in Figure 5-5. The first one illustrated in Figure 5-5 is the typical design for a single body point absorber, where a floating buoy moves along the incident wave. The buoy is guided by a rigid structure which in the figure is represented by a column. The buoy moves along the structure and is constrained only to the heave direction. Thus, only one degree of freedom (DOF) z_1 need to be taken into consideration. The motion of the buoy is then adopted to drive the power take-off (PTO) and generate electricity.

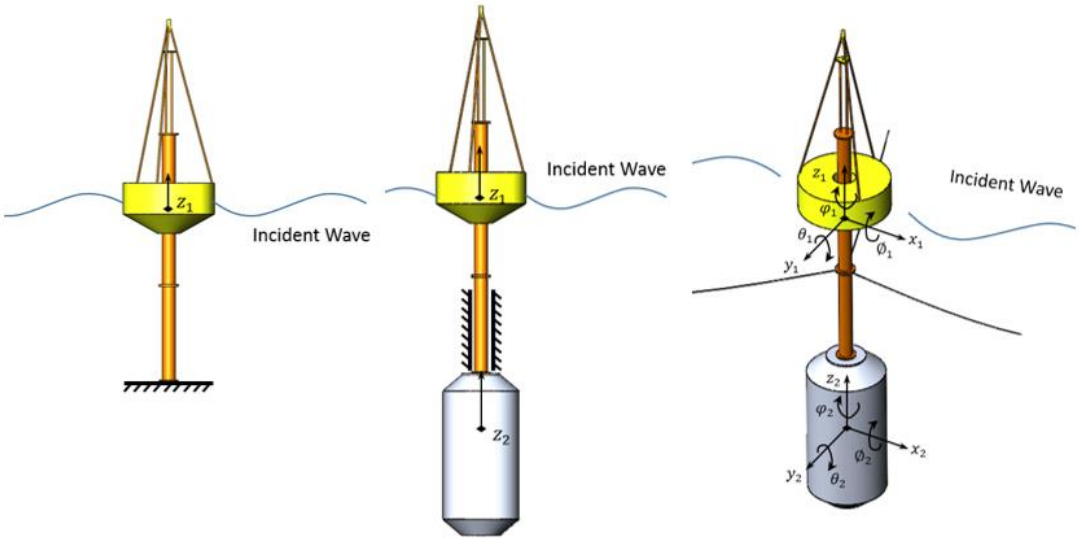

Figure 5-5 Three configurations of set-up used in the wave tank test

The second one is the two body wave energy point absorber, consisting of one floating buoy and a neutrally buoyed submerged body. Energy is absorbed through the relative motion between the two bodies. Such design has the advantage that the natural frequency of the system has high flexibility for adjustment. The study of the two body point absorber usually regards the system as a two body system. Only two DOF, z_1 and z_2, is considered. For the idealized case shown in the figure, the column is constrained in all rotary, surge and sway motion to simplify the dynamic analysis.

The last subfigure of Figure 5-5 shows the general situation where mooring is added to the two body point absorber. The energy abstraction remained comes from the relative motion between the z_1 and z_2. The individual body is free to move in all DOF. The mooring lines

will provide soft constrain to the system. For x_1, y_1, z_1, $\emptyset_1$, θ_1 and φ_1, each of them represents the surge, sway, heave, pitch, row and yaw motion of the floating body. Similarly, for x_2, y_2, z_2, $\emptyset_2$, θ_2 and φ_2, each of them represents motion of the submerged body respectively.

For all these configurations, the MMR PTO is adopted in the design. However, due to time constraint, the non-MMR PTO is not tested as comparison. Thus, only the data with MMR PTO is acquired for the test.

Table 5 Wave conditions used in the water tank test

Run	Wave Type	1:30 Scale		Full Scale	
		Period (s)	Height (m)	Period (s)	Height (m)
1	Mono	1.64	0.053	9.00	1.58
2	Mono	1.83	0.065	10.00	1.95
3	Mono	2.01	0.079	11.00	2.36
4	Mono	2.19	0.094	12.00	2.81
5	Mono	2.37	0.110	13.00	3.30
6	Mono	2.56	0.128	14.00	3.83
7	Mono	2.74	0.146	15.00	4.39
8	Poly	2.83	0.173	15.50	5.20

Table 5 listed all the wave conditions that has been tested on the different configurations. Here, the mono wave refers to the regular wave input towards the WEC, and the ploy wave refers to the irregular waves. The irregular wave used in the test are generated by using the Bret-Schneider wave spectrum. For regular mono waves, the total test time is 5min per wave condition due to the fact that it usually take 30~50 seconds for the WEC to reach to steady state. For the irregular wave, however, the total tested time length is 30min to avoid the high standard deviation caused issue.

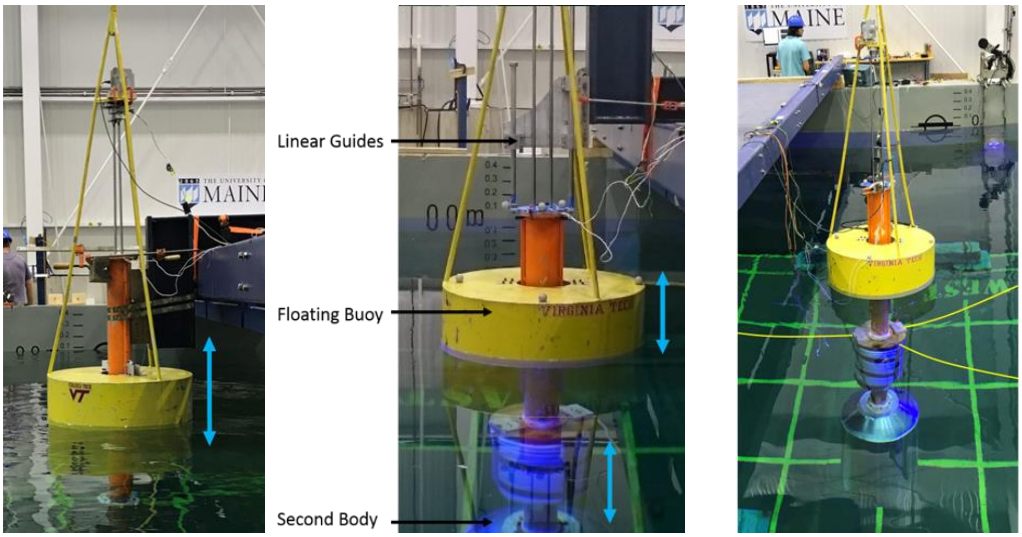

Figure 5-6 The set-up for the three different configurations: single-body WEC in heave motion (1 DOF), two-body WEC in heave motion (2 DOF), and two-body WEC with three-point mooring (6DOF)

Figure 5-6 illustrates the set-up for three different configurations during the test. For the single body 1DOF set-up, the column is fixed on the bridge through clamps and only the floating buoy is able to move in heave. Similarly, for the 2DOF test, a linear guide system is used for the second body as illustrated in the figure. Both the floating buoy and the second body is restricted to the heave motion only. At last, the subfigure on the right of the figure shows the test setup for the 6DOF system, three mooring lines are fixed on the proposed prototype to provide the mooring force as illustrated.

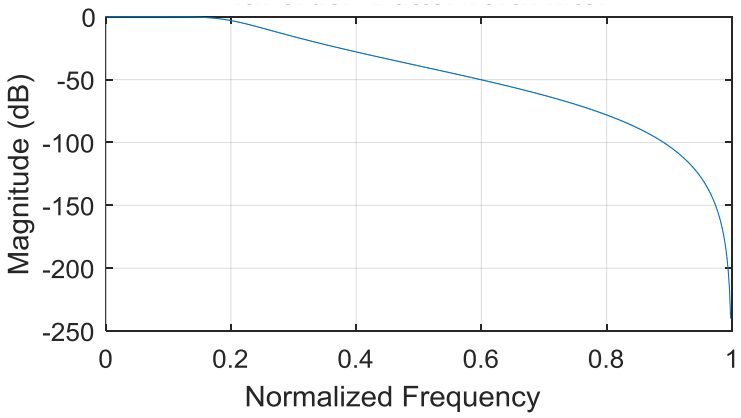

Figure 5-7 4th order low-pass Butterworth filter used for processing data

The DAQ collected signals during the test are later processed for further analysis. A fourth order low-pass Butterworth filter with the cutoff frequency of 20Hz as illustrated in Figure

5-7 is used when processing the data to eliminate the noises generated from the inner impedance of the DAQ and other sources. The comparison between the data before and after the processed by the filter is illustrated in Figure 5-8.

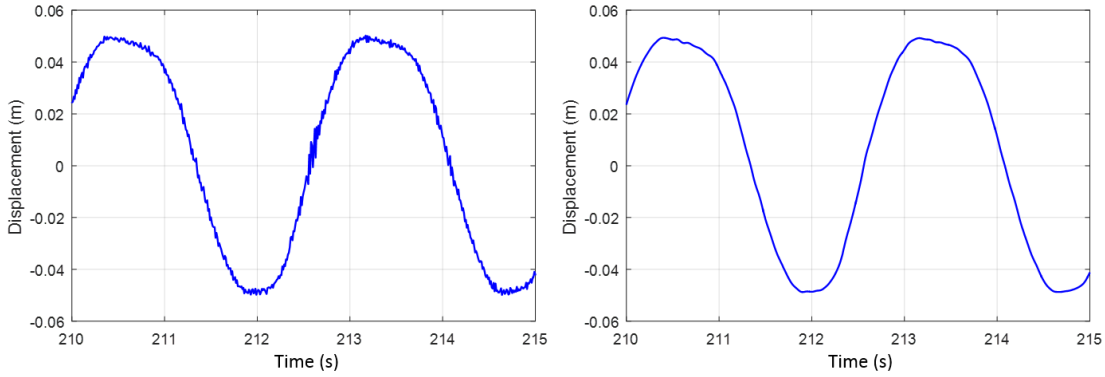

Figure 5-8 Time domain data before and after processed with filter

5.3 Compare Between the Single Body Point Absorber (1DOF) and the Two Body Self-reactive Point Absorber (2DOF)

There are two separate criteria used for comparing the performance of the 1DOF and 2DOF point absorber. One is the power absorption from the waves, which is the total mechanical power the prototype extracted from the wave. The other is the power output which considered the power loss during the transmission process, which includes the mechanical loss due to the friction and impact loss of the mechanical components and the electric loss due to the existence of the impedance in the generator and wire. The first criteria is more important for theoretical study because the nonideal factors are neglected, and the second one is more important for the real application because it takes the usable power into consideration.

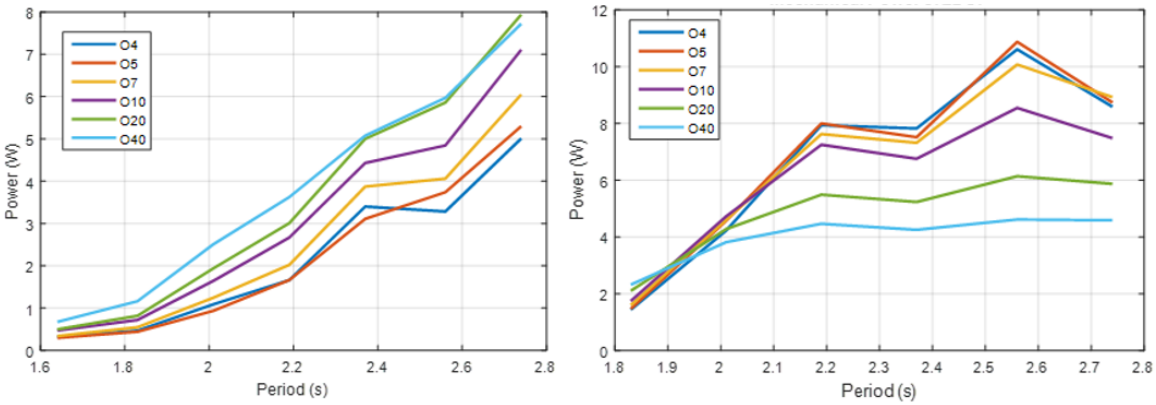

Figure 5-9 Left: Total power absorption of the 1DOF point absorber from the wave; Right: Total power absorption of the 2DOF point absorber from the wave

Figure 5-9 shows the compare between the total power absorption of the prototype in the 1DOF and 2DOF configurations under different wave conditions listed in Table 5. The label in the figure represents different external resistance used during the test, which are 4Ω, 5Ω, 7Ω, 10Ω, 20Ω, and 40Ω.

From the left of Figure 5-9, it can be observed that for the 1DOF configuration, the power absorption follows the trend of the wave power flux and no obvious peak can be observed. It can also be noticed that the optimal external resistance for most of the wave conditions are 40 Ω, which lead to relatively small damping coefficient from the PTO, indicating that the maximum power is achieved when the damping coefficient of the PTO is small and the movement stroke of the point absorber is large.

The right side of the Figure 5-9 shows the power absorption from waves for the 2DOF configuration, and it is easy to observe that one peak can be reached near the wave with 2.6s of period. In addition, the power absorption increases with smaller external resistance, which indicate that the larger the damping coefficient, the higher the power extracted from the wave. While the performance of 4Ω external resistance is still better than the 5Ω one, it can be told that the optimum power absorption hasn't been achieved and still have potential for better performance, yet it also means more energy will be waste on the electric components.

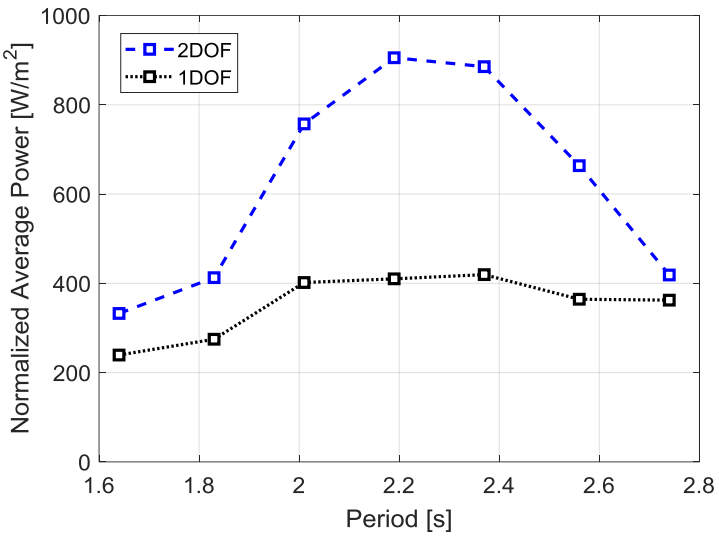

Figure 5-10 Normalized power absorption of the 1DOF and 2DOF set-up

To address the peak more clearly and avoid the different wave height caused influence. Figure 5-10 illustrated the normalized power on the 2DOF set-up by dividing the absorbed power by the square of the wave height. From the normalized power, it is obvious that the peak has been achieved by adopting the two body self-reactive structure.

Comparing the 2DOF regular wave results to the 1DOF results on the power absorption from waves, shown in Figure 5-10, the 2DOF model produced over twice the amount of power as the 1DOF model, consistent with the simulation results in Section 2. From the figures, it can be observed that the 2DOF can almost double the power absorption even when the optimal damping coefficient is not achieved and still has potential for further improve.

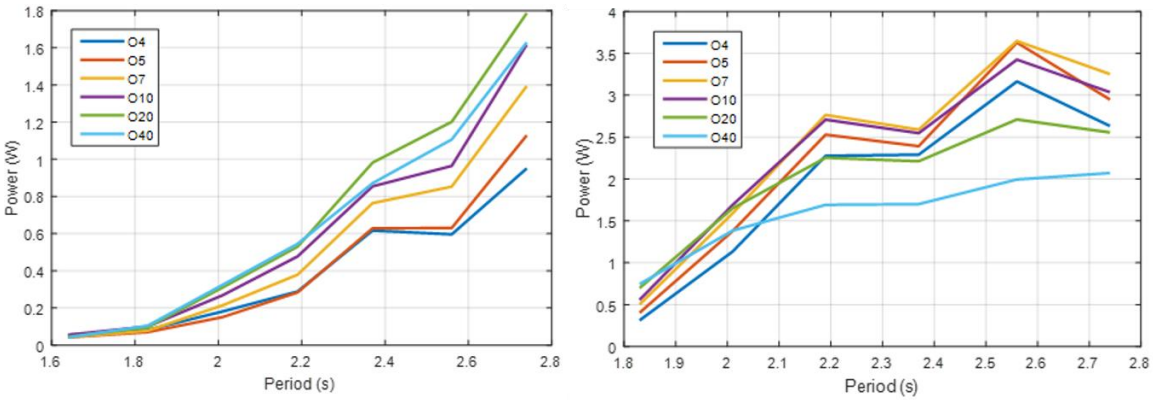

Figure 5-11 Left: Total electric power output of the 1DOF point absorber from the wave; Right: Total electric power output of the 2DOF point absorber from the wave

However, when the other criteria, the electric power output from the point absorber is adopted, the performance evaluation can be changed. From Figure 5-11, it can be observed that for the output electric power, the optimal external resistance is different from the power absorption. For the 1DOF configuration, the optimal damping for power output is 20Ω and for the 2DOF configuration is 7Ω. This is because the existence of the impedance in the generator and wire can also divide voltage, the smaller the external resistance, the higher the voltage loss and lead to smaller electric power output. The optimal external resistance on the electric power output is also used in the irregular wave test which is introduced later to achieve the highest possible power generation.

In addition to the frequency domain data, the time domain model also functioned well with the refined PTO dynamic model from the previous bench test.

Figure 5-12 compares the test results of regular wave test with wave No.5 and No.7 on a 2DOF test configuration, the results show that as the wave height is higher, the WEC has larger relative displacement, larger PTO force as well as larger output voltage from the generator. The external resistance used in the tests shown in Figure 5-12 is 20Ω for both cases. In addition, some latching phenomenon where a flap shows up at the maximum displacement can be observed for both group of tests, this is resulted from the existence of the static friction and can be simulated well using the previously introduced friction model.

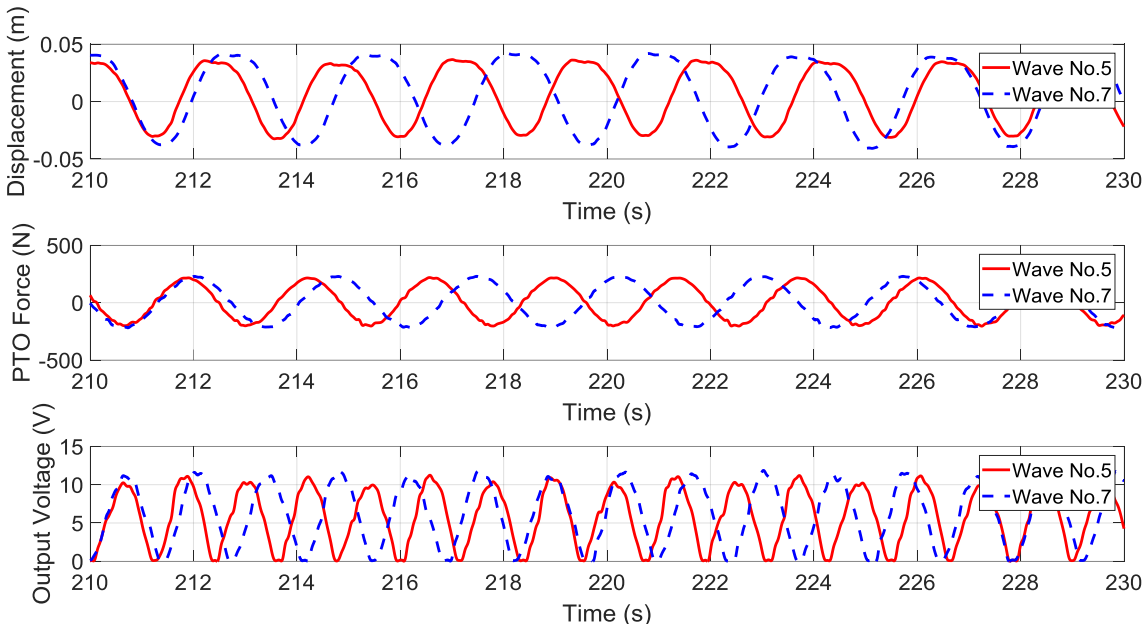

Figure 5-12 Compare of the test results between wave No.5 and wave No.7

Figure 5-13 illustrates the compared simulation and test results for both tests that are introduced in the previous figure. It can be observed that with the friction terms added towards the dynamic modeling, the simulation results can predict the latching phenomenon as well as the PTO force accurately and unanimously, indicating that the dynamic model of the PTO is characterized well and capable to be adopted for performance prediction of the WEC.

However, it is worth noticing that the predicted voltage is higher than the actual voltage measured during the test. This may result from several reasons. First of all, the parameters used in the simulation are constant, however, due to the small wave height of the test, the rotation speed of the generator is not able to reach its rated condition, and that may lead to low efficiency of the generator. Secondly, it can be observed that the voltage signal has some uneven shapes during the test, this may be resulted from the meshing and paring of mechanical components in the gearhead of the generator and caused some energy loss. Lastly yet importantly, although the sealing for the PTO worked well during the test, the environment inside the cylinder where the generator is located is very humid, this can also bring in some unexpected impact on the generator.

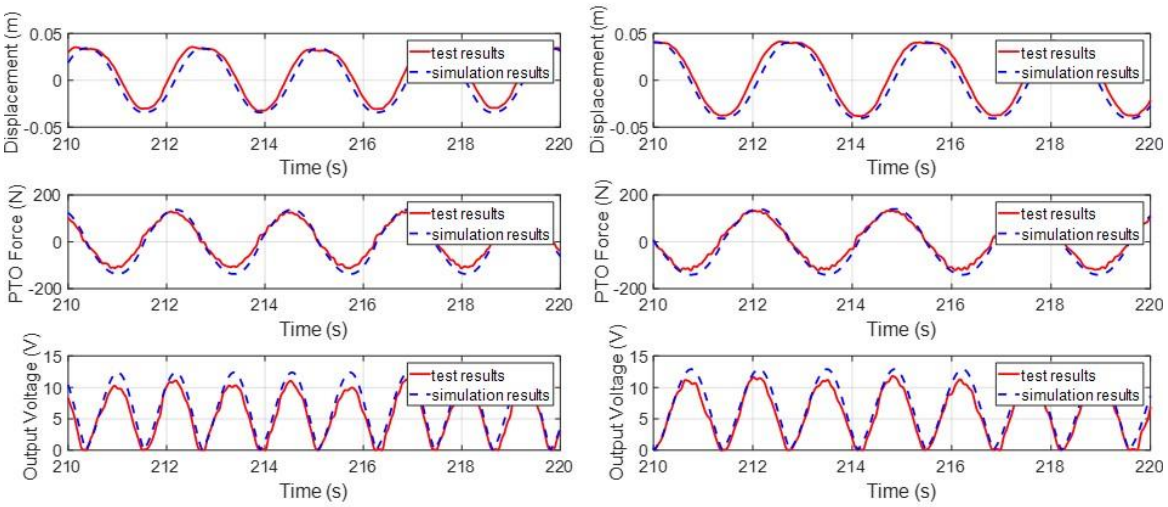

Figure 5-13 Left: Compare of simulation and test results for wave No.5; Right: Compare of simulation and test results for wave No.7

In Figure 5-13, the disengagement phenomenon of the MMR PTO observed during the water tank test is not obvious. This situation resulted from several reasons. Firstly, the excitation frequency at the wave tank test was low, and disengage ratio was small. Secondly, when the PTO is disengaged, the friction from the geared generator and the transmission gearbox will slow down the rotation speed of the generator quickly. Lastly, the rotatory inertia of the generator for the test is small and not able to store enough energy to continue power the generator during disengagement.

Table 6 Capture width ratio results for the 2DOF set-up in the wave tank test

Test	Full-Scale Energy Flux	2DOF Mechanical Power
2	36 kW/m	51.06
3	59 kW/m	58.69
4	91 kW/m	57.45
5	135 kW/m	51.87
6	196 kW/m	36.13
7	276 kW/m	21.01

Through the comparison between the 1DOF and 2DOF models, the 1:30 scale model WEC was used to compare a two-body WEC to a single-body WEC. Instead of varying the size of the submerged body during the experiment, the regular wave period was varied to find the optimal period for the submerged body. Experimental results show for regular waves the two-body WEC can produce twice the amount of power as a single-body WEC. Simulation shows that the power can be further increased by PTO design and power electronics optimization. The capture width ratios shown in Table 6 also met or exceeded similar two-body WEC designs. The two-body WEC also produced a quarter more power than a single-body WEC in irregular waves using the same optimal resistance value found for regular waves.

Besides the regular wave conditions, the test on irregular wave also proved the advantage of the 2DOF design. Figure? Shows the results of the power output from the two point absorbers in the same irregular wave condition listed in Table 5. The outer resistance chosen in the irregular wave test is the optimal outer resistance acquired during the previous test to guarantee the fairness of the compare. For the single body point absorber, the peak power achieved during the tests is 33.82W and the average power is 2.04W, whereas for the two body design the peak power is 44.98W and the average power is 2.61W, indicating that the two body design have extract more power in a more realistic wave condition.

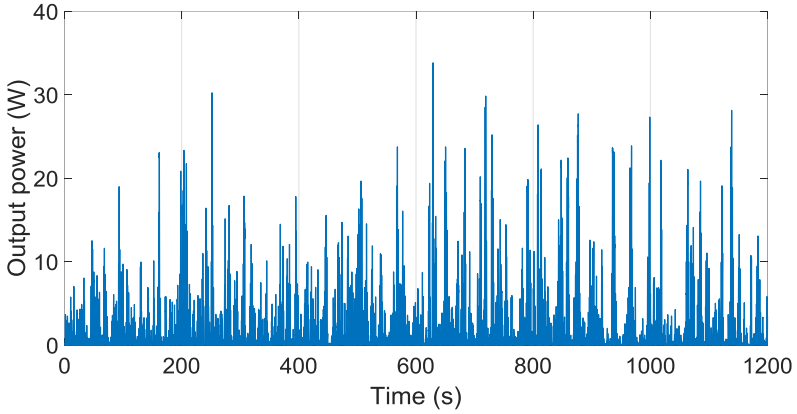

Figure 5-14 Power output of the single body point absorber in irregular wave test

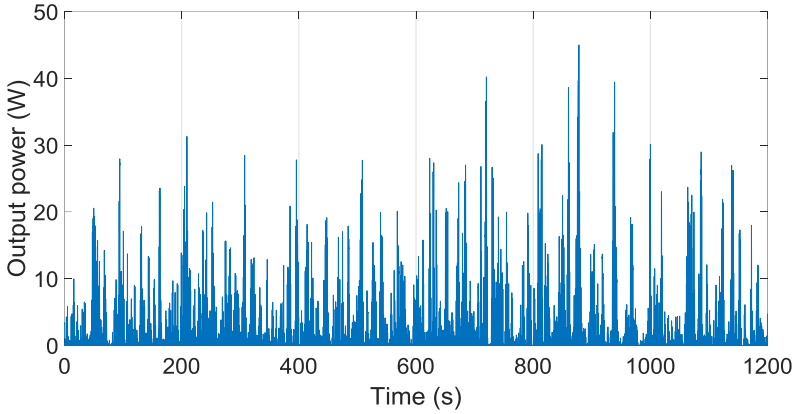

Figure 5-15 Power output of the two body self-reactive point absorber in irregular wave test

5.4 Compare Between the Fixed Two Body Point Absorber (2DOF) and the Moored Two Body Point Absorber (6DOF)

In addition to the comparison between the 1DOF and 2DOF, the comparison between the 2DOF set-up and 6DOF set-up is also conducted to evaluate how a two body WEC under more realistic installation with mooring. The detailed set-up is previously introduced in Figure 5-6.

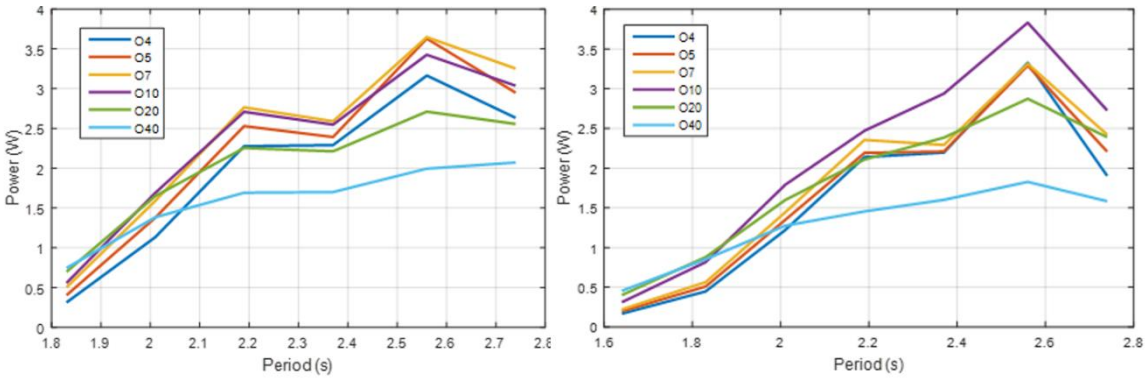

Figure 5-16 Left: Total electric power output of the 2DOF point absorber from the wave; Right: Total electric power output of the 6DOF point absorber from the wave

Figure 5-16 shows the compare of the total power output on the 2DOF and 6DOF set-up. It can be observed that under the mooring constrain, the self-reactive point absorber can still achieve the frequency matching effect and have the similar peak as the 2DOF set-up.

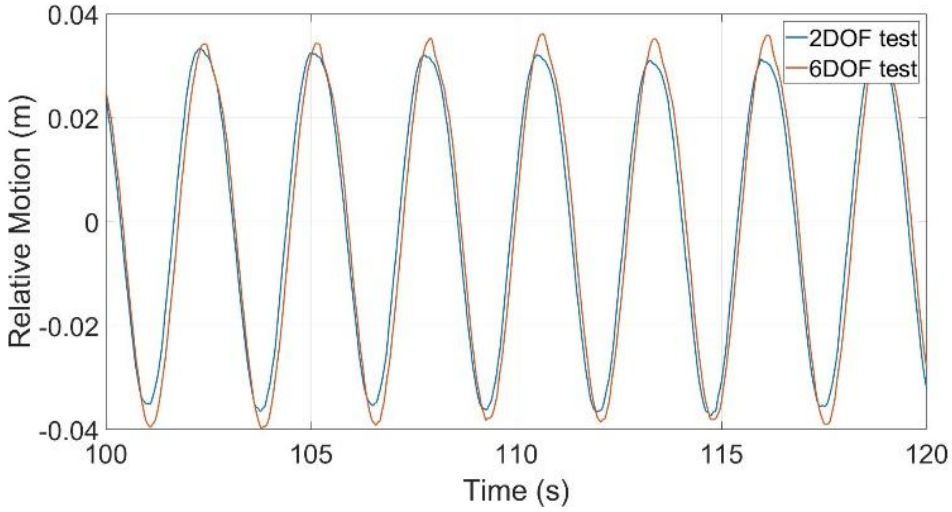

Figure 5-17 Compare of 2DOF and 6DOF in regular wave

Figure 5-17 shows the zoomed time domain test results comparison for the relative motion between the two bodies under the excitation of wave No.7 with 5Ω external resistance. It can be observed that due to the free motion in all degrees of freedom, the 6DOF has a larger relative motion between the floating buoy and the submerged body which leads to higher total input power. This is because the other motions of the WEC, for example, the pitch and sway, can contribute to a larger relative motion between the floating buoy and the submerged body. Therefore, the total energy absorption can be increased with the extra boost from the other motions.

Similar results can be observed in the irregular wave test, Figure 5-18 shows the zoomed time domain test results comparison between the two configurations in irregular waves. With same PTO damping coefficient applied, it is easy to observe that the 2DOF and 6DOF share similar dynamic response that follows the pattern of the irregular wave excitation. The 6DOF configuration has a larger displacement, indicating the same conclusion that it can benefit on energy absorption from the other motion.

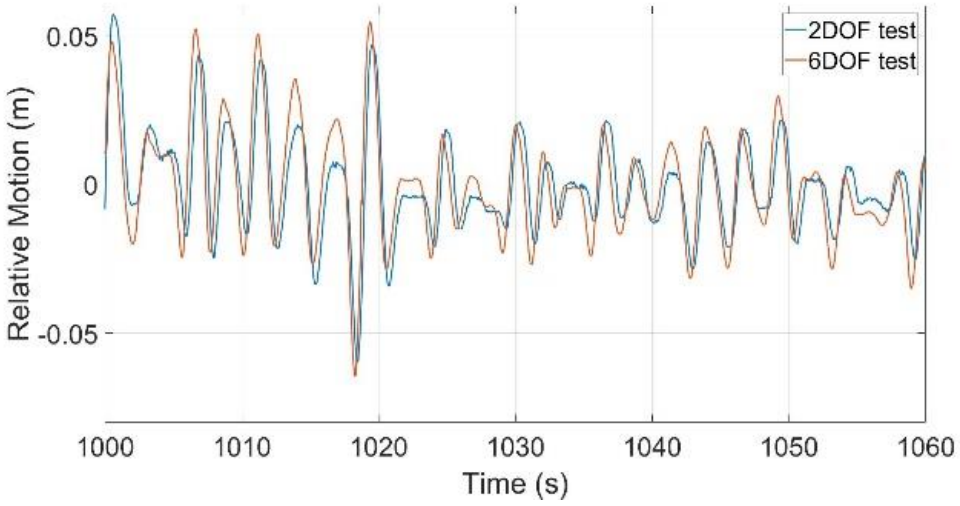

Figure 5-18 Compare of 2DOF and 6DOF in regular wave

5.5 Chapter Summary

In this Chapter, through the wave tank test, the WEC assembled with the MMR PTO is verified with its performance and several conclusions can be draw.

The effect and performance of the MMR PTO is satisfying and achieved as high as 58.69% of the CWR, which is superior to the other similar prototypes. Indicating the directly drive PTO with MMR can have a good advantage over other designs.

Compared with the single body design of the WEC, the two body WEC can successfully achieve the peak tuning on the natural frequency of the WEC. This helps the WEC to match with the frequency of the wave to achieve better energy absorption performance.

Using the 2DOF model to predict the power generation of the 6DOF WEC with mooring configuration is applicable. If the mooring is designed well, the other motion on the other degree of freedom can boost the relative motion of the bodies in heave, leading to a better performance on absorbing power.

6. Conclusion and Future Work

6.1 Conclusion

In this dissertation, a self-reactive point absorber with a mechanical Power Take-off (PTO) which adopts the mechanical motion rectifying (MMR) mechanism is introduced and investigated. Through the MMR mechanism, the bi-directional motion of the ocean wave excitation is rectified mechanically into unidirectional rotation of the generator, which can change the alternating stress on the components into normal stress, and improve the service life and reliability of the components. Moreover, during the rectifying motion, the energy stored in the inertia of the PTO can create a flywheel motion and decouple the PTO with excitation source to create a unique phenomenon of disengagement. During the disengagement, the generator can maintain certain speed by absorbing the stored kinematic energy and avoid the low efficiency zone and improve the total energy transfer efficiency.

The detailed design are introduced and multiple prototypes are developed in different scale including a 50W prototype, a 500W prototype and a 10kW prototype. These prototypes on PTO are tested under the in-lab environment, the test results show that the MMR PTO can achieve energy transfer efficiency as high as 81.2% and over 40% of improvement compared with the traditional non-MMR PTO. In addition, through a series of test, the weak components for the design are detected for further improvement.

The dynamic model on the MMR PTO are established with the piecewise nonlinear property of the engagement and disengagement considered. Through the data from the in-lab experiment on the MMR PTO, the unknown parameters on the model is characterized and the model is refined for better simulation accuracy. The refined model can predict the performance of the PTO well under different test conditions.

Moreover, the MMR PTO is assembled with a point absorber. A self-reactive two body structure is adopted for the point absorber with a reacting submerged body added. Through both theoretical analysis and experimental verification, by adjusting the second body shape and mass properly, the two body structure can successfully match the frequency of the ocean wave and hence significantly improve the total energy absorption. Three representative second body shape is chosen and the tank shape is chosen as it performed best in the simulation.

Three configurations including a single body point absorber in only heave motion (1DOF), a two body self-reactive point absorber in only heave motion (2DOF), and a two body self-reactive point absorber with mooring configuration (6DOF) are compared. The results show that the 2DOF configuration can almost double the power absorption compared with the 1DOF configuration near the resonant frequency, proving the advantage of the self-reactive structure once again. In addition, with the motion boost from other coupled motion, the 6DOF configuration can perform slightly better than the 2DOF under certain circumstance, indicating the importance of the mooring design. The two body point absorber developed in this dissertation achieved highest power Capture Width Ratio (CWR) of 58.69%, which can be considered impressive.

6.2 Future Work

6.2.1 Applying MMR PTO to other wave energy devices

The advantage of MMR PTO is on multiple aspects, in this dissertation, these advantages are introduced more on the point absorber type of Wave Energy Converter (WEC). However, the MMR PTO can be used for different types of WEC that are designed for various typical wave conditions to take the advantage of its high efficiency and reliability, especially for the oscillating wave energy devices.

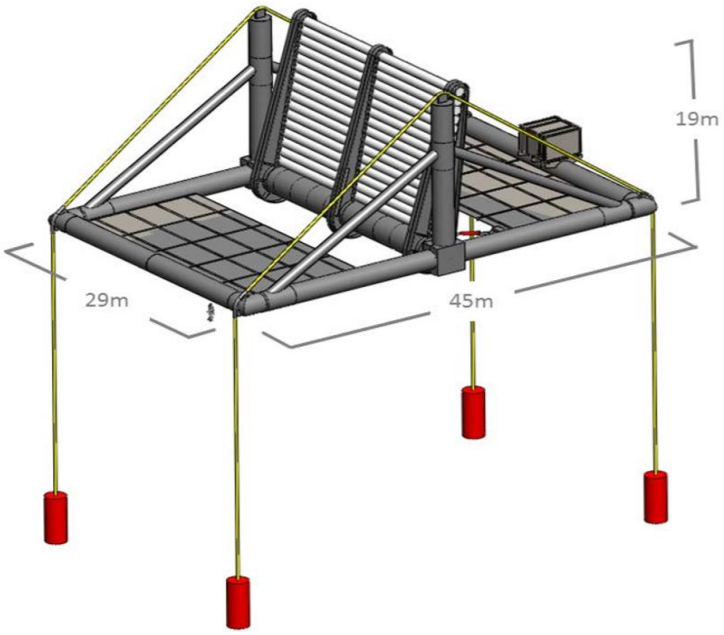

Figure 6-1 A typical wave surge device [82]

For example, unlike the point absorber that focuses more on using the heave motion of the ocean wave, the ocean wave surge device focus more on the absorbing the power in the surge motion of the wave. The motion of the surge device comes in as rotation and does not need to adopt ballscrew to transform the linear motion into rotation. However, the excitation speed of the wave surge device can be as low as 0.1rad/s and the excitation torque is large, which is not suitable for generating electricity if not speed up. As a result, a speed-up gearbox is desired in the design. Since it is already known that the increasing the inertia of the MMR PTO can contribute to a larger disengagement ratio and improve its performance, the speed-up gearbox can be taken advantage to increase the equivalent inertia of the PTO, indicating that the MMR PTO can have a board room for improving the performance of the wave surge device, and much research value can be applied on the optimization of design parameters.

Therefore, the design and analysis of the other types of WEC that are assembled with MMR PTO is worthy of further explore and will be the most important future work of this dissertation.

6.2.2 Mooring Configuration Design

From the wave tank test introduced previously, it can be concluded that the mooring configuration should be considered seriously during the design process, because the other motions besides the major working degree of freedom can also have influence on the power absorption. However, most of current research mainly work on the analysis of the WEC itself and lack of focus on the mooring configuration. Therefore, a comprehensive model that considers the WEC, PTO and mooring configuration together should be established for more accurate performance evaluation.

There are multiple choice for the mooring configuration of a WEC. For example, the catenary mooring adopts a free hanging anchor points which is horizontal to the seabed, and the mooring force mainly comes from the weight of the mooring lines, the taut mooring uses mooring line to directly connect the WEC with the anchor points on the seabed, and the fixed mooring uses a fixed structure on the seabed to constrain the motion of the WEC. The selection of the mooring type need to take both the dynamic of the WEC and the construction difficulty into consideration to improve the power absorption and decrease the cost.

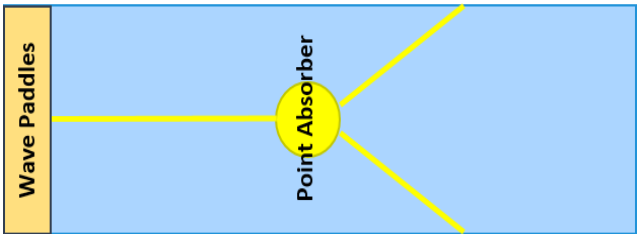

Figure 6-2 Mooring configuration of the tank test

Figure 6-2 shows the mooring configuration for the point absorber during the wave tank test, the three mooring lines are arranged in different angle and tied to the wall of the tank, and the mooring lines are in parallel to the floor of the tank. Using this configuration, the surge motion of the point absorber is constrained to guarantee that the point absorber remains on it desired location, yet the working degree of freedom, which is the heave motion, is not influenced. However, this mooring set-up is based on the wave tank test environment, and the real world application can be far less ideal and much more complicated. Therefore, the research on the mooring configuration can be a realistic problem and greatly improve the maturity of the technology if solved.

Reference

1. Blair, T. (2005). *Avoiding dangerous climate change*. UK Dept. for Environment, Food and Rural Affairs.
2. Renewable Capacity Statistics 2020. Accessible at: https://www.irena.org/publications/2020/Mar/Renewable-Capacity-Statistics-2020
3. S. H. Salter. (1974). Wave Power. *Nature* 249, no. 5459: 720-24.
4. Gunn, K., & Stock-Williams, C. (2012). Quantifying the global wave power resource. *Renewable Energy*, *44*, 296–304. https://doi.org/10.1016/j.renene.2012.01.101
5. Mo/rk Gunnar, Barstow, S., Kabuth, A., & Pontes, M. T. (2010). Assessing the Global Wave Energy Potential. *29th International Conference on Ocean, Offshore and Arctic Engineering: Volume 3*. https://doi.org/10.1115/omae2010-20473
6. EPRI (Electric Power Research Institute). 2011. Mapping and Assessment of the United States Ocean Wave Energy Resource. Palo Alto, CA. 1024637. Accessible at: https://www.energy.gov/sites/prod/files/2013/12/f5/mappingandassessment.pdf
7. Wave Energy Utilization in Europe: Current Status and Perspectives. (2018). *Renewable Energy*, 487–500. https://doi.org/10.4324/9781315793245-115
8. Ross, D. (1996). *Power from the waves*. Oxford University Press.
9. Falcão, A. F. D. O. (2010). Wave energy utilization: A review of the technologies. *Renewable and Sustainable Energy Reviews*, *14*(3), 899–918. https://doi.org/10.1016/j.rser.2009.11.003
10. Evans, D. V. (1978). The oscillating water column wave-energy device. *IMA Journal of Applied Mathematics*, *22*(4), 423-433.
11. Falcão, A. F., & Henriques, J. C. (2016). Oscillating-water-column wave energy converters and air turbines: A review. *Renewable Energy*, 85, 1391-1424. https://doi.org/10.1016/j.renene.2015.07.086
12. Weber, J., Mouwen, F., Parish, A., & Robertson, D. (2009). Wavebob—research & development network and tools in the context of systems engineering. In *Proc. Eighth European Wave and Tidal Energy Conference*, Uppsala, Sweden (pp. 416-420).

13. Whittaker, T., Collier, D., Folley, M., Osterried, M., Henry, A., & Crowley, M. (2007). The development of Oyster—a shallow water surging wave energy converter. In *Proceedings of the 7th European Wave and Tidal Energy Conference* (pp. 11-14).
14. Kofoed, J. P., Frigaard, P., Friis-Madsen, E., & Sørensen, H. C. (2006). Prototype testing of the wave energy converter wave dragon. *Renewable energy*, 31(2), 181-189. https://doi.org/10.1016/j.renene.2005.09.005
15. Budar, K., & Falnes, J. (1975). A resonant point absorber of ocean-wave power. *Nature*, *256*(5517), 478–479. https://doi.org/10.1038/256478a0
16. Evans, D. V. (1976). A theory for wave-power absorption by oscillating bodies. *Journal of Fluid Mechanics*, *77*(1), 1–25. https://doi.org/10.1017/s0022112076001109
17. C. Mei. (1976). Power extraction from water waves. *Journal of Ship Research,* 20: 63-66.
18. Budal, K., Falnes, J., Iversen, L. C., Lillebekken, P. M., Oltedal, G., Hals, T., ... & Høy, A. S. (1982). The Norwegian wave-power buoy project.
19. French, M. J., & Bracewell, R. (1986). Heaving point absorbers reacting against an internal mass. In *Hydrodynamics of Ocean Wave-Energy Utilization* (pp. 247-255). Springer, Berlin, Heidelberg.
20. Babarit, A., & Clément, A. (2006). Optimal latching control of a wave energy device in regular and irregular waves. *Applied Ocean Research*, *28*(2), 77–91. https://doi.org/10.1016/j.apor.2006.05.002
21. Babarit, A., Guglielmi, M., & Clément, A. H. (2009). Declutching control of a wave energy converter. *Ocean Engineering*, *36*(12-13), 1015–1024. https://doi.org/10.1016/j.oceaneng.2009.05.006
22. Falcão, A. F. D. O. (2008). Phase control through load control of oscillating-body wave energy converters with hydraulic PTO system. *Ocean Engineering*, *35*(3-4), 358–366. https://doi.org/10.1016/j.oceaneng.2007.10.005
23. Bjarte-Larsson, T., & Falnes, J. (2006). Laboratory experiment on heaving body with hydraulic power take-off and latching control. *Ocean Engineering*, *33*(7), 847–877. https://doi.org/10.1016/j.oceaneng.2005.07.007
24. Babarit Aurélien. (2017). *Ocean wave energy conversion: resource, technologies and performance*. ISTE Press Ltd.

25. Salter, S. H., & Lin, C. P. (1998). Wide tank efficiency measurements on a model of the sloped IPS buoy. In *Proceedings of 3rd European Wave Energy Conference* (pp. 200-6).
26. Hirohisa, T. (1982). Sea trial of a heaving buoy wave power absorber. In *Proceedings of 2nd international symposium on wave energy utilization, Trondheim, Norway* (pp. 403-17).
27. http://www.awsocean.com/archimedes-waveswing.html
28. Falnes, J. (1999). Wave-Energy Conversion Through Relative Motion Between Two Single-Mode Oscillating Bodies. *Journal of Offshore Mechanics and Arctic Engineering*, *121*(1), 32–38. https://doi.org/10.1115/1.2829552
29. Beatty, S. J., Buckham, B. J., & Wild, P. (2008). Frequency response tuning for a two-body heaving wave energy converter. In *The eighteenth international offshore and polar engineering conference*. International Society of Offshore and Polar Engineers.
30. Liang, C., & Zuo, L. (2017). On the dynamics and design of a two-body wave energy converter. *Renewable Energy*, *101*, 265–274. https://doi.org/10.1016/j.renene.2016.08.059
31. Korde, U. A. (2003). Systems of reactively loaded coupled oscillating bodies in wave energy conversion. *Applied Ocean Research*, *25*(2), 79–91. https://doi.org/10.1016/s0141-1187(03)00044-0
32. Babarit, A. (2010). Impact of long separating distances on the energy production of two interacting wave energy converters. *Ocean Engineering*, *37*(8-9), 718–729. https://doi.org/10.1016/j.oceaneng.2010.02.002
33. Cândido, J. J., & Justino, P. A. (2011). Modelling, control and Pontryagin Maximum Principle for a two-body wave energy device. *Renewable Energy*, *36*(5), 1545–1557. https://doi.org/10.1016/j.renene.2010.11.013
34. Yu, Y.-H., & Li, Y. (2013). Reynolds-Averaged Navier–Stokes simulation of the heave performance of a two-body floating-point absorber wave energy system. *Computers & Fluids*, *73*, 104–114. https://doi.org/10.1016/j.compfluid.2012.10.007
35. Shami, E. A., Wang, X., Zhang, R., & Zuo, L. (2019). A parameter study and optimization of two body wave energy converters. *Renewable Energy*, *131*, 1–13. https://doi.org/10.1016/j.renene.2018.06.117
36. Elwood, D., Yim, S. C., Prudell, J., Stillinger, C., Jouanne, A. V., Brekken, T., … Paasch, R. (2010). Design, construction, and ocean testing of a taut-moored dual-body wave energy

converter with a linear generator power take-off. *Renewable Energy*, *35*(2), 348–354. https://doi.org/10.1016/j.renene.2009.04.028

37. https://www.oceanpowertechnologies.com/powerbuoy
38. Têtu, A. (2017). Power take-off systems for WECs. In *Handbook of Ocean Wave Energy* (pp. 203-220). Springer, Cham.
39. Ruehl, K., & Bull, D. (2012). Wave Energy Development Roadmap: Design to commercialization. *2012 Oceans*, Hampton Roads, VA, pp. 1-10, doi: 10.1109/OCEANS.2012.6404795.
40. Henriques, J. C. C., Gomes, R. P. F., Gato, L. M. C., Falcão, A., Robles, E., & Ceballos, S. (2016). Testing and control of a power take-off system for an oscillating-water-column wave energy converter. *Renewable Energy*, *85*, 714-724. https://doi.org/10.1016/j.renene.2015.07.015
41. Lin, Y., Bao, J., Liu, H., Li, W., Tu, L., & Zhang, D. (2015). Review of hydraulic transmission technologies for wave power generation. *Renewable and Sustainable Energy Reviews*, *50*, 194–203. https://doi.org/10.1016/j.rser.2015.04.141
42. Henderson, R. (2006). Design, simulation, and testing of a novel hydraulic power take-off system for the Pelamis wave energy converter. *Renewable Energy*, *31*(2), 271–283. https://doi.org/10.1016/j.renene.2005.08.021
43. Mekhiche, M., Edwards, K., & Bretl, J. (2014). System-Level Approach to the Design, Development, Testing, and Validation of Wave Energy Converters at Ocean Power Technologies. *Volume 9B: Ocean Renewable Energy*. https://doi.org/10.1115/omae2014-24009
44. Falcão, A. F. D. O. (2008). Phase control through load control of oscillating-body wave energy converters with hydraulic PTO system. *Ocean Engineering*, 35.3-4: 358-366. https://doi.org/10.1016/j.oceaneng.2007.10.005
45. Bjarte-Larsson, T., & Falnes, J. (2006). Laboratory experiment on heaving body with hydraulic power take-off and latching control. *Ocean Engineering*, *33*(7), 847–877. https://doi.org/10.1016/j.oceaneng.2005.07.007
46. Gaspar, J. F., Calvário, M., Kamarlouei, M., & Soares, C. G. (2016). Power take-off concept for wave energy converters based on oil-hydraulic transformer units. *Renewable Energy*, *86*, 1232–1246. https://doi.org/10.1016/j.renene.2015.09.035

47. Elwood, D., Yim, S. C., Prudell, J., Stillinger, C., Jouanne, A. V., Brekken, T., … Paasch, R. (2010). Design, construction, and ocean testing of a taut-moored dual-body wave energy converter with a linear generator power take-off. *Renewable Energy*, *35*(2), 348–354. https://doi.org/10.1016/j.renene.2009.04.028
48. Lejerskog, E., Boström, C., Hai, L., Waters, R., & Leijon, M. (2015). Experimental results on power absorption from a wave energy converter at the Lysekil wave energy research site. *Renewable Energy*, *77*, 9–14. https://doi.org/10.1016/j.renene.2014.11.050
49. Mueller, M. (2002). Electrical generators for direct drive wave energy converters. *IEE Proceedings - Generation, Transmission and Distribution*, *149*(4), 446. https://doi.org/10.1049/ip-gtd:20020394
50. Vermaak, R., & Kamper, M. J. (2012). Design Aspects of a Novel Topology Air-Cored Permanent Magnet Linear Generator for Direct Drive Wave Energy Converters. *IEEE Transactions on Industrial Electronics*, *59*(5), 2104–2115. https://doi.org/10.1109/tie.2011.2162215
51. Eriksson, M. (2007). *Modelling and experimental verification of direct drive wave energy conversion: Buoy-generator dynamics* (Doctoral dissertation, Acta Universitatis Upsaliensis). Accessible at: https://www.diva-portal.org/smash/record.jsf?pid=diva2%3A169996&dswid=9785
52. Cruz, J. (2008). *Ocean wave energy: current status and future prespectives*. Springer.
53. Kececioglu, D. (1972). Reliability analysis of mechanical components and systems. *Nuclear Engineering and Design*, *19*(2), 259-290.
54. Shen, M. H. H. (1999). Reliability assessment of high cycle fatigue design of gas turbine blades using the probabilistic Goodman Diagram. *International journal of fatigue*, *21*(7), 699-708.
55. Nicholas, T., & Zuiker, J. R. (1996). On the use of the Goodman diagram for high cycle fatigue design. *International Journal of Fracture*, *80*(2-3), 219-235.
56. Falnes, J., & Kurniawan, A. (2020). *Ocean waves and oscillating systems: linear interactions including wave-energy extraction* (Vol. 8). Cambridge university press.
57. Falnes, J. (1980). Radiation impedance matrix and optimum power absorption for interacting oscillators in surface waves. *Applied Ocean Research*, *2*(2), 75–80. https://doi.org/10.1016/0141-1187(80)90032-2

58. Martin, D., Li, X., Chen, C.-A., Thiagarajan, K., Ngo, K., Parker, R., & Zuo, L. (2020). Numerical analysis and wave tank validation on the optimal design of a two-body wave energy converter. *Renewable Energy*, *145*, 632–641. https://doi.org/10.1016/j.renene.2019.05.109
59. Li, X., Liang, C., Chen, C.-A., Xiong, Q., Parker, R. G., & Zuo, L. (2020). Optimum power analysis of a self-reactive wave energy point absorber with mechanically-driven power take-offs. *Energy*, *195*, 116927. https://doi.org/10.1016/j.energy.2020.116927
60. Li, Z., Zuo, L., Kuang, J., & Luhrs, G. (2012). Energy-harvesting shock absorber with a mechanical motion rectifier. *Smart Materials and Structures*, *22*(2), 025008. https://doi.org/10.1088/0964-1726/22/2/025008
61. Liu, Y., Xu, L., & Zuo, L. (2017). Design, Modeling, Lab, and Field Tests of a Mechanical-Motion-Rectifier-Based Energy Harvester Using a Ball-Screw Mechanism. *IEEE/ASME Transactions on Mechatronics*, *22*(5), 1933–1943. https://doi.org/10.1109/tmech.2017.2700485
62. Beatty, S. J., Hall, M., Buckham, B. J., Wild, P., & Bocking, B. (2015). Experimental and numerical comparisons of self-reacting point absorber wave energy converters in regular waves. *Ocean Engineering*, *104*, 370–386. https://doi.org/10.1016/j.oceaneng.2015.05.027
63. Eriksson, M., Isberg, J., & Leijon, M. (2006). Theory and experiment on an elastically moored cylindrical buoy. *IEEE Journal of Oceanic Engineering*, *31*(4), 959-963.
64. W. E. Cummins. *The impulse response function and ship motions*. No. DTMB-1661. David Taylor Model Basin Washington DC, 1962.
65. WAMIT Manual, http://www.wamit.com, last access on March 2020.
66. Ruehl, K., Michelen, C., Kanner, S., Lawson, M., & Yu, Y. H. (2014, June). Preliminary verification and validation of WEC-Sim, an open-source wave energy converter design tool. In *International Conference on Offshore Mechanics and Arctic Engineering* (Vol. 45547, p. V09BT09A040). American Society of Mechanical Engineers.
67. Lawson, M., Yu, Y. H., Ruehl, K., & Michelen, C. (2014). Development and demonstration of the WEC-Sim wave energy converter simulation tool.
68. Zurkinden, A., Ferri, F., Beatty, S., Kofoed, J., & Kramer, M. (2014). Non-linear numerical modeling and experimental testing of a point absorber wave energy converter. *Ocean Engineering*, *78*, 11–21. https://doi.org/10.1016/j.oceaneng.2013.12.009

69. Engström, J., Kurupath, V., Isberg, J., & Leijon, M. (2011). A resonant two body system for a point absorbing wave energy converter with direct-driven linear generator. *Journal of Applied Physics*, *110*(12), 124904. https://doi.org/10.1063/1.3664855
70. Babarit, A., Hals, J., Muliawan, M., Kurniawan, A., Moan, T., & Krokstad, J. (2012). Numerical benchmarking study of a selection of wave energy converters. *Renewable Energy*, *41*, 44–63. https://doi.org/10.1016/j.renene.2011.10.002
71. Li, X., Chen, C. A., Xiong, Q., Parker, R., & Zuo, L. (2018, August). Design and simulation of a novel mechanical power take-off for a two-body wave energy point absorber. In *International Design Engineering Technical Conferences and Computers and Information in Engineering Conference* (Vol. 51852, p. V008T10A060). American Society of Mechanical Engineers.
72. Box, M. J. (1965). A new method of constrained optimization and a comparison with other methods. *The Computer Journal*, *8*(1), 42-52.
73. Andersson, J. (2001). *Multiobjective optimization in engineering design: applications to fluid power systems* (Doctoral dissertation, Linköpings universitet).
74. Goda, Y. (2010). *Random seas and design of maritime structures*. World scientific.
75. Chakrabarti, S. K. (1987). *Hydrodynamics of offshore structures*. WIT press.
76. Dallman, A. R., & Neary, V. S. (2014). *Characterization of US Wave Energy Converter (WEC) Test Sites: A Catalogue of Met-Ocean Data* (No. SAND2014-18206). Sandia National Lab.(SNL-NM), Albuquerque, NM (United States).
77. rmstrong, B. (1988). Friction: experimental determination, modeling and compensation. *Proceedings. 1988 IEEE International Conference on Robotics and Automation*. https://doi.org/10.1109/robot.1988.12266
78. Armstrong, B., Dupont, P., & Wit, C. C. D. (1994). A survey of models, analysis tools and compensation methods for the control of machines with friction. *Automatica*, *30*(7), 1083–1138. https://doi.org/10.1016/0005-1098(94)90209-7
79. Penalba, M., Davidson, J., Windt, C., & Ringwood, J. V. (2018). A high-fidelity wave-to-wire simulation platform for wave energy converters: Coupled numerical wave tank and power take-off models. *Applied Energy*, *226*, 655–669. https://doi.org/10.1016/j.apenergy.2018.06.008

80. Payne, G. (2008). Guidance for the experimental tank testing of wave energy converters. *SuperGen Marine, 254*.
81. Li, X., Martin, D., Liang, C., Chen, C., Parker, R. G., & Zuo, L. (2021). Characterization and verification of a two-body wave energy converter with a novel power take-off. *Renewable Energy*, *163*, 910–920. https://doi.org/10.1016/j.renene.2020.08.113
82. Yu, Y. H., Jenne, D. S., Thresher, R., Copping, A., Geerlofs, S., & Hanna, L. A. (2015). *Reference model 5 (rm5): Oscillating surge wave energy converter* (No. NREL/TP-5000-62861). National Renewable Energy Lab.(NREL), Golden, CO (United States).